

ACTA

UNIVERSITATIS OULUENSIS

Pekka Pirinen

EFFECTIVE CAPACITY
EVALUATION OF ADVANCED
WIDEBAND CDMA AND
UWB RADIO NETWORKS

FACULTY OF TECHNOLOGY,
DEPARTMENT OF ELECTRICAL AND INFORMATION ENGINEERING,
UNIVERSITY OF OULU

C
TECHNICA



ACTA UNIVERSITATIS OULUENSIS
C Technica 260

PEKKA PIRINEN

**EFFECTIVE CAPACITY EVALUATION
OF ADVANCED WIDEBAND CDMA
AND UWB RADIO NETWORKS**

Academic dissertation to be presented, with the assent of
the Faculty of Technology of the University of Oulu, for
public defence in Raahensali (Auditorium L10), Linnanmaa,
on December 4th, 2006, at 12 noon

OULUN YLIOPISTO, OULU 2006

Copyright © 2006
Acta Univ. Oul. C 260, 2006

Supervised by
Professor Savo Glisic

Reviewed by
Associate Professor Mohamed-Slim Alouini
Professor Abbas Jamalipour

ISBN 951-42-8269-8 (Paperback)
ISBN 951-42-8270-1 (PDF) <http://herkules.oulu.fi/isbn9514282701/>
ISSN 0355-3213 (Printed)
ISSN 1796-2226 (Online) <http://herkules.oulu.fi/issn03553213/>

Cover design
Raimo Ahonen

OULU UNIVERSITY PRESS
OULU 2006

Pirinen, Pekka, Effective capacity evaluation of advanced wideband CDMA and UWB radio networks

Faculty of Technology, University of Oulu, P.O.Box 4000, FI-90014 University of Oulu, Finland,
Department of Electrical and Information Engineering, University of Oulu, P.O.Box 4500, FI-90014 University of Oulu, Finland

Acta Univ. Oul. C 260, 2006

Oulu, Finland

Abstract

High radio capacity is one of the main targets in wireless network planning. The characteristics of the broadband radio channel pose serious challenges for achieving this goal. This thesis views the capacity problem from two frameworks. In the first, the effective user capacity in advanced direct sequence wideband code-division multiple-access (DS-SS) radio networks is evaluated. Sensitivity to various imperfections in key system parameters is studied. The analysis is based on a mathematical foundation that presents complex signal models and enables evaluation of the performance losses due to parameter estimation errors and multipath fading. The effective number of users supported in a cell is restricted by the multiple access interference (MAI) in the same cell (intracell interference) and overall background noise. The studied wideband CDMA receiver structures comprise conventional rake receivers with both the maximal ratio combining (MRC) and equal gain combining (EGC) schemes that can be supplemented with either linear decorrelating or nonlinear successive cancellation-based multiuser detectors and M -antenna spatial diversity.

The second framework focuses on direct sequence spread spectrum-based ultra wideband (UWB) indoor communications. Cochannel interference limited capacity is evaluated against the outage probability criterion in exponentially decaying lognormal multipath fading channels. Distance-dependence and spatial distribution of users is taken into account at different spatial cell configurations. Only moderate complexity partial rake receivers with noncoherent combining are employed. Total interference is composed of interpath, multipath, intracell, and intercell interference contributions. Lognormal sum approximations and simulations are used to evaluate distributions of the desired and interfering signals. The impact of the timing errors at the receiver monopulse correlation is studied.

The numerical results for the wideband CDMA framework show that effective user capacity and sensitivity depend critically on the joint impact of nonidealities in system parameters (e.g., channel profile, severity of fading, receiver algorithms). User capacities of the studied multiuser enhanced receivers were more prone to these impairments than those of the simpler single user receivers. The results should be used for network planning and optimization.

The numerical results of the UWB framework suggest that, even in the multipath rich channel, the optimal number of rake fingers can be less than half of the significant multipaths. Differences between circular, square, and hexagonal cell models proved to be minor with respect to link distance distributions. The derived link distance statistics are useful tools in the analytic piconet dimensioning and optimization.

Keywords: decorrelator, fading multipath channel, imperfections, interference cancellation, lognormal fading, outage probability, rake receiver

Preface

Research work related to this thesis was carried out at the Telecommunication Laboratory and the Centre for Wireless Communications (CWC), Department of Electrical and Information Engineering, University of Oulu, Oulu, Finland, during the years 1995–2006. The Telecommunication Laboratory and CWC have a long and successful record in studying spread spectrum techniques and their wireless applications. This work covers multiple access effective capacity studies of advanced wideband code division multiple access (CDMA) and direct sequence ultra wideband (UWB) networks.

The thesis work has been financially supported by the Infotech Oulu Graduate School during the period 1/1999–6/2001. Partial funding is due to various research projects in which I have had the pleasure of be involved over the last number of years. The Finnish Funding Agency for Technology and Innovation (Tekes), the Finnish Academy (through the CAFU project, project number 104783), the European Union (through the projects EU-ACTS-AC090 FRAMES, EU-IST-506897 PULSERS, and EU-IST-507325 NEWCOM), Elektrobit, Nokia, Finnish Defense Forces, Patria, Instrumentointi, WHealth, and ODL Health earn recognition for their support. In addition to the project funding, the following Finnish foundations have granted personal scholarships for doctoral studies: Tauno Tönnöngin säätiö, Jenny ja Antti Wihurin rahasto, Oulun yliopiston tukisäätiö, Tekniikan edistämissäätiö, HPY:n tutkimussäätiö, Seppo Säynjäläkankaan tiedesäätiö and Nokia Oyj:n säätiö. All these contributions are hereby gratefully acknowledged.

I am grateful to Professor Pentti Leppänen, Head of the Telecommunication Laboratory, for engaging me as a diploma thesis worker at the Telecommunication Laboratory in early 1994. His supervision of my Diploma and Licentiate works has been a valuable milestone in my research career.

I want to thank the pre-examiners of the thesis, Professor Abbas Jamalipour from the University of Sydney, Australia, and Associate Professor Mohamed-Slim Alouini from Texas A&M University at Qatar, Qatar, for their valuable work. My colleague Dr. Matti Hämäläinen deserves a special distinction for a profound review and constructive commenting of the manuscript. I would also like to thank Nicholas Longhurst for proofreading.

Professor Savo Glisic earns my deepest appreciation for supervising this doctoral dissertation work. He has persistently guided me through difficulties and helped me to stay on the course, when my own compass has bumbled around. I would also like to thank Professors Jari Iinatti, Markku Juntti, and Matti Latva-aho for research, academic, administrative, and other stimulating discussions. The former director of CWC, Dr. Ian Oppermann, deserves acknowledgment for pushing me forward in the (never-ending) postgraduate studies, and for offering challenging project opportunities.

Thanks are also due to the whole CWC and Telecommunication Laboratory staff equally for creating a comfortable working atmosphere and fair attitude among personnel while dealing with everyday duties. I am grateful to those colleagues who have voted me to be representative in the faculty and department level governing bodies. The years in these positions of trust improved my knowledge about the university decision-making and administration.

Finally, I am indebted to my parents Marjatta and Veikko for their love and support throughout my life. They have raised me to be down-to-earth and to appreciate hard work. Visits to childhood home during my studies have always been refreshing breaks for the mind in exchange for more physical countryside activities. My sisters Satu (and her family) and Anne have also brought joy to my life.

Oulu, November 8, 2006

Pekka Pirinen

Symbols and abbreviations

a	side of a square cell
A	generic amplitude scaling constant
\mathbf{A}	$(K \times K)$ -element diagonal matrix of transmitted amplitudes of all users at one symbol interval
\mathbf{A}	$(N_b K \times N_b K)$ -element diagonal matrix of transmitted complex amplitudes of all users over all symbol intervals
A_c	circular cell area
A_h	hexagonal cell area
A_k	transmitted signal amplitude of user k
\mathbf{A}_k	L_0 -element vector of imperfect rake combining coefficients of user k
a_{klm}	received complex signal amplitude of user k over the l th path and m th antenna
A_{klm}	received signal amplitude of user k over the l th path and m th antenna
A_{kr}	channel amplitude of user k at receiver branch r
A_s	square cell area
a_l	real-valued amplitude of the l th multipath
b	data bit
$b_{ik}^{(n)}$	in-phase channel data bit of user k over the n th symbol interval
$b_{qk}^{(n)}$	quadrature channel data bit of user k over the n th symbol interval
B_L	tracking loop bandwidth
\mathbf{c}	vector of interference cancellation coefficients
c_c	control channel spreading code
c_d	data channel spreading code
c_{ik}	in-phase part of the chip waveform of user k after chip pulse shaping
$c_{ikg}^{(n)}$	g th chip of spreading code of user k in in-phase channel over symbol interval n
C_{klm}	interference cancellation coefficient of user k at path l and antenna m
c_{qk}	quadrature part of the chip waveform of user k after chip pulse shaping
$c_{qkg}^{(n)}$	g th chip of spreading code of user k in quadrature channel over symbol interval n

c_s	scrambling code
c_{ls}	long scrambling code
c_0	propagation slope constant before the breakpoint
c_1	normalization constant to ensure continuity of the dual-slope model
c_2	propagation slope constant after the breakpoint
\mathbb{C}	set of complex numbers
d	link distance
\mathbf{d}	generic K -element vector of transmitted data symbols
\mathbf{d}	$N_b K$ -element vector of data symbols of all users over all symbol intervals
\mathbf{D}_{ab}	complex multiuser data vector with I- and Q-branch combinations $a \in [i, q]$ and $b \in [i, q]$
$\mathbf{d}^{(n)}$	K -element vector of transmitted data symbols at symbol interval n
d_{break}	breakpoint distance of the dual-slope path loss model
d_c	control channel information bit
d_d	data channel information bit
d_{des}^x	desired link distance with percentiles $x \in [10, 100]$
\mathbf{d}_i	I-branch $N_b K$ -element vector of data symbols of all users over all symbol intervals
d_{ik}	in-phase part of the bit waveform of user k after bit pulse shaping
d_{inter}^x	intercell link distance with percentiles $x \in [10, 100]$
d_{intra}^x	intracell link distance with percentiles $x \in [10, 100]$
$d_k^{(n)}$	transmitted data symbol of user k at symbol interval n
d_{max}	maximum link distance
d_{min}	minimum link distance
\mathbf{d}_q	Q-branch $N_b K$ -element vector of data symbols of all users over all symbol intervals
d_{qk}	quadrature part of the bit waveform of user k after bit pulse shaping
$d_{scen_0_j}^x$	scenario dependent link distance
E_b	bit energy
E_{bk}	received bit energy of user k
$f(\mathbf{a})$	intracell interference density
f_D	maximum Doppler shift
g	chip index
G	processing gain, number of chips per symbol
\mathbf{h}	$N_b K$ -element vector of data-amplitude products of all users over all symbol intervals
\mathbf{H}	generic $(KLM \times K)$ -element matrix of channel coefficient vectors
\mathbf{H}	$(N_b KLM \times N_b K)$ -element matrix of the channel coefficient vectors of all users over all symbol intervals
$h(t)$	channel impulse response
$\mathbf{H}^{(n)}$	$(KLM \times K)$ -element matrix of channel coefficient vectors of all users at symbol interval n

$\mathbf{H}_k^{(n)}$	LM -element vector of channel coefficients of user k at symbol interval n
$\mathbf{h}_k^{(n)}(t)$	vector channel impulse response of user k over symbol interval n
$\mathbf{h}_{kl}^{(n)}$	vector of complex channel gains of user k over the l th path at symbol interval n
$h_{klm}^{(n)}$	complex channel gain of user k over the l th path and m th receive antenna at symbol interval n
$H_{k,lm}^{(n)}$	user k l th path and m th antenna element of $\mathbf{H}_k^{(n)}$ at symbol interval n
$h_{km}^{(n)}(t)$	the m th row of $\mathbf{h}_k^{(n)}(t)$
$\mathbf{H}_{kl}^{(n)}$	magnitude of the complex vector channel gain of user k over the l th path at symbol interval n
$H_{klm}^{(n)}$	magnitude of the complex channel gain of user k over the l th path and m th receive antenna at symbol interval n
i	index
I	cochannel interference power
I_e	interference element in ΔR
I_{INTER}	intercell interference power
I_{INTRA}	intracell interference power
I_{IPI}	interpath interference power
I_{MPI}	multipath interference power
I_{oc}	power density of intracell interference
I_{oic}	power density of intercell interference
I_{oin}	power density of overlay type of internetwork interference
I_0	interference power density
$I_0(\cdot)$	zeroth order Bessel function of the first kind
$I_1(\cdot)$	first order Bessel function of the first kind
j	imaginary unit, index
k	user index
K	number of active users
k'	user index
K_{DEC}	effective user capacity with imperfect decorrelator
K_{DEC}^{\max}	maximum user capacity with decorrelator
K_{NL}	effective user capacity with imperfect nonlinear multiuser detector
K_{NL}^{\max}	maximum user capacity with nonlinear multiuser detector
K_{MF}	effective user capacity with imperfect rake receiver
K_{MF}^{\max}	maximum user capacity with rake receiver
l	multipath index
L	number of multipaths
l'	multipath index
L_w	wall loss in dB scale
L_0	number of rake fingers
m	Nakagami fading parameter

m	antenna index
M	modulation alphabet size
M	number of receive antennas, modulation alphabet size
m'	antenna index
m_d	area mean desired signal power
m_g	mean of the Gaussian interference distribution
m_{IP1}	mean value of the interpath interference components
m_{IPM}	mean value of the inverted multipath profile components
m_{MPI}	mean value of the multipath profile components
m_{PL}	signal mean value in dB scaled by the path loss
m_z	area mean total cochannel interference power
m_0	signal mean value in dB without path loss
\mathbf{n}	$N_b KLM$ -element Gaussian output noise vector
$\mathbf{n}^{(n)}$	KLM -element Gaussian output noise vector at symbol interval n
n	discrete symbol interval index, index
N	maximum number of intracell interferers
N_b	number of symbols in the data packet
\mathbf{n}_i	$N_b KLM$ -element Gaussian output noise vector in the I-branch
\mathbf{n}_q	$N_b KLM$ -element Gaussian output noise vector in the Q-branch
\mathbf{n}_r	Gaussian approximated residual noise vector
N_0	overall noise density
P_{act}	interference source activity factor
$p_c^c(d)$	link distance probability density function in a single circular cell with centralized topology
$p_c^d(d)$	link distance probability density function in a single circular cell with distributed topology
$p_{cc}^c(d)$	intercell link distance probability density function in a centralized circular multiple cells scenario
$P_{CDF}(\cdot)$	cumulative distribution function of link distance
P_e	bit error probability
$p_h^c(d)$	link distance probability density function within a single hexagonal cell
$p_{hh}^c(d)$	link distance probability density function in a centralized hexagonal multiple cells scenario
$P_n(n)$	cochannel interference probability density function of n active interferers
$P_{out}(\cdot)$	outage probability
$P_{out}(I n)$	conditional outage probability on n active cochannel interferers
$p_{PDF}(\cdot)$	probability density function of link distance
$p_{s_a}^c(d)$	link distance probability density function in a centralized single square cell <i>Scenario a</i>
$p_{s_b}^c(d)$	link distance probability density function in a centralized single square cell <i>Scenario b</i>

$p_{s_c}^c(d)$	link distance probability density function in a centralized single square cell <i>Scenario c</i>
$p_{s_d}^d(d)$	link distance probability density function in a distributed single square cell <i>Scenario d</i>
$p_{s_{01}}^c(d)$	intercell link distance probability density function between cells #0 and #1 in a centralized multiple square cell scenario
$p_{s_{02}}^c(d)$	intercell link distance probability density function between cells #0 and #2 in a centralized multiple square cell scenario
$p_{s_{0(1&2)}}^c(d)$	intercell link distance probability density function between cell #0 and union of cells #1 and #2 in a centralized multiple square cell scenario
$PL(d)$	path loss as a function of link distance d
r	diversity order index
R	simplified expression of crosscorrelation function
\mathbf{r}	diversity order vector
\mathbf{R}	generic $(KLM \times KLM)$ -element crosscorrelation matrix of signature waveforms
\mathbf{R}	$(N_b KLM \times N_b KLM)$ -element matrix of crosscorrelations of signature waveforms for all multipath components of all users over all symbol intervals
\mathbb{R}	set of real numbers
$\mathbf{R}^{ab(n)}(i)$	extension of $\mathbf{R}^{(n)}(i)$ to in-phase and quadrature branch elements
\mathbf{R}^{ab}	I- and Q-branch mixes of $(N_b KLM \times N_b KLM)$ -element matrix of crosscorrelations of signature waveforms for all multipath components of all users over all symbol intervals
\mathfrak{R}^{ab}	extension of matrix product \mathbf{RHA} to in-phase and quadrature branch elements
$\mathbf{R}^{(n)}(i)$	$(KLM \times KLM)$ -element crosscorrelation matrix of signature waveforms with delay i at symbol interval n
$R^2(\cdot)$	squared autocorrelation function of the Gaussian pulse waveform
R_b	bit rate
R_c	chip rate
\mathfrak{R}_{DEC}	sensitivity function of the decorrelator
r_{dz}	correlation between desired signal and total interference
R_h	hexagonal cell radius
$r_k^{(L_0)}$	rake receiver efficiency of user k with L_0 diversity branches
R_{kk}^+	kk th element of inversed correlation matrix $\hat{\mathbf{R}}^{-1}$
$\mathbf{R}_{k,k'}^{ab(n)}(i)$	$(LM \times LM)$ -element in-phase and quadrature terms crosscorrelation matrix of signature waveforms of users k and k' with delay i at symbol interval n
$\left(\mathbf{R}_{k,k'}^{ab(n)}(i)\right)_{lm,l'm'}$	element of matrix $\mathbf{R}_{k,k'}^{ab(n)}(i)$

$\mathbf{R}_{k,k'}^{(n)}(i)$	$(LM \times LM)$ -element crosscorrelation matrix of signature waveforms of users k and k' with delay i at symbol interval n
$r_m(t)$	complex envelope of the received continuous-time signal at the m th receive antenna
\mathfrak{R}_{MF}	sensitivity function of the rake receiver
r_{mpi}	multipath correlation
\mathfrak{R}_{NL}	sensitivity function of the nonlinear interference cancellation
R_1	circular single cell radius
R_2	radius of a circular cell whose area covers nine single cells
S	received power of the useful signal
$S(L_0)$	desired signal power combined by L_0 rake fingers
S_{ik}	in-phase component of the spread data waveform of user k
s_k	complex envelope of the signal transmitted by user k
S_k	complex spread data bit of user k
$s_k^{(n)}(t)$	continuous-time complex envelope of the signal transmitted by user k at symbol interval n
S_{qk}	quadrature component of the spread data waveform of user k
$S_k^{(n)}(t)$	combined data and signature waveform of user k at symbol interval n
s_ε	carrier phase estimation error
s_ρ	code phase estimation error
SNR_L	tracking loop signal-to-noise ratio
S/I	signal-to-interference power ratio
$(S/I)_{tar}$	signal-to-interference power ratio target
t	continuous-time index
T	symbol duration
T_b	bit duration
T_c	chip duration
T_m	maximum delay of the channel
T_p	Gaussian pulse duration
u	index
U	number of active intercell interference sources
v	integration variable
$w_{G_n}(t)$	n th derivate Gaussian pulse waveform
\mathbf{w}_k	L_0 -element vector of rake combining coefficients
w_{kr}	k th user r th diversity branch rake combining coefficient
x	index, integration variable
y	index, signal-to-noise ratio
\mathbf{y}	$N_b KLM$ -element complex matched filter output sample vector
$\mathbf{y}^{(n)}$	KLM -element complex matched filter output sample vector at symbol interval n
\mathbf{y}_{ab}	I- and Q-branch mixes of $N_b KLM$ -element complex matched filter output sample vectors
Y_{bk}	received bit signal-to-noise ratio of user k

$\bar{\mathbf{y}}_i$	I-branch output sample vector of $N_b KLM$ -element complex matched filter
$\mathbf{y}_{ik}^{(n)}$	LM -element vector of I-branch matched filter output of user k at symbol interval n
$y_{iklm}^{(n)}$	I-branch matched filter output of user k over the l th path and m th receive antenna at symbol interval n
$\mathbf{y}_k^{(n)}$	LM -element complex sum vector of I- and Q-branch matched filter outputs of user k at symbol interval n
γ_k	signal-to-noise ratio of user k
\mathbf{y}_q	Q-branch output sample vector of $N_b KLM$ -element complex matched filter
$\mathbf{y}_{qk}^{(n)}$	LM -element vector of Q-branch matched filter output of user k at symbol interval n
$y_{qklm}^{(n)}$	Q-branch matched filter output of user k over the l th path and m th receive antenna at symbol interval n
Y_0	signal-to-noise ratio target
z	index
$z_m(t)$	complex continuous-time zero-mean additive white Gaussian noise at the m th receive antenna
$\mathbf{0}_{KLM}$	all-zero matrix of size $KLM \times KLM$
$\mathbf{1}$	vector of all ones
α	average power of the multipath components
$\bar{\mathbf{a}}$	vector of exponential multipath profile path gains
$\bar{\mathbf{a}}$	reversed vector of exponential multipath profile path gains
\mathbf{a}_k	vector of channel power coefficients of user k
\mathbf{a}_{klm}	$(K \times LM)$ -element vector of channel power coefficients of user k over paths l and antennas m
α_{klm}	channel power coefficient of user k at path l and antenna m
α_{kr}	channel power coefficient of user k at the r th receiver branch
α_l	mean channel power coefficient of the l th multipath
$\bar{\alpha}_l(\varepsilon_l)$	mean channel power coefficient of the l th multipath as a function of the normalized timing offset ε_l
α_{lm}	mean channel power coefficient of the l th multipath and m th antenna
$\delta(t)$	Dirac's delta function
ΔA_{kr}	difference of user k amplitude and its estimate at receiver branch r
ΔR	additional Gaussian noise component in correlation matrix
$\Delta \mathbf{R}$	difference of the actual and estimated crosscorrelation matrix
$\Delta \varepsilon$	phase estimation error term
$\Delta \phi$	phase estimation error
$\Delta \phi_1$	user 1 phase estimation error
$\Delta \phi_2$	user 2 phase estimation error

$\Delta\rho$	correlation function error
$\Delta\tau_1$	user 1 delay estimation error
$\Delta\tau_2$	user 2 delay estimation error
ε	phase difference, estimation error
ε_a	relative amplitude estimation error
ε_b	bit offset
ε_c	chip offset
ε_t	normalized timing error
$\varepsilon_{k'l'm',klm}$	phase difference
$\varepsilon_{\theta kr}$	carrier phase synchronization error of user k at receiver branch r
ε_τ	difference of two delay estimation errors
ϕ_0	frequency downconversion phase error
ϕ_1	user 1 phase
ϕ_2	user 2 phase
ϕ_{kl}	channel phase of user k over path l
ϕ_{k0}	transmitted signal carrier phase
ϕ_{klm}	phase of the complex channel coefficient of user k at path l and antenna m
Φ_{klm}	phase of the received signal of user k at path l and antenna m
$\tilde{\Phi}_{klm}$	estimated phase of the received signal of user k at path l and antenna m
η	thermal noise power density after decorrelation
η_{th}	thermal noise power density
η_0	overall Gaussian noise power density including thermal noise, intercell and internetwork interference
$\varphi(t)$	bit waveform
λ_l	temporal (delay) decay parameter
λ_m	spatial decay parameter
θ_{kr}	carrier phase of user k at receiver branch r
ρ	crosscorrelation function
ρ'	correlation function slope at the zero delay estimation error
$\rho_{x,y}$	crosscorrelation of x and y
σ	standard deviation of the complex zero-mean additive white Gaussian noise process
σ_d	desired signal standard deviation
σ_g	standard deviation of the Gaussian interference distribution
σ_{IPI}	standard deviation of the interpath interference components
σ_{IPM}	standard deviation of the inverted multipath profile components
$\sigma_l^2(\varepsilon_t)$	variance of the path l received signal as a function of normalized timing offset ε_t
σ_{MPI}	standard deviation of the multipath profile components
σ_n^2	Gaussian noise variance
Σ_n^2	Gaussian noise variance after decorrelation
σ_r^2	Gaussian approximated residual noise variance

Σ_r^2	variance contribution due to system imperfections after decorrelation
σ_z	standard deviation of the total cochannel interference
$\sigma_{\Delta R}^2$	variance of the additional Gaussian noise component in correlation matrix due to estimation imperfections
σ_ϕ^2	Gaussian phase estimation error variance
σ_ρ^2	squared magnitude of the correlation function slope at the point of zero-delay error
σ_τ^2	Gaussian delay estimation error variance
τ_k	delay of the k th user's signal
τ_l	delay of the l th multipath
τ_{klm}	delay of user k at path l and antenna m
$\tau_{kl}^{(n)}$	delay of user k at path l over symbol period n
ζ_0	squared sum of rake combining coefficients over L_0 diversity branches
ω_0	angular carrier frequency
ξ	index
Ξ	modulation symbol alphabet
$\psi(t)$	chip waveform
$\mathfrak{F}^x(\cdot)$	x -element vector

AWGN	additive white Gaussian noise
BEP	bit error probability
BER	bit error rate
BPSK	binary phase shift keying
CDF	cumulative distribution function
CDMA	code division multiple access
CM	channel model
CWC	Centre for Wireless Communications
DPSK	differentially coherent phase shift keying
DS	direct sequence
EGC	equal gain combiner/combining
EKF	extended Kalman filter
FCC	the Federal Communications Commission
FDD	frequency-division duplex
FDMA	frequency division multiple access
fpc	full power control
FW	Fenton–Wilkinson
GPS	global positioning system
GSM	global system for mobile communications
I	in-phase
IC	interference cancellation
IEEE	the Institute of Electrical and Electronics Engineers, Inc.
IR	impulse radio
ISI	intersymbol interference
LMMSE	linear minimum mean squared error

LOS	line-of-sight
LSG	log shifted gamma
MAI	multiple access interference
MBO	multiband OFDM
MGF	moment generating function
MIMO	multiple-input multiple-output
MIP	multipath intensity profile
ML	maximum-likelihood
MMSE	minimum mean squared error
M-PPM	M -ary pulse position modulation
MPSK	M -ary phase shift keying
MRC	maximal ratio combiner/combining
MSIC	multistage successive interference cancellation
MUD	multiuser detection
MUI	multiple user interference
NLOS	non-line-of-sight
npc	no power control
OFDM	orthogonal frequency division multiplexing
OOK	on-off keying
PC	power control
PDF	probability density function
PDP	power delay profile
PIC	parallel interference cancellation
ppc	partial power control
PPM	pulse position modulation
PSK	phase shift keying
Q	quadrature
QoS	quality-of-service
RLS	recursive least squares
rpc	rake power control
SC	selection combiner/combining
SIC	successive interference cancellation
SNR	signal-to-noise ratio
SS	spread spectrum
ST	space-time
STDL	stochastic tapped delay line
SY	Schwartz–Yeh
TDMA	time division multiple access
TH	time hopping
UMTS	universal mobile telecommunications system
UWB	ultra wideband
WCDMA	wideband code division multiple access
WILHO	wireless technology in hospital operation management
ZF	zero-forcing
*	convolution
$(\cdot)^{(n)}$	value at the n th symbol interval

\mathbf{A}^{-1}	inverse of \mathbf{A}
\mathbf{A}^T	transpose of \mathbf{A}
$\hat{\mathbf{A}}$	estimate of \mathbf{A}
$\overline{\mathbf{A}}$	average of \mathbf{A}
$(\mathbf{A})_{i,j}$	i th row and j th column element of matrix \mathbf{A}
$\text{diag}(\dots)$	diagonal matrix with elements \dots on the main diagonal
$E(\cdot)$	expectation
$\text{erfc}(\cdot)$	complementary error function
$\ln(\cdot)$	natural logarithm
$Q(\cdot)$	zero-mean, unit-variance Gaussian complementary distribution function
$\text{Re}(\cdot)$	real part
$\text{sgn}(\cdot)$	signum function
$\text{var}(\cdot)$	variance
$\text{vec}(\cdot)$	vector
$ \cdot $	magnitude, absolute value
$\ \cdot\ $	Euclidean norm
$\lfloor x \rfloor$	largest integer less than or equal to x

Contents

Abstract	
Preface	
Symbols and abbreviations	
Contents	
1 Introduction	21
1.1 Motivation	21
1.2 Author's contributions	22
1.3 Thesis outline	22
2 Literature review	24
2.1 CDMA capacity	24
2.2 Multiuser detection	26
2.3 Diversity methods	29
2.4 UWB systems	31
2.5 Lognormal sum approximations	36
3 Signal and channel models for the wideband CDMA framework	39
3.1 Transmitted and received waveforms	39
3.2 Space-time multipath intensity profile	46
4 Wideband CDMA performance analysis	48
4.1 CDMA system capacity	48
4.2 Space-time rake combining in the multipath channel	51
4.2.1 Equal gain combining	51
4.2.2 Maximal ratio combining	52
4.2.3 Channel parameter estimation errors	53
4.3 Imperfect rake receiver	54
4.3.1 User capacity and sensitivity	54
4.3.2 Numerical examples	55
4.4 Imperfect linear multiuser detector (decorrelator)	61
4.4.1 User capacity and sensitivity	62
4.4.2 Numerical examples	62
4.5 Imperfect nonlinear multiuser detector	70
4.5.1 Approximations	72

4.5.2	Outage probability	74
4.5.3	User capacity and sensitivity	75
4.5.4	Numerical examples	76
4.6	Performance comparison	84
4.7	Chapter summary	89
5	Ultra wideband spread spectrum framework	90
5.1	Introduction	90
5.2	System Description	91
5.2.1	Multipath channel model	91
5.2.2	Path loss model	92
5.2.3	Square cell network topologies and link distance distributions	93
5.2.3.1	Single cell scenarios	93
5.2.3.2	Multiple cell scenarios	97
5.2.4	Comparison of link distance statistics in different cellular models	101
5.2.4.1	Single cell comparisons	102
5.2.4.2	Multiple cell comparisons	104
5.2.5	UWB pulse waveforms and impact of timing errors	106
5.3	Outage probability analysis	108
5.4	Numerical examples	111
5.5	Chapter summary	124
6	Conclusions and future work	125
6.1	Summary and conclusions	125
6.2	Future research directions	126
	References	
	Appendix	

1 Introduction

1.1 Motivation

The capacity of cellular systems is of paramount importance to mobile operators, vendors, and system providers. Therefore, it is important to develop analytical tools to assess the capacity of wireless networks. There are practical, well-established, and generally accepted models and techniques available for the first and second generation wireless mobile networks. This has been possible because these systems are targeted for low data rate speech services keeping them relatively simple. Third generation wideband CDMA (code division multiple access) networks need to support variable rate services with different quality of service requirements. This means that they have become rather complex, heterogeneous, and difficult to analyze. Narrowband CDMA has been thoroughly studied during the last few decades. However, when the bandwidth is increased and state-of-the-art signal processing techniques are used, the former analysis and simulation methods become inadequate.

This study proposes new models for capacity analysis, taking into account imperfections in multiuser detection, multipath combining, and parameter estimation. These models quantify implementation losses in the system. The system model is based on the conventional multipath rake combiner that is enhanced with multiuser detection techniques and spatial diversity.

Ultra wideband (UWB) technology is emerging radio technology for short-range wireless communications (mainly indoors). Conceptually, UWB technology is not so much different from wideband CDMA technology. The second part of the thesis is devoted to the capacity studies in direct sequence ultra wideband (DS-UWB) single and multiple cell configurations. Similarities to the first framework are mainly in the adoption of exponential multipath channel profiles and rake reception. Simple or moderate complexity UWB devices (e.g., sensors) are assumed, which may lead to high appliance densities in small coverage areas.

1.2 Author's contributions

For the sake of clarity this thesis is written as a monograph. However, the main body of the manuscript is based on three original journal publications [1–3] and five conference papers [4–8]. Effective capacity evaluation in the thesis can be divided into two main analytical frameworks. The first research theme is based on the advanced broadband cellular CDMA systems. Contributions [1] and [2] set up the framework for effective capacity and sensitivity analysis of wideband CDMA networks. In [1], it is assumed that a nonlinear interference canceler is utilized at the receiver along with the rake receiver. Imperfections in equal gain and maximal ratio combining and interference cancellation, and fading in exponentially decaying multipath channel profiles are incorporated. Publication [2] extends the framework to cover a linear decorrelating detector and exploitation of spatial (antenna) diversity at the receiver. Conference papers [4] and [5] complement and summarize these studies by comparative performance analyses. Chapters 3 and 4 rely to large extent on these publications. However, numerical examples especially have been revised and the manner of representation has been unified according to the common assumptions and parameters over the framework.

The other main research theme and framework is built upon cochannel interference limited ultra-wideband communications, lognormal multipath fading and outage probability evaluation. References [3, 6–8] include results on this particular research topic. Paper [6] applies the conditional outage probability criterion to UWB communication system and studies the sensitivity to parameter variations. The framework is further modified to include square-shaped spatial topologies and relative path losses according to the cell geometry in [7]. Detailed link distance probability distribution derivations and descriptions of the interference aggregation from multiple sources are given in [3]. The latest contribution [8] compares different cell models and lognormal sum approximations in correlated multipath channels. Chapter 5 of the thesis is firmly based on the work conceived in the aforementioned publications.

The author of this thesis is the main author in all contributions but [1], where the first author, professor Savo Glisic provided the ideas and the scope for the article. The co-author complemented and further developed the ideas and created the numerical results. Most of the content for [2] was generated by the present author. The co-author, professor Savo Glisic, provided ideas, gave comments and supervised the writing process of the manuscript. Reference [3] was solely conceived by the author. Professor Jari Iinatti provided valuable comments to the manuscript.

1.3 Thesis outline

The rest of the thesis follows the organization given below. Chapter 2 provides an overview of the relevant literature in the research fields dealt with in the thesis. The main topics in the literature review are: CDMA capacity evaluation with single and multiuser detection techniques, multipath and spatial combining diversity techniques, ultra wideband communications, and lognormal sum approximations. Chapter 3 defines mathematical models for complex wideband CDMA signal and channel waveforms

including various imperfections. Chapter 4 provides effective user capacity analysis and numerical results for three receiver structures: imperfect space-time rake receiver, imperfect space-time rake receiver enhanced with linear decorrelator, and imperfect space-time rake receiver enhanced with nonlinear interference canceller. Chapter 5 includes the framework and numerical user capacity evaluations for UWB spread spectrum networks in lognormal multipath fading. Finally, some concluding remarks are given in Chapter 6, after which the references are listed.

2 Literature review

This chapter provides relevant background information or parallel work within the scope of the thesis. Section 2.1 reviews capacity evaluations of the second and the third generation CDMA systems. Section 2.2 summarizes multiuser detection related milestones with the special emphasis in user capacity. Section 2.3 is devoted to various diversity reception and multipath combining techniques. Section 2.4 presents some important steps in the ultra wideband research. Finally, a review of the methods of solving lognormal power sums is given in Section 2.5.

2.1 CDMA capacity

Prominent overviews of wireless spread spectrum and code division multiple access (CDMA) systems can be found in [9–11]. During the development of second generation cellular networks many narrowband CDMA research publications were issued. CDMA capacity analysis is covered in a number of papers, e.g., [12–36]. One of the landmark papers in this field is the work of Gilhousen *et al.* [12] that inspired and prompted many other researchers to simulate capacity of CDMA systems. Their analysis uses outage criterion, and includes voice activity monitoring, sectorization (3 sectors), perfect uplink power control and assumes a Gaussian approximation for multiple access interference (MAI) statistics. Paper [33] discusses analytically frequency reuse efficiency issues for CDMA and comes to the conclusion that a fully loaded multiple cell capacity is about $\frac{3}{4}$ of the single cell capacity. Cellular CDMA radio capacity framework of [11] is in part corrected and enhanced in [35].

The effect of imperfect power control (PC) on CDMA capacity has also been studied actively in the literature, e.g., [37–52]. The main conclusion that can be drawn from those references is that CDMA network capacity is very sensitive to closed loop PC errors, i.e., the capacity decreases rapidly as a function of power control error. PC errors are usually modeled as lognormal random variables in dB scale.

Proper modeling and parameterization of signal propagation phenomena is an important aspect in CDMA network capacity studies. In general, radio channel effects can be divided into elements due to propagation path losses, slow fading (shadowing) and fast

fading. Path losses depend on the geographical environment (e.g., urban, rural, hilly) and cell size (macro, micro, pico) and type (outdoor, indoor). Average attenuation grows as a power law of distance. A path loss exponent of four is widely adopted in the literature. It is valid in a typical urban environment. A shadowing effect is usually analyzed at the system level, and the lognormal distribution provides generally a good fit. Fast fading can be taken into account at the link level as a required signal-to-noise ratio (SNR) for the predefined quality-of-service (QoS). The stronger the fading, the more signal-to-noise ratio is required for a given required bit error rate (BER). The influence of these propagation parameters is discussed, e.g., in [47].

The effects of user mobility on the CDMA capacity have been studied in [53]. In that work the results are based on simulations that take into account shadowing, call statistics, voice activity, cell sectorization and user mobility. Perfect power control and ideal antenna directivity are assumed. The presented concepts are general and they can be applied to any asynchronous CDMA cellular networks.

The impact of the carrier phase and chip timing errors to DS-CDMA capacity is evaluated in [54]. The joint effects of imperfections due to power control, channel parameter estimation, and spreading code estimation are taken into consideration in the performance evaluation of high chip rate CDMA system with multipath diversity combining in [55]. Paper [56] promises hot-spot traffic relief in cellular CDMA network by using tilted antenna approach. In [57], adaptive sectorization and non-uniform traffic are taken into consideration in the capacity evaluation.

A discussion of the Erlang capacity in a power controlled CDMA system is presented in [58]. Similar capacity gains, as reported in [12], are expected in the Erlang capacity as well. Reverse link Erlang capacity under nonuniform cell loading is documented in [59]. The effects of adaptive base station antenna arrays on CDMA capacity have been studied, e.g., in [46, 60, 61]. The results show that significant capacity gains can be achieved with quite simple techniques. Additional analysis of the outage probability in cellular CDMA is presented in [62, 63]. Both Nakagami and Rician fadings coupled with lognormal shadowing have been taken into account in the propagation model. Additionally, the voice activity factor is included in [62]. Paper [64] provides a simple generalization of the reverse link CDMA capacity under different spreading and interference conditions. Expressions of average external interference are discussed in [65]. The impact of power control to other-cell interference is evaluated in [66]. In [67], the effect of cochannel interference to CDMA capacity in a two-tier cellular system is studied.

The combined effects of soft handover, power control errors, and shadowing correlation are included in the CDMA performance studies of [68]. Soft handoff impact to CDMA capacity and coverage is evaluated in [69] and the relative portion of the other-cell interference of the total interference in a power-controlled cellular CDMA system in [70]. Capacity and radio resource sharing in hierarchical macro/micro-cell structures is studied in [71].

Paper [72] is devoted to the analysis of multiple cell DS-CDMA system performance with diversity reception. Multipath diversity is utilized in [73] for three differentially coherent receiver structures. A rake receiver was shown to improve the performance substantially in a moderately dispersive channel. Reverse link capacity in a power-controlled CDMA system, in the presence of multipath fading, is analyzed in [74]. Uniform and exponentially decaying power delay profiles have been assumed in single

and multiple cell scenarios. The numerical results indicate interesting tradeoffs in performance between these set-ups, depending on the chosen key parameters. Link reliability with multipath diversity is assessed in [75]. References [76, 77] also analyze CDMA performance in multipath channels. Bit error rate and user capacity of rake reception with maximal ratio combining (MRC) and equal gain combining (EGC) is evaluated in [78] in Nakagami fading. Imperfections in MRC are also modeled. In [79], a generalized rake receiver is proposed for interference mitigation in the wideband CDMA downlink. This receiver can use some of the fingers for interference suppression instead of increasing diversity. Significant performance and capacity gains over conventional rake receivers are reported. A two-dimensional rake receiver that utilizes both the spatial antenna diversity and the temporal multipath diversity is analyzed in [80]. Independent and correlated fading among receive antennas is assumed in a Nakagami- m fading environment.

A recent contribution [81] studies the effectiveness of spatial multiplexing in MIMO-CDMA systems with linear spatial receivers. It is shown that the (multiple-input multiple-output) MIMO outage capacity is severely degraded by the enhancement of the other-cell interference. Conventional single band (carrier) CDMA systems have gradually evolved to multicarrier implementations. The performance of single and multicarrier DS-CDMA is compared in [82]. System capacities in conventional DS-CDMA, multicarrier DS-CDMA and uplink synchronized multicarrier DS-CDMA systems are compared in [83]. The latter system is shown to clearly outperform the former schemes in a single cell capacity comparison with fast transmit power control.

In most of the previous references, it has been assumed that the service of interest is low rate speech. However, in the third generation and beyond systems mixed services, including multiple service classes (e.g., integrated voice/data, variable data rates), have to be taken into account. The performance of this kind of systems is evaluated, e.g., in [84–93]. Additional studies on the capacity of the third generation UMTS/WCDMA systems can be found in [94–102]. In references [103–110], the outage probability criterion is used as a metric to assess system capacity of CDMA radio networks.

The extensive list of references above demonstrates that CDMA capacity related research has been intensive during the last two decades. This thesis contributes to this area by presenting an analytical framework for the effective user capacity evaluation that addresses complex wideband CDMA signals, multipath fading, temporal and spatial diversity, enhanced receiver structures, and most of all takes into account the various system imperfections that are inevitable in the practical implementation.

2.2 Multiuser detection

Advanced wireless CDMA systems employing multiuser receivers have gained a lot of attention in the latest two decades. This research area has gradually emerged from a purely academic topic towards practical implementation. The third generation wideband CDMA (WCDMA) standard [111, 112] can be supplemented with this technology. A number of overview papers [112–120] discuss basic features of multiuser detection

(MUD) and interference cancellation (IC) techniques. They also offer classifications of different multiuser receiver structures.

Among linear interference cancellation schemes, decorrelating detectors [121–123] represent one important sub-category of multiuser receivers. The basic idea of the decorrelator is to use the inverted crosscorrelation matrix to remove interference caused by other active users, i.e., multiple access interference (MAI). With a perfect knowledge of crosscorrelations (based on the knowledge of code sequences and timing of all active users) the effect of all MAI can be eliminated at the cost of noise enhancement. One important benefit of the ideal decorrelator is that it does not require knowledge of the users' power levels (or amplitudes) and is thus resistant to power fluctuations. On the other hand, the complexity and the need for matrix inversion updates can create a bottleneck at high user loads and in fast fading environments. The crosscorrelation matrix must be estimated, which will lead to further impairments. An analogy with the operation of the zero-forcing equalizer and the decorrelating detector can be identified.

The capacity of decorrelating detectors is discussed in [124–134]. Papers [124, 125] analyze bit error performance and user capacity of linear multipath-decorrelating receivers in frequency-selective fading channels. Multipath-decorrelating maximal ratio and equal gain combiners are shown to outperform the plain rake receiver. The so-called pseudo-decorrelating multiuser receiver is introduced in [126]. It is evaluated in asynchronous multiple access case in the presence of synchronization errors in AWGN channel. The capacity of the linear decorrelating detector for quasi-synchronous CDMA is evaluated in [127]. It reports that at large processing gains the impact timing offset is very detrimental to the system capacity. As a low complexity alternative to multiuser detection, [128] proposes a hybrid diversity combining structure that is based on a one-shot decorrelating detector. Iterative implementation of the decorrelator for multipath combining in slowly-varying frequency-selective fading channel is investigated in [129]. Performance limits for full and partial decorrelation are assessed in [130]. The quasi-decorrelating detector is dealt with in [131, 132] where the impact of the specific spreading code families to bit error performance is quantified. In [133], an approximate decorrelator is analyzed based on the first order approximation to the inverse crosscorrelation matrix. In [134], Kawahara and Matsumoto analyze the asymptotic efficiencies of path-by-path and channel-matched decorrelators in asynchronous CDMA system with channel estimation. The impact of a fraction of chip time offset on the decorrelator capacity in AWGN channel is studied in [135]. Moreover, the performance of various spreading code sets is compared in this context.

In [136, 137], a CDMA system that is based on joint detection data estimation with coherent receiver antenna diversity is described and analyzed. This system can be used as a hybrid multiple access scheme with time division multiple access (TDMA) and frequency division multiple access (FDMA) components. Outage probability bounds when using a zero-forcing (ZF) multiuser detector are presented in [138]. Significant capacity gains are reported for ZF detectors over conventional single-user receivers.

Other linear multiuser receivers include minimum mean square error (MMSE) detectors [139–142] and linear implementations of interference cancellation [144–149]. According to the system capacity evaluation presented in [143], the MMSE detector can provide moderate gains over single user receiver, while the decorrelator is even inferior to the conventional receiver. In [144], a linear interference canceller is applied to a

microcellular CDMA and uplink capacities are estimated for different propagation scenarios.

Successive interference cancellation (SIC) and multistage SIC (MSIC) are discussed with respect to DS-CDMA system capacity in [150–159]. In addition, adaptive interference cancellation is described in [160].

Upper and lower bit error bounds for optimum multiuser detection are estimated in [161] on AWGN and fading channels for synchronous and asynchronous CDMA systems. Wiener filtering and parallel interference cancellation (PIC) are compared as interference suppression methods in [162]. Multistage PIC is utilized in [163] for the bit error probability analysis at the base station of a DS-CDMA system. The impact of phase jitter and timing errors is incorporated in the study. Paper [164] focuses on resource allocation and capacity studies of CDMA multiuser receivers that support multiple traffic classes (data rates, bit error rate requirements).

Combined effects of link and system level simulation results for wideband CDMA uplink capacity are investigated in [165, 166]. Nonlinear PIC multiuser detection is compared to the conventional rake reception with dual-antenna diversity and closed loop power control. The results show that with MUD efficiency of 65%, roughly a two-fold increase in capacity is achieved in comparison to a conventional receiver. The effect of the fractional cell load on the coverage of the wideband MUD-CDMA in the same framework is presented in [167]. The coverage of the uplink was observed to be less affected by the variation in cell loading than in conventional systems. Downlink capacity enhancements are discussed in [168].

Multiuser capacity versus bit error rate of various MUD structures with beamforming antenna arrays is compared in [169]. Spatial equivalence classes are employed, and the capacity is studied in AWGN and Rayleigh fading channels. Spatial diversity is used in [170] as well to enhance decorrelating detector performance in single path and multipath fading channels. The demonstrated capacity improvements are proportional to the number of receive antennas. Paper [171] presents a framework for the performance analysis of linear multisensor multiuser receivers. The potential correlation between antenna elements is accounted for. Already two diversity antennas are seen to be advantageous, especially if the channel is not multipath rich. A space-time MMSE (ST-MMSE) detector is offered in [172] as a solution to synchronous CDMA in multipath channels where conventional receivers perform poorly. Adaptive implementations are studied and multiuser performance is compared to that of single user bound and single user detector with correlated and uncorrelated antennas.

A noteworthy comparative overview of the simulated performances of several MUD receivers under similar assumptions is published in [173]. The chosen receiver structures are: 1) decorrelator, 2) MMSE receiver, 3) multistage PIC receiver, 4) SIC receiver, and 5) decorrelating decision feedback receiver. Estimation errors and complexity issues are also addressed. The results indicate that nonlinear MUD techniques provide the best performance when estimation is not an issue. Otherwise, the linear receivers perform better. Another comparative framework is shown in [174] where the spectral efficiency is the performance measure for alternative linear MUD receiver implementations. Information-theoretic aspects and large system analyses for multiuser detectors are conducted in [175–177].

The performance of the multiuser detector depends heavily on the channel parameter estimation. For these reasons, parameter estimation in multiuser communications has become an important research area, aiming at finding feasible solutions for practical MUD applications. The performance of linear decorrelating detectors in the presence of time delay, carrier phase and carrier frequency errors is analyzed in [178]. The low-complexity amplitude and phase estimation methods with known or unknown delays are analyzed in [179]. Joint signal detection and parameter estimation schemes (amplitudes and phases) are evaluated in [180]. Adaptive symbol and parameter estimation algorithms based on recursive least squares (RLS) and extended Kalman filters (EKF) have been studied in [181]. The sensitivity of multiple-access channels to various mismatches due to imperfect carrier recovery, timing jitter, and channel truncation is studied in [182]. The impact of timing (delay) errors to the performance of linear MUD receivers is illustrated in [183, 184]. Mostly the same authors have also considered the whole estimation problem in [185]. Sensitivity analysis of near-far resistant DS-SS receivers to propagation delay estimation errors in [186] shows that even quite small errors will destroy near-far resistance of the decorrelating detector. Joint amplitude and delay estimation is evaluated in [187] by using the extended Kalman filter and the same authors study quasi-synchronous CDMA systems applying linear decorrelators in [188].

The above references mainly study the link performances at quite limited code lengths and user populations. This is often necessary to ensure analytical tractability of the performance evaluation or to keep the complexity of simulations at a reasonable level. In a large-scale capacity evaluation, however, some simplifying assumptions and approximations are usually unavoidable in order to obtain results for heavily loaded systems utilizing long spreading codes. This thesis proposes some solutions for these conditions so that large user capacities can be quantified in favorable situations. The imperfections of the multiuser detection and interference cancellation are modelled and reflected in the numerical user capacity and sensitivity results.

2.3 Diversity methods

Paper [189] offers a useful introduction to multipath combining and basic principles of rake reception. A comprehensive review and classification of multipath diversity receiver techniques can be found in [190]. In addition, the well-known text book by Proakis [191] includes a sub-chapter of diversity techniques for fading multipath channels.

Equal gain combining is studied in [192–197]. Bit error rate performances of dual-branch M -ary phase shift keying (MPSK) diversity receivers with equal gain and selection combining in the presence of cochannel interference and various fading channels are evaluated in [192]. In addition, the accuracy of Gaussian approximation for the interference is assessed and confirmed to be good for small to medium range of SNR. Paper [193] provides an analytical framework to the expressions of equal gain diversity in Rayleigh, Rician, and Nakagami fading channels. Error performance in Rayleigh fading channels is investigated in [194–196], whereas [197] focuses on Doppler-spread Rician fading and differentially coherent PSK modulation.

Maximal ratio combining is discussed for example in [124, 198–215]. Linear multipath-decorrelating receivers in frequency-selective fading channels have been compared to the conventional rake receiver in [124]. It concludes that decorrelators can avoid error floors demonstrated by plain rake receivers. Performance of rake combining techniques (selection, equal gain and maximal ratio diversity) in the presence of chip and phase synchronization errors is reported in [198, 199]. As expected, the maximal ratio combiner outperforms other schemes and quite drastic capacity losses are seen due to synchronization errors and fading. Diversity methods in Rayleigh fading have also been evaluated and compared in [200, 201]. In [202], a novel method is applied to the performance evaluation of diversity reception with two correlated Rayleigh fading signals. A transformation is derived to convert two correlated signals to two independent signals. A moment generating function based numerical outage probability analysis is performed in [203] for the MRC and postdetection EGC diversity systems in generalized fading channels. Paper [204] presents simple iterative methods for blind MRC methods. Hybrid selection/maximal ratio combining is discussed in [205–208]. In [205], a so-called *virtual branch* technique is used to find out the mean of the combiner output SNR for any number of branches out of the total number of available diversity branches. Closed-form expressions for the symbol error probabilities in flat Rayleigh fading channels are derived in [206]. The impact of Gaussian distributed weighting errors on the performances of hybrid selection/MRC combiners is examined in [207]. Tradeoffs between diversity gain and performance losses are shown at variable orders of diversity branches. Additional results on this topic are provided in [208], where the upper and lower bounds of SNR penalty are evaluated in detail. The impact of fading correlation and unequal branch gains on the Shannon capacity is investigated in [209]. Average channel capacity for rake receivers is studied also in [210]. A tutorial paper [211] outlines a unified approach to performance assessment of digital communication over generalized fading channels. References [212–214] cover bit error rate studies for MRC diversity in correlated fading with channel estimation errors, weighting errors, and unequal mean powers. The impact of noisy channel estimates on MRC, EGC, and selection combiner (SC) is studied also in [215]. Three variations of MRC rake receivers are compared in [216] over Nakagami fading multipath environments.

The effect of tap spacing and chip waveform on the performance of DS spread spectrum rake receiver is analyzed in [217]. The multipath combining rule is based on a maximum-likelihood criterion. In [218], the generalized selection combining is studied in Rayleigh fading channels in terms of average combined SNR, outage probability, and average error rate. The more recent contribution [219] focuses on low-complexity combining in diversity-rich environments. The proposed scheme is called generalized switch and examine combining that can conserve the complexity as the number of available diversity paths increases. The combined benefit from the selective rake and best SNR scheduling diversity is evaluated in [220].

An extensive overview of space-time signal processing techniques in wireless communications is given in [221]. Smart antenna techniques and their potential applications are reviewed in [222]. The joint effect of transmit and receive diversity is studied in [223] by means of outage probability in a shadowing environment. Monte Carlo simulations confirm the closed-form derivations. A simple two-dimensional rake structure to increase capacity in antenna array CDMA systems is proposed in [224]. Paper

[225] evaluates the effect of finite antenna separation on the performance of MRC and EGC spatial (uniform linear antenna array) diversity receivers. A closed-form expression for the correlation as a function of antenna spacing in adaptive arrays is derived in [226]. Hotelling's generalized distribution is applied to the performance analysis of dual-antenna rake receivers in [227]. Letter [228] proposes an interference blocking space-time rake receiver to combat the strong interference in CDMA systems over multipath fading channels.

This work utilizes equal gain combining, maximal ratio combining, spatial diversity, and noncoherent partial rake combining. The novel contribution is related to the modeling of system parameter imperfections in the operation of these diversity techniques in fading multipath channels.

2.4 UWB systems

The online source [229] introduces and outlines milestones in the history of ultra wideband (UWB) technologies and applications. It lists down the early UWB references and patents from the 60s and 70s. In [230], a timely overview of ultra wideband wireless systems is given. It discusses, e.g., the Federal Communications Commission (FCC) allocation of 7.5 GHz (3.1–10.6 GHz) unlicensed band for the UWB devices. The potential UWB modulation schemes, multiple access issues, single vs. multiband implementation, and link budgets are also dealt with. Paper [231] is frequently referred to and gives a brief introduction to the basics of impulse radio systems. It describes the characteristics of impulse radio and gives analytical estimates of the multi-access capability under idealistic channel conditions. The potential scenarios anticipated for UWB technology are described in [232] from the European research and development perspective. A tutorial article [233] outlines the main features and elements in the physical layer of the UWB communication system. In addition, the article discusses some aspects of network topology. More information on the higher layer protocols, such as medium access control and packet scheduling, is available in [234]. A recently published doctoral thesis [235] also includes a review of the steps in UWB technology deployment, standardization, and regulation.

Some new channel capacity results for M -ary pulse position modulation (M-PPM) time hopping UWB systems are presented in [236]. It is demonstrated that the previous results based on the "pure PPM model" have overestimated the real UWB capacity. The proposed model is extended with the correlator and soft decision decoding. The capacity is evaluated in the single-user case and with asynchronous multiple user interference (MUI) when the inputs are equiprobable. It is found that larger M leads to increased capacity only at the high bit SNR region. Furthermore, optimal time offset values for each M are independent of the bit SNR. The MUI influence is detrimental for the capacity, especially at high bit SNRs.

Paper [237] focuses on the UWB indoor channel modeling issues. The measurement data is collected from an extensive campaign in a typical modern office building with a 2 ns delay resolution. The model is formulated as a stochastic tapped delay line (STDL). The energy statistics due to small-scale effects seem to follow a Gamma distribution for

all bins. Large-scale parameters can be modeled as stochastic parameters that can change, e.g., from room to room. UWB propagation channels are the topic of [238]. Based on the modified CLEAN algorithm, estimates of time-of-arrival, angle-of-arrival, and waveform shape are derived. Key parameters of the model are intercluster decay rate, intracluster decay rate, cluster arrival rate, ray arrival rate, and standard deviation of the relative azimuth arrival angles. Intercluster signal decay rate is generally determined by the architecture of the building. Intracluster decay rate, on the other hand, depends on the objects close to the receive antenna (e.g., furniture). Relative azimuth arrival angles were best suited to a Laplacian probability density function. Saleh and Valenzuela [239] present a model that has become a frequently referred to and adopted source in indoor multipath propagation channel modeling. They propose a statistical indoor radio channel model that 1) has the flexibility to reasonably fit with the measured data, 2) is simple enough to be used in simulation and analysis, and 3) can be extended by adjusting the parameters to represent various buildings. In the developed statistical model the rays of the received signal arrive in clusters. The ray amplitudes are independent Rayleigh random variables with exponentially decaying variances with respect to the cluster delay and the ray delay. The clusters and the rays within the cluster form Poisson arrival processes with different, fixed rates. The modification of the Saleh-Valenzuela model to UWB propagation channel models is introduced in [240]. Paper [241] characterizes measurement-based ultra-wide bandwidth wireless indoor channels from the communications theoretic viewpoint. The bandwidth of the signal used in the measurement is over 1 GHz resulting in less than 1 ns time resolution. The robustness of the UWB signal to multipath fading is quantitatively evaluated through histograms and cumulative distributions. Two rake structures are introduced: the all rake serves as the best-case (benchmark) receiver and the maximum-energy-capture selective rake is a realistic sub-optimal approach. The multipath components of the measured waveforms are detected using a maximum-likelihood estimator based on a separable specular multipath channel model.

The performance of PPM and on-off keying (OOK) binary block-coded modulation formats using a maximal ratio combining rake receiver is studied analytically in [242]. The trade-off between receiver complexity and performance is examined. Several suboptimal receivers in indoor multipath AWGN channels have been employed. Results indicate that the robust performance may require increase in rake complexity. This implies allocation of more rake fingers and tracking of the strongest multipaths to help in the selection combining. Rake performance for a pulse-based high data rate UWB system in an Intel Labs indoor channel model is addressed in [243]. It is noted that at low input SNR values (0–10 dB) and with a low number of rake fingers, it is more beneficial to add rake fingers for energy capture rather than for intersymbol interference (ISI) mitigation. In the presence of channel estimation errors, equal gain combining can be more tolerant than maximal ratio combining, and therefore yield better performance [243]. In order to quantify the trade-off between rake receiver energy capture and diversity order, [244] presents a partly quasi-analytical and partly experimental analysis suited to dense multipath propagation environments. Numerical results show that a diversity level of less than 50 is adequate in typical indoor office conditions. Paper [245] studies the optimal number of rake fingers to be employed in time hopping (TH) and direct sequence selective rake UWB systems at various multipath combining techniques. The impact of

exponentially decaying power delay profile to the performance of selective rake combining in Rayleigh fading is evaluated in [246]. In addition, partial band interference effects are studied.

In [247], a method to evaluate bit error rate (BER) performance of time hopping PPM in the presence of multiuser interference and AWGN channel is proposed. Gaussian quadrature rules are used in this approach. Paper [248] concentrates on the signal design for binary UWB communications in dense multipath channels. The aim is to find signals with good distance properties leading to smooth BER performance that both depend on the time shift parameter. The performance of UWB correlation receivers for equal mean power Gaussian monocycles is studied in [249]. Channel conditions vary among ideal single user AWGN, non-ideal synchronous, multipath fading and multiple access interference. It is shown that the pulse shape has a notable impact on the correlation receiver performance. The effects can be seen in the autocorrelation function, especially in the mainlobe. The autocorrelation is closely related to the SNR gain of the output and to interference resistance properties. The special characteristics of the Gaussian monocycles include the following descriptions: 1) higher order derivatives have higher SNR gain in single user and in asynchronous multiple access channels, but are less robust to interference than lower order derivatives, 2) narrower pulses have higher SNR gain in asynchronous multiple access channels at the cost of inferior interference resistance ability. Exact bit error rate performance of TH-PPM UWB systems in the presence of multiple access interference is analyzed and simulated in [250]. Furthermore, it is shown that with a moderate number of MAI sources the standard Gaussian approximation becomes inaccurate at high SNRs. The usage of space-time coding in single band UWB is analyzed in [251], where performance gains against single link scheme are reported. In addition, high resistance to timing jitter is observed. Three different UWB modulation schemes are compared in a multipath environment in [252]. These modulation techniques are based on timing hopping and direct sequence schemes with either bit flipping or pulse-position modulation. The numerical results confirmed that bit flipped modulation is better in terms of average BER and outage probability.

The main principles for multi-access in UWB systems are discussed in [253]. A functional medium access, radio link and radio resource control architecture is proposed and open issues for future activities are addressed. Numerical throughput and delay performance results in radio resource sharing are shown. Uncoded and coded performance analyses for TH-UWB systems are covered in [254], where a practical low-rate error correcting coding scheme that does not require bandwidth expansion, is presented. The Gaussian assumption for multiuser interference is shown to be invalid for high uncoded data rates. The user capacity increases radically with the proposed coding scheme. Contribution [255] extends the analysis to general M -ary PPM modulation and quantifies exact MUI and Gaussian approximated MUI results in capacity versus symbol error rate results. M -ary signals ranging from $M = 2$ up to $M = 256$ are used in [256], together with PPM signal formats in the UWB multiple access capacity analysis. Performance is analyzed in free-space propagation conditions, where the number of supported users depends on the given bit error rate, SNR, transmission rate, and modulation alphabet size. Furthermore, performance and receiver complexity trade-off is discussed. Upper bounds are derived for the combinations of user capacity and total transmission rate. According to the numerical examples, it is possible to achieve a system

with high capacity and data rate, low bit error probability, and yet only moderate receiver complexity.

Reference [257] is one of the first pivotal UWB papers outlining the potential of time hopping impulse radio multiple access communications. It describes the basic building blocks of the impulse transmitter and receiver, and their mathematical formulations. It also shows an example of the bit error rate versus user capacity estimate at variable data rates. Finally, some drawbacks of the high time-resolution impulse radio systems are mentioned: 1) the need for up to thousands of rake fingers in the multipath receiver, and 2) complex initial clock acquisition. In [258], a quite comprehensive overall description of time hopping UWB system physical layer issues is given. Achievable transmission rates and multiple access capacities are estimated for analog and digital modulation formats. Numerical results indicate that the digital implementation has potential to nearly one order of magnitude higher user densities than the analog one. Paper [259] defines a signal-to-(noise+interference) ratio based framework for the analysis of TH-UWB communication systems. Specific attention is paid to hopping sequences and synchronization issues in AWGN and lognormal fading channels.

The authors of [260–262] have established a reference scenario and framework for indoor master-slave UWB network and evaluated outage probability restricted system capacity with and without power control. Performances of high data rate direct sequence spread spectrum (DS-SS) and multiband OFDM¹ (MBO) UWB piconets are compared in [263] in terms of link outage probability and average aggregate network throughput. Numerical examples indicate that DS-SS modulated scheme has a better link reliability at small number of frequency hops, while the MBO outperforms it with a large number of hops. The multiuser DS-UWB system performance, with random ternary sequences, is analyzed in [264]. Such issues as processing gain, jamming margin, coding gain, and multiuser interference are studied for a single-user matched filter receiver. Antipodal DS-UWB system performance and capacity is analyzed in [265] under imperfect power control. Space-time selective rake combining and finger allocation strategies are proposed and compared in [266]. One of the evaluated methods is specifically targeted to narrowband interference mitigation. Variable bit rate multiclass time hopping [267] and direct sequence [268] UWB systems are analyzed in terms of outage probability and bit error rate. DS-UWB is characterized in [269] in the presence of multipath, multiuser, and narrowband interference. The impact of the various spreading code families to the system performance and capacity is also evaluated. An overview to the candidate multiplexing techniques for multiple UWB piconets is given in [270]. The main conclusion in the article is that code division multiplexing seems to be the most promising alternative between multiple piconets. Papers [271–273] are related to the multiple access performance assessment and code selection in synchronous and asynchronous UWB networks. Reference [271] compares performance of time hopping modulation and signaling variants, whereas [272, 273] include binary direct sequence modulation too. The problem of time hopping code design is addressed in [274], having cyclic correlation as a performance measure. The multiple access capacity of a novel delay-hopped transmitted reference UWB system in rich multipath environment is discussed in [275]. The relation of binary time hopping sequences correlation function and MAI is analyzed

¹ OFDM = orthogonal frequency division multiplexing

and simulated in [276]. Secure wireless sensor networks are evaluated in [277]. Binary direct sequence spread spectrum and pulse position modulated UWB schemes are compared. Localization aspects for future sensor networks are discussed in [278].

Reference [279] is focused on MUD possibilities for direct sequence UWB systems. It is demonstrated that the adaptive MMSE MUD receiver outperforms the rake receiver both in energy capture and in the interference rejection sense. The studied interference sources are narrowband IEEE 802.11a interference and multiuser UWB interference. Ideally, an MMSE receiver can achieve AWGN bit error rate within a 1–2 dB margin even in dense multipath channels. In heavily loaded conditions the penalty of 6 dB is experienced, but at the same time the rake receivers suffer from unacceptable error floors. An iterative partial PIC is applied to the UWB multiuser system in [280]. The matched filter, maximum-likelihood, and linear minimum mean squared error receivers are also used in the performance comparison. In this paper, multiuser detection is combined with error control coding. The UWB system includes only one pulse per symbol and AWGN channel is assumed. The numerical results show that it is possible to attain the coded single user BER bound for 8–15 users in a heavily loaded system without any processing gain. As the number of users increases and the bandwidth to pulse repetition frequency decreases, MAI is expected to adversely affect system capacity and performance. As a consequence, a framework for the design of multiuser detectors for UWB multiple access communications systems is presented in [281]. Optimum multiuser detector is also proposed. As an alternative to impulse radio, [282] discusses a multistage frequency hopping multiple access scheme that allows for dividing the huge pool of potential users to smaller groups that are free of interference from the other groups. Paper [283] focuses on synchronization, channel estimation, and detection issues in biphase DS-CDMA impulse radio systems. Both the time and frequency domains are used in the reception process. It is shown that the interference cancellation receivers can significantly outperform conventional rake receivers that do not have an interference suppression property. The applicability of minimum variance multiuser detection for UWB systems is evaluated in [284]. The same authors investigate subspace MUD in [285].

The coexistence of UWB systems with some other radio systems is studied in [286]. The study includes the evaluation of interference caused by the UWB system to the other radio systems, and vice versa. The coexisting radio concepts are GSM900, UMTS/WCDMA, and global positioning system (GPS). Several short Gaussian based UWB pulses are employed. According to the numerical results, convenient selection of pulse waveform and width leads to interference resistance up to a certain limit. The pulse shape is in interaction with the data rate. High-pass filtered waveforms are preferred in the case of short UWB pulses, whereas generic Gaussian ones are favorable if long pulses are utilized. Interference caused by narrowband systems is the most detrimental to UWB if it is located at the UWB system's nominal center frequency. In the GPS band the DS based UWB system interfered less than the time hopping system. This reference is one of the key contributions in [235] where coexistence of UWB with selected existing radio systems is discussed even more thoroughly.

Channel estimation for time hopping UWB communications is dealt with in [287], where multipath propagation and MAI are taken into consideration. Maximum-likelihood estimation is applied in data-aided and nondata-aided scenarios. Numerical results show that the performance is reasonable if the number of simultaneous users is below 20. The

impact of the timing jitter and tracking to the impulse radio system performance is investigated in [288] using binary and 4-ary modulations. According to these studies, both modulations suffer from the jitter, however 4-ary being better. Timing jitter is also discussed in [289] where static and Rayleigh fading channels are assumed. Orthogonal PPM, optimum PPM, OOK and BPSK modulations are compared in performance evaluation. Similar performance degradation is noted for BPSK and PPM schemes, while OOK is more susceptible to large jitter. Probability density function of timing jitter due to rake finger estimation is simulated. The results depend on the pulse shape and SNR. The worst case distribution is shown to provide an upper bound for BER performance.

The present thesis provides a framework for multiple access capacity assessment in indoor DS-UWB cellular configurations. New models for link distance statistics in different cell shapes and network topologies are derived and simulated. In addition to multiple access interference the contributions of multipath, desired user interpath interference, path loss, and timing errors are uniquely modeled in this framework.

2.5 Lognormal sum approximations

Lognormal power sums need to be resolved often in mobile radio communications. Long-term shadowing effects in many practical cellular systems agree closely with a lognormal model. Furthermore, short-term channel amplitude fluctuations may also fit into lognormal distribution (e.g., in the case of ultra wideband). Sums of multiple signals will be realized in the presence of cochannel interference.

Closed-form solutions for the sum distributions of multiple lognormal signals are not known. Therefore, several approximations have been derived for this purpose. Perhaps the best-known proposals are the Fenton–Wilkinson (FW) [290] and Schwartz–Yeh (SY) [291] methods. Both schemes model the sum of multiple lognormal random variables by another lognormal random variable. The FW approach is attractive due to its simplicity. As a drawback, this method provides reasonable accuracy for the first two moments (mean and variance) at small dB spreads (< 4 dB) only. However, some practical problems (such as outage probability) require merely the right-tail distribution where the FW method can give a good match, even at larger dB spreads. The SY approximation provides the exact mean and standard deviation for the sum of two lognormal random variables. Then, nesting and recursion techniques are used to estimate the power sum for greater number of signals. In many instances, the SY procedure is more accurate than the FW approach. It suits signals with large standard deviations also. The main drawback of this method is the complexity associated with the calculus. These approximations have been used in cellular radio performance assessment, e.g., in [292]. The original approximations were intended to sums of uncorrelated random variables. Extensions to correlated random variables have been presented in [293–295]. In [293], Ho also introduces a computationally efficient numerical integration routine as a modification to the SY approximation.

Cardieri and Rappaport [296, 297] have done statistical analysis and comparison of FW and SY approximations for lognormal summands having different mean values and standard deviations, also accounting for the possible correlation between signal

components. Their results indicate that the FW approximation is poor when the standard deviations of the summands are clearly different. The SY approximation shows excellent accuracy in wide range of the numerical examples. In [298], the author of this thesis has examined the applicability of the FW and SY methods for power sums of correlated random variables with different means and variances. It was found that both approximations can become highly inaccurate in the case of heterogeneous sets of correlated summands. Contributions [299] and [300] are related to the user signal-to-interference ratio calculations in the presence of generically correlated lognormal interferers. In the same context, extensions to the FW and SY approaches have been derived.

In addition to these frequently cited approaches, there are some other noteworthy approximations for the sums of lognormal components. Farley's approximation [291, 301–303] is one of these. In [301], it is stated that Farley's approximation is a strict lower bound for the cumulative distribution function (CDF) of a sum of independent lognormal random variables. This implies that if Farley's estimate of a CDF value is larger than any other estimate, it is more accurate. Furthermore, it is claimed in [291] that this method is easy to apply and is appropriate for lognormal distributions with large dB spreads (i.e., standard deviation $\sigma > 10$ dB).

Schleher's cumulants matching approach was originally presented in [304]. It is based on the division of the sum CDF to a few regions and applying lognormal approximations in each region. The approximation method is a generalized Gram-Charlier series. Six error correction terms are included in the original scheme: however in [294] they were omitted due to convergence problems. The extension to the case of correlated lognormal random variables is presented in detail in [294]. The cumulants matching approach is rather complex to apply but it is accurate for lognormal sums with small and medium standard deviation components ($\sigma \leq 6$ dB). However, the FW method gives almost identical results in that range.

A general method for arbitrary distributions is described in [305]. It is based on the computation of the probability density function (PDF) of a power sum of two random variables that is referred to as *logarithmic convolution*. Recursion can be used to extend the method for larger number of components as in the SY approximation. In [305], the method was compared to the SY and the FW methods and results were crosschecked with Monte Carlo simulations in the case of lognormal component distributions. The results showed an almost perfect match with theoretical and simulated sum PDFs. The method seems to be very practical and it is not restricted to any specific PDFs or dB spreads. This approach is particularly useful when a large number of components exists and an effective integration routine is available.

The authors of [306] and [307] have expressed a simplified method to account for the cochannel effects of lognormal shadowing and Rayleigh fading. In the case of lognormal fading only, their approach has been compared to SY approximation and Monte Carlo simulations. A fairly close match was found with respect to both methods.

Recently, a new accurate and simple closed-form approximation to lognormal sum densities and cumulative distributions has been published [308]. This new paradigm is based on a low order curve fitting on lognormal probability paper. The idea is a further development of the minimax approximation discussed in [309] and [310].

Another novel approximation for the sum of independent non-identically distributed lognormal signals is described in [311]. Instead of matching the first two moments of the lognormal components, the idea is simply to match the moments of inverse exact sum. The new approximation is shown to outperform FW and SY approximations in the selected numerical examples.

Paper [312] discusses a case where both the desired signal and interference is composed of multiple correlated components. A simple method for estimating the correlation coefficient between total useful and total interfering signals, as a function of the correlation between the individual components, is derived.

A novel method to lognormal sum calculation of independent, but not necessarily identical summands, is given in [313]. There the lognormal sum is approximated by matching the moment generating function (MGF) of the sum with that of a single lognormal random variable suitably parameterized. Approximate Gauss-Hermite expansion of the lognormal MGF is used. The computational complexity is claimed to be comparable to the SY approach. Flexibility to emphasize accuracy in either head or tail of the distribution is one of the inherent advantages of this method in comparison to the FW and SY schemes.

Log shifted gamma (LSG) lognormal sum approximation is proposed in [314]. Its main idea is to use a shifted Gamma distribution in logarithmic domain to derive a probability density function to approximate the sum of multiple components. Cumulative distribution functions are compared with simulations, SY & FW methods, minimax approximation, and Farley's approximation. The results indicate that the LSG approximation outperforms others, especially when the number of summands and/or divergence of their statistics is large.

Additional theoretical insights to lognormal sums can be found in [315–318]. As an example, paper [315] defines upper and lower bounds on the distribution function of a sum of independent lognormal random variables.

This work makes use of the FW and SY approximations in such UWB scenarios that they have seldom been used so far. They require intricate combinations of signal components due to large number of users and multipath rich channel that brings on many multipath and interpath interference components to encounter for in the resulting sum of lognormal contributions. Luckily, the simple FW approximation turns out to be accurate enough in most of the studied numerical cases. In the exceptional cases (such as correlated multipaths), Monte Carlo simulations are used to verify the results.

3 Signal and channel models for the wideband CDMA framework

This chapter presents mathematical models for the transmitted and the received complex wideband CDMA signals (Section 3.1). The applied multipath channel profile modeling is briefly discussed in Section 3.2. The derivations in this chapter follow closely the structure presented in [2], which is an extension of the system model in [1].

3.1 Transmitted and received waveforms

The complex envelope of the signal transmitted by user $k \in \{1, 2, \dots, K\}$ in the n th symbol interval $t \in [nT, (n+1)T]$ is written as

$$s_k = A_k e^{j\phi_{k0}} S_k^{(n)}(t - \tau_k), \quad (1)$$

where A_k is the transmitted signal amplitude of user k , τ_k is the signal delay, ϕ_{k0} is the transmitted signal carrier phase. K is the total number of active users and T is the symbol interval. $S_k^{(n)}(t)$ is represented by

$$S_k^{(n)}(t) = S_k^{(n)} = S_k = S_{ik} + jS_{qk} = d_{ik}c_{ik} + jd_{qk}c_{qk}, \quad (2)$$

$$d_{ik} = b_{ik}^{(n)}\varphi(t - nT), \quad (3)$$

$$c_{ik} = \sum_{g=0}^{G-1} c_{ikg}^{(n)}\psi(t - gT_c), \quad (4)$$

$$d_{qk} = b_{qk}^{(n)}\varphi(t - nT - \varepsilon_b T), \quad (5)$$

$$c_{qk} = \sum_{g=0}^{G-1} c_{qkg}^{(n)} \psi(t - gT_c - \varepsilon_c T_c). \quad (6)$$

In equations (1)–(6), $b_{ik}^{(n)}$ is the data bit of the in-phase (I) channel and $b_{qk}^{(n)}$ is the data bit of the quadrature (Q) channel, $G = T/T_c$ is the number of chips per symbol, i.e., the processing gain due to direct sequence spreading, $\varphi(t)$ represents the bit pulse shape and ε_b is the relative bit offset of the Q-channel with respect to the I-channel. Parameters $c_{ikg}^{(n)}$ and $c_{qkg}^{(n)}$ are the g th chips of the k th user pseudo-noise spreading codes in the I- and Q-channel, respectively. $\psi(t)$ is the chip pulse shape and ε_c is the chip offset of the Q-channel relative to the I-channel. In practical applications, ε_b and ε_c will have values either 0 or $1/2$.

Equations (1)–(6) are general and different combinations of the signal parameters cover most of the signal formats of practical interest. E.g., in the WCDMA frequency-division duplex (FDD) mode the uplink signal format can be expressed as

$$(c_d d_d + j c_c d_c) c_s c_{ls}, \quad (7)$$

where c_d and c_c are data and control channel codes, d_d and d_c data and control channel information bits and, c_s and c_{ls} scrambling and (optional) long scrambling codes. Equation (7) can be written in the form of (2) with the following mapping

$$\begin{aligned} c_{ik} &= c_d c_s c_{ls}, \\ c_{qk} &= c_c c_s c_{ls}, \\ d_{ik} &= d_d, \\ d_{qk} &= d_c. \end{aligned} \quad (8)$$

Due to antenna diversity and multipath propagation, the vector channel impulse response consists of discrete multipath components represented as

$$\mathbf{h}_k^{(n)}(t) = \sum_{l=1}^L \mathbf{h}_{kl}^{(n)} \delta(t - \tau_{kl}^{(n)}) = \sum_{l=1}^L \mathbf{H}_{kl}^{(n)} e^{j\phi_{kl}} \delta(t - \tau_{kl}^{(n)}), \quad (9)$$

$$\mathbf{h}_{kl}^{(n)} = \mathbf{H}_{kl}^{(n)} e^{j\phi_{kl}}, \quad (10)$$

where L is the number of multipath components of the channel, $\mathbf{h}_{kl}^{(n)} = (h_{kl1}^{(n)}, h_{kl2}^{(n)}, \dots, h_{klM}^{(n)})^T$ is the vector of complex coefficients (gains) of the signal received over the l th path of user k at symbol interval n , $\tau_{kl}^{(n)} \in [0, T_m)$ is the delay of the

same component, and $\delta(t)$ is the Dirac delta function. It is assumed that T_m is the maximum delay of the channel. In the following analysis, indices n will be dropped whenever it is possible without ambiguity. It is also assumed that condition $T_m < T$ is satisfied, meaning that harmful intersymbol interference (ISI) can be avoided.

Let us assume a generic spatial diversity system having M receive antennas. In this case, the overall received signal during N_b symbol intervals in the m th antenna, $m \in \{1, 2, \dots, M\}$, can be represented as

$$\begin{aligned} r_m(t) &= \text{Re} \left\{ e^{j\omega_0 t} \sum_{n=0}^{N_b-1} \sum_{k=1}^K s_k^{(n)}(t) * h_{km}^{(n)}(t) \right\} + \text{Re} \left\{ z_m(t) e^{j\omega_0 t} \right\} \\ &= \text{Re} \left\{ e^{j\omega_0 t} \sum_{n=0}^{N_b-1} \sum_{k=1}^K \sum_{l=1}^L a_{klm} S_k^{(n)}(t - nT - \tau_k - \tau_{klm}) \right\} + \text{Re} \left\{ z_m(t) e^{j\omega_0 t} \right\}, \end{aligned} \quad (11)$$

where $h_{km}^{(n)}(t)$ is the m th row of $\mathbf{h}_k^{(n)}(t)$, $a_{klm} = A_k H_{klm}^{(n)} e^{j\Phi_{klm}} = A_{klm} e^{j\Phi_{klm}}$, $A_k H_{klm}^{(n)} = A_{klm}$, $\Phi_{klm} = \phi_0 + \phi_{k0} - \phi_{klm}$, ϕ_0 is the frequency downconversion phase error and $z_m(t)$ is a complex zero-mean additive white Gaussian noise process with two-sided power spectral density σ^2 and ω_0 is the angular carrier frequency. In the following, the noise term will be dropped for the sake of simplicity, and the focus will be only on the proper representation of multiple access interference (MAI). For a correct representation of the overall signal, the noise term will be reintroduced again in (39).

The complex matched filter of user k will create two correlation functions for each path and antenna. By omitting the noise terms, the I-channel signal becomes

$$\begin{aligned} y_{iklm}^{(n)} &= \int_{nT+\tau_k+\tau_{klm}}^{(n+1)T+\tau_k+\tau_{klm}} r_m(t) c_{ik}(t - nT - \tau_k + \tau_{klm}) \cos(\omega_0 t + \tilde{\Phi}_{klm}) dt \\ &= \sum_{k'} \sum_{l'} \sum_{m'} A_{k'l'm'} \left[d_{ik'} \rho_{ik'l'm',iklm} \cos \varepsilon_{k'l'm',klm} + d_{qk'} \rho_{qk'l'm',iklm} \sin \varepsilon_{k'l'm',klm} \right] \\ &= \sum_{k'} \sum_{l'} \sum_{m'} y_{iklm}(k'l'm'), \end{aligned} \quad (12)$$

where $\tilde{\Phi}_{klm}$ is the estimate of Φ_{klm} and

$$\begin{aligned} y_{iklm}(k'l'm') &= y_{iiklm}(k'l'm') + y_{iqklm}(k'l'm') \\ &= A_{k'l'm'} \left[d_{ik'} \rho_{ik'l'm',iklm} \cos \varepsilon_{k'l'm',klm} + d_{qk'} \rho_{qk'l'm',iklm} \sin \varepsilon_{k'l'm',klm} \right] \end{aligned} \quad (13)$$

Similarly, for the Q-channel the correlation function can be formulated as

$$\begin{aligned}
y_{qklm}^{(n)} &= \int_{nT+\tau_k+\tau_{klm}}^{(n+1)T+\tau_k+\tau_{klm}} r_m(t) c_{qk}(t-nT-\tau_k+\tau_{klm}) \sin(\omega_0 t + \tilde{\Phi}_{klm}) dt \\
&= \sum_{k'} \sum_{l'} \sum_{m'} A_{k'l'm'} \left[d_{qk'} \rho_{qk'l'm',qklm} \cos \varepsilon_{k'l'm',klm} - d_{ik'} \rho_{ik'l'm',qklm} \sin \varepsilon_{k'l'm',klm} \right] \\
&= \sum_{k'} \sum_{l'} \sum_{m'} y_{qklm}(k'l'm')
\end{aligned} \tag{14}$$

with

$$\begin{aligned}
y_{qklm}(k'l'm') &= y_{qqklm}(k'l'm') + y_{qiklm}(k'l'm') \\
&= A_{k'l'm'} \left[d_{qk'} \rho_{qk'l'm',qklm} \cos \varepsilon_{k'l'm',klm} - d_{ik'} \rho_{ik'l'm',qklm} \sin \varepsilon_{k'l'm',klm} \right].
\end{aligned} \tag{15}$$

Terms $\rho_{x,y}$ are crosscorrelation functions between the corresponding code components x and y . A scaling factor $1/2$ is dropped in the above equations for simplicity. Basically, dropping this coefficient for both the signal and the noise will not affect the signal-to-noise ratio (SNR) that determines the system performance. Each of these components is defined with four indices. Parameter $\varepsilon_{a,b} = \Phi_a - \tilde{\Phi}_b$, where a and b are defined with three indices.

Let the LM -element vectors $\mathfrak{Z}^{LM}(\cdot)$ of matched filter output samples for the n th symbol interval be defined as

$$\mathbf{y}_{ik}^{(n)} = \mathfrak{Z}^{LM}(y_{iklm}^{(n)}) = (y_{ik11}^{(n)}, y_{ik12}^{(n)}, \dots, y_{ik1M}^{(n)}, y_{ik21}^{(n)}, \dots, y_{ikLM}^{(n)})^T \in \mathbb{C}^{LM}, \tag{16}$$

$$\mathbf{y}_{qk}^{(n)} = \mathfrak{Z}^{LM}(y_{qklm}^{(n)}) = (y_{qk11}^{(n)}, y_{qk12}^{(n)}, \dots, y_{qk1M}^{(n)}, y_{qk21}^{(n)}, \dots, y_{qkLM}^{(n)})^T \in \mathbb{C}^{LM}, \tag{17}$$

$$\mathbf{y}_k^{(n)} = \mathbf{y}_{ik}^{(n)} + j\mathbf{y}_{qk}^{(n)}, \tag{18}$$

$$\mathbf{y}^{(n)} = \mathfrak{Z}^K(\mathbf{y}_k^{T(n)}) \in \mathbb{C}^{KLM}, \tag{19}$$

$$\mathbf{y} = \mathfrak{Z}^{N_b}(\mathbf{y}^{T(n)}) \in \mathbb{C}^{N_b KLM}. \tag{20}$$

Let in general $\mathbf{R}^{(n)}(i) \in (-1, 1]^{KLM \times KLM}$ be a crosscorrelation matrix with the following partition

$$\mathbf{R}^{(n)}(i) = \begin{pmatrix} \mathbf{R}_{1,1}^{(n)}(i) & \mathbf{R}_{1,2}^{(n)}(i) & \cdots & \mathbf{R}_{1,K}^{(n)}(i) \\ \mathbf{R}_{2,1}^{(n)}(i) & \mathbf{R}_{2,2}^{(n)}(i) & \cdots & \mathbf{R}_{2,K}^{(n)}(i) \\ \vdots & \vdots & \ddots & \vdots \\ \mathbf{R}_{K,1}^{(n)}(i) & \mathbf{R}_{K,2}^{(n)}(i) & \cdots & \mathbf{R}_{K,K}^{(n)}(i) \end{pmatrix} \in \mathbb{R}^{KLM \times KLM} \quad (21)$$

$$= \mathfrak{I} \mathfrak{I}^K \left(\mathbf{R}_{k,k'}^{(n)}(i) \right).$$

For the final representation of the complex matched filter output signal, to be given later by (53) and (54), four specific matrices in the form of (21) will be defined with the following notation

$$\mathbf{R}^{ii(n)}(i) = \mathfrak{I} \mathfrak{I}^K \left(\mathbf{R}_{k,k'}^{ii(n)}(i) \right), \quad (22)$$

$$\mathbf{R}^{qi(n)}(i) = \mathfrak{I} \mathfrak{I}^K \left(\mathbf{R}_{k,k'}^{qi(n)}(i) \right), \quad (23)$$

$$\mathbf{R}^{iq(n)}(i) = \mathfrak{I} \mathfrak{I}^K \left(\mathbf{R}_{k,k'}^{iq(n)}(i) \right), \quad (24)$$

$$\mathbf{R}^{qq(n)}(i) = \mathfrak{I} \mathfrak{I}^K \left(\mathbf{R}_{k,k'}^{qq(n)}(i) \right), \quad (25)$$

where matrices $\mathbf{R}_{k,k'}^{ab(n)}(i) \in \mathbb{R}^{LM \times LM}$, $\forall k, k' \in \{1, 2, \dots, K\}$ in (22)–(25) have elements

$$\left(\mathbf{R}_{k,k'}^{ii(n)}(i) \right)_{lm, l'm'} = \cos \varepsilon_{k'l'm', klm} \times \int_{-\infty}^{\infty} c_{ik}^{(n)}(t - \tau_k - \tau_{klm}) c_{ik'}^{(n-i)}(t + iT - \tau_{k'} - \tau_{k'l'm'}) dt, \quad (26)$$

$$\left(\mathbf{R}_{k,k'}^{qi(n)}(i) \right)_{lm, l'm'} = \sin \varepsilon_{k'l'm', klm} \times \int_{-\infty}^{\infty} c_{qk}^{(n)}(t - \tau_k - \tau_{klm}) c_{ik'}^{(n-i)}(t + iT - \tau_{k'} - \tau_{k'l'm'}) dt, \quad (27)$$

$$\left(\mathbf{R}_{k,k'}^{iq(n)}(i) \right)_{lm, l'm'} = -\sin \varepsilon_{k'l'm', klm} \times \int_{-\infty}^{\infty} c_{ik}^{(n)}(t - \tau_k - \tau_{klm}) c_{qk'}^{(n-i)}(t + iT - \tau_{k'} - \tau_{k'l'm'}) dt, \quad (28)$$

$$\left(\mathbf{R}_{k,k'}^{qq(n)}(i) \right)_{lm, l'm'} = \cos \varepsilon_{k'l'm', klm} \times \int_{-\infty}^{\infty} c_{qk}^{(n)}(t - \tau_k - \tau_{klm}) c_{qk'}^{(n-i)}(t + iT - \tau_{k'} - \tau_{k'l'm'}) dt, \quad (29)$$

$\forall l, l' \in \{1, 2, \dots, L\}$ and $\forall m, m' \in \{1, 2, \dots, M\}$.

In order to simplify notation, (26) is presented as $R = \rho \cos \varepsilon$ and its estimate as

$$\hat{R} = \hat{\rho} \cos \hat{\varepsilon}, \quad (30)$$

where ρ represents crosscorrelation. In general, the estimated phase difference $\hat{\varepsilon}$ between two users (e.g., users with indices $k = 1$ and $k = 2$) can be represented as

$$\hat{\varepsilon} = \phi_1 - \Delta\phi_1 - \phi_2 - \Delta\phi_2 = \varepsilon + \Delta\varepsilon, \quad (31)$$

where $\varepsilon = \phi_1 - \phi_2$ and $\Delta\varepsilon = -(\Delta\phi_1 + \Delta\phi_2)$.

If $\Delta\phi$ is a Gaussian process with zero-mean and variance σ_ϕ^2 , then $\Delta\varepsilon$ is a zero-mean Gaussian process with variance $2\sigma_\phi^2$. The estimated correlation function can be represented as

$$\hat{\rho} = \rho + \Delta\rho \cong \rho + \rho'\varepsilon_\tau = \rho \left(1 + \frac{\rho'\varepsilon_\tau}{\rho} \right) = \rho(1 + s_\rho), \quad (32)$$

where ρ' is the slope of the ρ function at the point of zero delay estimation error and

$$\varepsilon_\tau = \Delta\tau_1 - \Delta\tau_2 \quad (33)$$

is the difference between the two delay estimation errors. For a given class and code length ρ' is a parameter [319]. If $\Delta\tau$ is a zero-mean Gaussian variable with variance σ_τ^2 then ε_τ is a zero-mean Gaussian variable with variance $2\sigma_\tau^2$.

The second component of (30) can be represented as

$$\begin{aligned} \cos \hat{\varepsilon} &= \cos(\varepsilon + \Delta\varepsilon) = \cos \varepsilon \cos \Delta\varepsilon - \sin \varepsilon \sin \Delta\varepsilon \\ &= (1 - \Delta\varepsilon^2/2) \cos \varepsilon - \Delta\varepsilon \sin \varepsilon \\ &= (1 + s_\varepsilon) \cos \varepsilon, \end{aligned} \quad (34)$$

where

$$s_\varepsilon = -(\Delta\varepsilon^2/2 + \Delta\varepsilon \cdot \tan \varepsilon). \quad (35)$$

Now, (30) becomes

$$\hat{R} = R + \Delta R, \quad (36)$$

where

$$\begin{aligned} R &= \rho \cos \varepsilon, \\ \Delta R &= \rho \cos \varepsilon (s_\varepsilon + s_\rho + s_\varepsilon s_\rho). \end{aligned} \quad (37)$$

Whenever $k' \neq k$, the average value of the crosscorrelation $\bar{\rho} = 0$. It can be shown by simulation (see Fig. 11) that parameter ΔR can be considered to be an additional noise component having a Gaussian distribution with zero-mean and variance

$$\sigma_{\Delta R}^2 = \rho^2 [(1 + 2\sigma_\rho^2 \sigma_\tau^2 / \rho^2)(3\sigma_\phi^4 + 2\sigma_\phi^2) + 2\sigma_\rho^2 \sigma_\tau^2 / \rho^2], \quad (38)$$

where σ_p^2 is the squared magnitude of the correlation function derivative (slope) at the point of zero-delay error defined in (32). Similar expressions can be derived for the estimations of (27)–(29).

If the delay spread is large it can cause severe ISI and the overall received signal model should be modified accordingly. However, when the delay spread is limited to less than one symbol interval, in asynchronous network the vector (19) can be expressed as [115, 122]

$$\begin{aligned} \mathbf{y}^{(n)}(\mathbf{R}, \mathbf{H}, \mathbf{A}, \mathbf{d}) = & \mathbf{R}^{(n)}(2)\mathbf{H}^{(n-2)}\mathbf{A}\mathbf{d}^{(n-2)} + \mathbf{R}^{(n)}(1)\mathbf{H}^{(n-1)}\mathbf{A}\mathbf{d}^{(n-1)} \\ & + \mathbf{R}^{(n)}(0)\mathbf{H}^{(n)}\mathbf{A}\mathbf{d}^{(n)} + \mathbf{R}^{(n)}(-1)\mathbf{H}^{(n+1)}\mathbf{A}\mathbf{d}^{(n+1)} \\ & + \mathbf{R}^{(n)}(-2)\mathbf{H}^{(n+2)}\mathbf{A}\mathbf{d}^{(n+2)} + \mathbf{n}^{(n)}, \end{aligned} \quad (39)$$

where

$$\mathbf{A} = \text{diag}(A_1, A_2, \dots, A_K) \in \mathbb{R}^{K \times K} \quad (40)$$

is a diagonal matrix of transmitted amplitudes,

$$\mathbf{H}^{(n)} = \text{diag}(\mathbf{H}_1^{(n)}, \mathbf{H}_2^{(n)}, \dots, \mathbf{H}_K^{(n)}) \in \mathbb{C}^{KLM \times K} \quad (41)$$

is the matrix of channel coefficient vectors

$$\mathbf{H}_k^{(n)} = \left(H_{k,11}^{(n)}, H_{k,12}^{(n)}, \dots, H_{k,1M}^{(n)}, H_{k,21}^{(n)}, \dots, H_{k,LM}^{(n)} \right)^T \in \mathbb{C}^{LM} \quad (42)$$

and

$$\mathbf{d}^{(n)} = \left(d_1^{(n)}, d_2^{(n)}, \dots, d_K^{(n)} \right)^T \in \mathbb{R}^K \quad (43)$$

is the vector of the transmitted data and $\mathbf{n}^{(n)} \in \mathbb{C}^{KLM}$ is the output vector due to noise. This component is due to processing the second term of (11) that was dropped for simplicity in the derivation of (12)–(38). It is easy to show that $\mathbf{R}^{(n)}(i) = \mathbf{0}_{KLM}, \forall |i| > 2$ and $\mathbf{R}^{(n)}(-i) = \mathbf{R}^{T(n+1)}(i)$, where $\mathbf{0}_{KLM}$ is an all-zero matrix of size $KLM \times KLM$. Thus, the concatenation vector of the matched filter outputs (20) has the expression

$$\mathbf{y}(\mathbf{R}, \mathbf{H}, \mathbf{A}, \mathbf{d}) = \mathbf{R}\mathbf{H}\mathbf{A}\mathbf{d} + \mathbf{n} = \mathbf{R}\mathbf{H}\mathbf{h} + \mathbf{n}, \quad (44)$$

where

$$\mathbf{R} = \begin{pmatrix} \mathbf{R}^{(0)}(0) & \mathbf{R}^{T(1)}(1) & \mathbf{R}^{T(2)}(2) & \cdots & \mathbf{0}_{KLM} \\ \mathbf{R}^{(1)}(1) & \mathbf{R}^{(1)}(0) & \mathbf{R}^{T(2)}(1) & \cdots & \mathbf{0}_{KLM} \\ \mathbf{R}^{(2)}(2) & \mathbf{R}^{(2)}(1) & \mathbf{R}^{(2)}(0) & \cdots & \mathbf{0}_{KLM} \\ \vdots & \vdots & \vdots & \ddots & \vdots \\ \mathbf{0}_{KLM} & \mathbf{0}_{KLM} & \mathbf{0}_{KLM} & \cdots & \mathbf{R}^{(N_b-1)}(0) \end{pmatrix} \in \mathbb{R}^{N_b KLM \times N_b KLM}, \quad (45)$$

$$\mathbf{H} = \text{diag}(\mathbf{H}^{(0)}, \mathbf{H}^{(1)}, \dots, \mathbf{H}^{(N_b-1)}) \in \mathbb{C}^{N_b KLM \times N_b K}, \quad (46)$$

$$\mathbf{A} = \text{diag}(\mathbf{A}, \mathbf{A}, \dots, \mathbf{A}) \in \mathbb{R}^{N_b K \times N_b K}, \quad (47)$$

$$\mathbf{d} = (\mathbf{d}^{T(0)}, \mathbf{d}^{T(1)}, \dots, \mathbf{d}^{T(N_b-1)})^T \in \mathbb{R}^{N_b K}, \quad (48)$$

$\mathbf{h} = \mathbf{A}\mathbf{d}$ is the data-amplitude product vector, and \mathbf{n} is the Gaussian noise output vector with zero-mean and covariance matrix $\sigma^2 \mathbf{R}$. If we define

$$\mathbf{y}_{ii} = \mathbf{y}(\mathbf{R}^{ii}, \mathbf{H}, \mathbf{A}, \mathbf{d}_i), \quad (49)$$

$$\mathbf{y}_{qi} = \mathbf{y}(\mathbf{R}^{qi}, \mathbf{H}, \mathbf{A}, \mathbf{d}_q), \quad (50)$$

$$\mathbf{y}_{iq} = \mathbf{y}(\mathbf{R}^{iq}, \mathbf{H}, \mathbf{A}, \mathbf{d}_i), \quad (51)$$

$$\mathbf{y}_{qq} = \mathbf{y}(\mathbf{R}^{qq}, \mathbf{H}, \mathbf{A}, \mathbf{d}_q), \quad (52)$$

then we have

$$\mathbf{y}_i = \mathbf{y}_{ii} + \mathbf{y}_{qi}, \quad (53)$$

$$\mathbf{y}_q = \mathbf{y}_{iq} + \mathbf{y}_{qq}. \quad (54)$$

Based on these equations a complex decorrelator receiver structure is derived in the Appendix.

3.2 Space-time multipath intensity profile

The exponential multipath intensity profile (MIP) channel model is a widely used analytical model and is realized as a tapped delay line [320]. It can flexibly model different realistic propagation scenarios. The decay of the profile and the number of taps can be varied. In [321], it is shown that the exponential decay model is valid also for the

spatial autocorrelation of the azimuth and delay spread. Therefore, the averaged power coefficients in the space-time multipath intensity profile can be presented as

$$\overline{\alpha_{lm}} = \overline{\alpha_{00}} e^{-\lambda_l l} e^{-\lambda_m m} \quad l, m, \lambda_l, \lambda_m \geq 0, \quad (55)$$

where λ_l is the temporal (delay) decay parameter, λ_m is the spatial decay parameter of the profile, l is the multipath delay index, and m is the spatial diversity index. The spatial decay parameter enables modeling of full or reduced (e.g., correlated antennas) diversity gains. Power coefficients in the model can be normalized as

$$\sum_{l=0}^{L-1} \sum_{m=0}^{M-1} \overline{\alpha_{00}} e^{-(\lambda_l l + \lambda_m m)} = 1. \quad (56)$$

For $\lambda_l = 0$ there would be equal gain in every multipath component, whereas very large λ_l would result in essentially 1-path channel in delay dimension. The number of resolvable multipaths depends on the chip rate and the channel delay spread.

4 Wideband CDMA performance analysis

This chapter discusses effective user capacity assessment of wideband CDMA systems, including various practical imperfections. The general framework for performance analysis is defined in Section 4.1. Section 4.2 is devoted to space-time rake combining issues. Section 4.3 shows numerical examples for the conventional rake receiver. A linear decorrelating multiuser detector is utilized in Section 4.4. Nonlinear interference cancellation is investigated in Section 4.5. Finally, Section 4.6 shows capacity comparison for these three alternative receiver structures.

The major body of the content of this chapter can also be found in the original publications [1, 2, 4, 5].

4.1 CDMA system capacity

The starting point in the evaluation of CDMA system capacity is the received signal energy per symbol divided with the overall noise density in a given reference receiver with index k . In the general case this quantity can be represented as

$$Y_{bk} = \frac{E_{bk}}{N_0} = \frac{ST}{I_{oc} + I_{oic} + I_{oin} + \eta_{th}}, \quad (57)$$

where I_{oc} , I_{oic} , and I_{oin} are power densities of intracell, intercell and overlay type internetwork interference, respectively, and η_{th} is thermal noise power density. Parameter S is the overall received power of the useful signal and $T = 1/R_b$ is the information bit interval (R_b is the bit rate). Contributions of I_{oic} and I_{oin} to N_0 have been discussed in a number of papers, e.g., [58]. In order to minimize repetition in the analysis we will parameterize this contribution by introducing a joint Gaussian variable

$$\eta_0 = I_{oic} + I_{oin} + \eta_{th}. \quad (58)$$

In this framework, closer attention is paid to the intracell interference I_{oc} in the analysis of a wireless CDMA network which is based on an imperfect rake receiver that may be enhanced by a linear decorrelator or nonlinear iterative interference canceller for MAI mitigation. An extension of the analysis to include more detailed intercell and internetwork interference models is straightforward. A general block diagram of the receiver is shown in Fig. 1, where the block ‘Multiuser receiver’ refers to the decorrelator or nonlinear interference canceller. This block is marked with the dashed line because it is optional. Without MUD unit the receiver is suppressed to the conventional rake receiver structure that is used as a reference in the capacity evaluation.

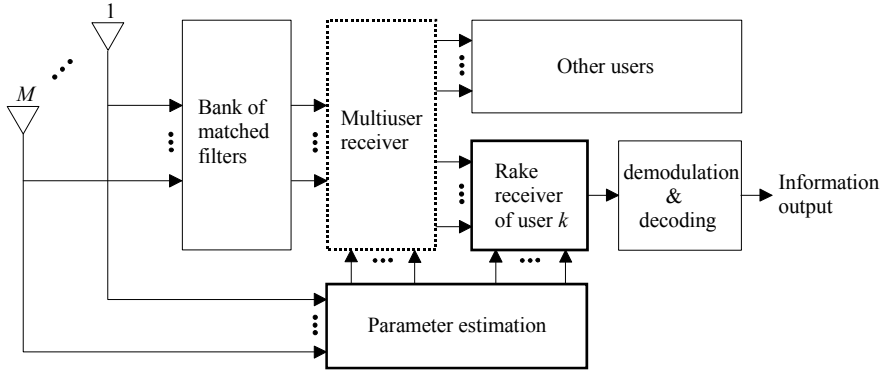


Fig. 1. General receiver block diagram.

The analysis will begin with the rejection combiner that chooses the first multipath signal component in the first antenna of the k th user and rejects (suppresses) the other signal components. In this case, (57) for the I-channel becomes

$$\begin{aligned}
 Y_{ibk} &= \frac{\alpha_{iik11}(k11)S/R_b}{\left\{ \alpha_{iqk11}(k11) + \sum_{k'=1}^K \sum_{\substack{l'=1 \\ l'=2(k'=k)}}^L \sum_{m'=1}^M \alpha_{ik1}(k'l'm') \right\} S/R_b + \eta_0} \\
 &= \frac{\alpha_{iim1}(m1)}{\alpha_{iqk11}(k11) + \sum_{k'=1}^K \sum_{\substack{l'=1 \\ l'=2(k'=k)}}^L \sum_{m'=1}^M \alpha_{ik1}(k'l'm') + \eta_0 R_b / S},
 \end{aligned} \tag{59}$$

where $\alpha_x(z)$, (for $x = iik11, iqk11, ik1$ and $z = k11, k'l'm'$) is the power coefficient, defined as $\alpha_x(z) = E_\varepsilon[|y_x(z)|^2] / S$, S is the normalized power level of the received signal and parameters $y_x(z)$ are in general defined by (12) and (53). Expression $E_\varepsilon[\cdot]$ stands for expectation, i.e., averaging with respect to corresponding phases $\varepsilon_{a,b}$ defined by (12)–(15). Based on this, we have

$$\alpha_{ik1}(k'l'm') = E_{\varepsilon}[y_{ik1}^2(k'l'm')] = A_{k'l'm'}^2 \rho_{ik1}^2(k'l'm') / 2 \Rightarrow A_{k'l'm'}^2 / 2, \quad (60)$$

where $\rho_{ik1}^2(k'l'm') = \rho_{ik'l'm',ik1}^2 + \rho_{qk'l'm',ik1}^2$, $\rho^2 = E_{\rho}[\rho_{ik'l'm',ik1}^2 + \rho_{qk'l'm',ik1}^2]$ and after normalization $A_{k'l'm'}^2 \rho^2 / 2 \Rightarrow A_{k'l'm'}^2 / 2$.

A similar equation can be obtained for the Q-channel. It has been assumed that all 'interference per path' components are independent. In the following, the notation is simplified by dropping all indices $ik1$ leading to $\alpha_{ik1}(k'l'm') \Rightarrow \alpha_{klm}$. With *no power control* (npc) α_{klm} will depend only on the channel characteristics. In *partial power control* (ppc) only the first multipath component of the signal is measured and used in the power control (open or closed) loop. *Full power control* (fpc) will normalize all components of the received signal and *rake power control* (rpc) will normalize only those components combined in the rake receiver. The rpc seems to be more feasible because these components are already available. These concepts for ideal operation are defined by the following equations

$$npc \Rightarrow \alpha_{klm} = \alpha_{klm}, \quad \forall k, l, m, \quad (61)$$

$$ppc \Rightarrow \alpha_{k11} = 1, \quad \forall k, \quad (62)$$

$$fpc \Rightarrow \sum_{l=1}^L \sum_{m=1}^M \alpha_{klm} = 1, \quad \forall k, \quad (63)$$

$$rpc \Rightarrow \sum_{r=1}^{L_0} \alpha_{klm} = 1, \quad \forall k, \quad (64)$$

where L_0 is the number of rake fingers in the receiver. The contemporary theory in this field does not recognize these options, which causes a lot of misunderstanding and misconceptions in the interpretation of the power control problem in the CDMA network. Although fpc is not practically feasible, the analysis including fpc should provide the reference results for the comparison with other, less efficient options.

Another problem in the interpretation of the results in the analysis of the power control imperfections is caused by the assumption that all users in the network have the same problem with power control. Hence, the imperfect power control is characterized by the same variance of the power control error. This is more than a pessimistic assumption and yet it has been used very often in analyses published so far. If we now introduce matrix $\mathbf{\alpha}_k$ with coefficients $\|\alpha_{klm}\|, \forall k, l, m$, except for $\alpha_{k11} = 0$, and use notation $\mathbf{1}$ for the vector of all ones, (59) becomes

$$Y_{bk} = \frac{\alpha_{k11}}{\mathbf{1} \cdot \mathbf{\alpha}_k \cdot \mathbf{1}^T + \eta_0 R_b / S}. \quad (65)$$

Compared with (59), the index i is dropped, indicating that the same form of equation is valid for both the I- and Q-channels defined by (53) and (54).

4.2 Space-time rake combining in the multipath channel

If an L_0 -finger space-time (or 2-D) rake receiver ($L_0 \leq LM$) with combiner coefficients w_{kr} ($r = 1, 2, \dots, L_0$) and an imperfect decorrelator is used, the signal-to-noise ratio for the k th user will become

$$Y_{bk} = \frac{r_k^{(L_0)} S T_b}{\varsigma_0 \eta} = \frac{r_k^{(L_0)}}{\varsigma_0 \eta R_b / S}, \quad (66)$$

where

$$\varsigma_0 = \sum_{r=1}^{L_0} w_{kr}^2 = \mathbf{w}_k \mathbf{w}_k^T, \quad \mathbf{w}_k = (w_{k1}, w_{k2}, \dots, w_{kL_0}) \quad (67)$$

is due to Gaussian noise processing in the rake receiver, and the noise density η_0 , after decorrelation, becomes η . The relation between these two parameters is elaborated later in (86)–(89). The parameter $r_k^{(L_0)}$ in (66) is called the rake receiver efficiency and is given by

$$r_k^{(L_0)} = \left(\sum_{r=1}^{L_0} w_{kr} \cos \varepsilon_{\theta kr} \sqrt{\alpha_{kr}} \right)^2 = (\mathbf{w}_k \mathbf{A}_k)^2 \quad (68)$$

with $\mathbf{A}_k = (\cos \varepsilon_{\theta k1} \sqrt{\alpha_{k1}}, \cos \varepsilon_{\theta k2} \sqrt{\alpha_{k2}}, \dots, \cos \varepsilon_{\theta kL_0} \sqrt{\alpha_{kL_0}})^T$. Parameter $\varepsilon_{\theta kr} = \theta_{kr} - \hat{\theta}_{kr}$ is the carrier phase synchronization error of user k at the receiver branch r . Indices in the subscript are dropped whenever it does not cause any confusion. In the sequel, the following notation will be used: $\alpha_{kr} = A_{kr}^2 / 2$, \hat{A}_{kr} is the estimate of A_{kr} , $\varepsilon_a = \Delta A_{kr} / A_{kr} = (A_{kr} - \hat{A}_{kr}) / A_{kr}$ is the relative amplitude estimation error, and ε_θ is the carrier phase estimation error.

4.2.1 Equal gain combining

For the equal gain combiner (EGC) the combiner coefficients are given as $w_{kr} = 1$. Having in mind the notation used so far, index k will be omitted for simplicity. By using the notation $A_r / A_1 = \sqrt{\alpha_r / \alpha_1}$, averaging (68) gives for EGC

$$\begin{aligned}
\mathbb{E}\{r^{(L_0)}\} &= \mathbb{E}\left\{\left(\sum_{r=1}^{L_0} \cos \varepsilon_{\theta_r} \sqrt{\alpha_r}\right)^2\right\} \cong \mathbb{E}\left\{\left(\sum_{r=1}^{L_0} (1 - \varepsilon_{\theta_r}^2 / 2) \sqrt{\alpha_r}\right)^2\right\} \\
&= \sum_{r=1}^{L_0} \sum_{\substack{l=1 \\ l \neq r}}^{L_0} (1 - \sigma_{\theta_r}^2)(1 - \sigma_{\theta_l}^2) \sqrt{\alpha_r \alpha_l} + \sum_{r=1}^{L_0} \alpha_r (1 - 2\sigma_{\theta_r}^2 + 3\sigma_{\theta_r}^4).
\end{aligned} \tag{69}$$

4.2.2 Maximal ratio combining

For the maximal ratio combiner (MRC) the combiner coefficients are based on estimates as

$$\hat{w}_r = \frac{\cos \varepsilon_{\theta_r}}{\cos \varepsilon_{\theta_1}} \cdot \frac{\hat{A}_r}{\hat{A}_1} \cong \frac{(1 - \varepsilon_{\theta_r}^2 / 2)}{(1 - \varepsilon_{\theta_1}^2 / 2)} \cdot \frac{A_r (1 - \varepsilon_{ar})}{A_1 (1 - \varepsilon_{a1})}, \tag{70}$$

$$\mathbb{E}\{\hat{w}_r\} = w_r (1 - \sigma_{\theta_r}^2)(1 + \sigma_{\theta_1}^2)(1 - \varepsilon_{ar})(1 + \varepsilon_{a1}), \tag{71}$$

$$\mathbb{E}\{\hat{w}_r^2\} = w_r^2 (1 - 2\sigma_{\theta_r}^2 + 3\sigma_{\theta_r}^4)(1 + 2\sigma_{\theta_1}^2 - 3\sigma_{\theta_1}^4)(1 - \varepsilon_{ar})^2 (1 + \varepsilon_{a1})^2. \tag{72}$$

For MRC the average rake efficiency becomes

$$\begin{aligned}
\mathbb{E}\{r^{(L_0)}\} &= \mathbb{E}\left\{\left(\sum_{r=1}^{L_0} \hat{w}_r \cos \varepsilon_{\theta_r} \sqrt{\alpha_r}\right)^2\right\} \cong \mathbb{E}\left\{\left(\sum_{r=1}^{L_0} \frac{\alpha_r}{\sqrt{\alpha_1}} \frac{(1 - \varepsilon_{\theta_r}^2 / 2)^2 (1 - \varepsilon_{ar})}{(1 - \varepsilon_{\theta_1}^2 / 2) (1 - \varepsilon_{a1})}\right)^2\right\} \\
&= \sum_{r=1}^{L_0} \frac{\alpha_r^2}{\alpha_1} (1 - 2\sigma_{\theta_1}^2 + 3\sigma_{\theta_1}^4) \frac{(1 - \varepsilon_{ar})^2}{(1 - \varepsilon_{a1})^2} \\
&\quad + \sum_{r=1}^{L_0} \sum_{\substack{l=1 \\ l \neq r}}^{L_0} \frac{\alpha_r \alpha_l}{\alpha_1} (1 - 2\sigma_{\theta_r}^2 + 3\sigma_{\theta_r}^4)(1 - 2\sigma_{\theta_l}^2 + 3\sigma_{\theta_l}^4) \times \\
&\quad \times (1 + 2\sigma_{\theta_1}^2 - 3\sigma_{\theta_1}^4)(1 - \varepsilon_{ar})(1 - \varepsilon_{al})(1 + \varepsilon_{a1})^2.
\end{aligned} \tag{73}$$

One should note that although $\hat{w}_1 = 1$, the value of the first term in the above sum is $\cos \varepsilon_{\theta_1} \sqrt{\alpha_1}$, which takes into account the error in the estimation of the phase for the first finger. In order to avoid dealing with the fourth power terms of the type $(1 - \varepsilon_{\theta_r}^2 / 2)^4$ in the evaluation of the first term in (73), limits will be used. The upper limit follows from the substitution

$$\varepsilon_{\theta_r}^2 \Rightarrow \varepsilon_{\theta_1}^2. \tag{74}$$

Using (74) leads to a further simplification

$$\frac{(1 - \varepsilon_{\theta_r}^2 / 2)^4}{(1 - \varepsilon_{\theta_1}^2 / 2)^2} \Rightarrow (1 - \varepsilon_{\theta_1}^2 / 2)^2 \quad (75)$$

and the first term of (73) becomes [322]

$$\sum_{r=1}^{L_0} \frac{\alpha_r^2}{\alpha_1} (1 - 2\sigma_{\theta_1}^2 + 3\sigma_{\theta_1}^4) \frac{(1 - \varepsilon_{ar})^2}{(1 - \varepsilon_{a1})^2}. \quad (76)$$

For the lower limit, the substitution

$$\varepsilon_{\theta_1}^2 \Rightarrow \varepsilon_{\theta_r}^2 \quad (77)$$

is used and the first term of (73) becomes

$$\sum_{r=1}^{L_0} \frac{\alpha_r^2}{\alpha_1} (1 - 2\sigma_{\theta_r}^2 + 3\sigma_{\theta_r}^4) \frac{(1 - \varepsilon_{ar})^2}{(1 - \varepsilon_{a1})^2}. \quad (78)$$

For a complex signal, the parameter $\cos \varepsilon_{\theta_r}$ should be replaced by

$$\cos \varepsilon_{\theta_r} \Rightarrow \cos \varepsilon_{\theta_r} + b\rho \sin \varepsilon_{\theta_r}, \quad (79)$$

where b is the information in the interfering channel (I or Q), and ρ is the crosscorrelation between the codes used in the I- and Q-channels. For small tracking errors this term can be approximated as

$$\cos \varepsilon_{\theta_r} + b\rho \sin \varepsilon_{\theta_r} \approx 1 + b\rho \varepsilon - \varepsilon^2 / 2, \quad (80)$$

where the notation is further simplified by dropping the subscript θ_r . By using (80) in (70)–(78), similar expressions can be derived for the complex signal format.

4.2.3 Channel parameter estimation errors

From the prior imperfect rake derivations we can see that expressions for the carrier phase estimation errors, and in the MRC case also for the amplitude estimation error, are needed for the further numerical evaluation on the impact of these imperfections to the effective CDMA user capacity. A performance measure of any estimator is the parameter estimation error variance that should be directly used in equation (84) for equivalent noise variance and (69)–(80) for the rake combiner. If joint parameter estimation is used, based on maximum-likelihood (ML) criterion, then the Cramér–Rao lower bound could

be used for these purposes [323–327]. For Kalman filter estimators [323, 328] the error covariance matrix is available for each iteration of estimation. This work, however, is restricted to the independent estimation of channel parameters. Simple phase-locked and delay-locked loop estimators are assumed, where the error variance is inversely proportional to the estimator loop signal-to-noise ratio. For carrier phase and code delay estimation error a simple relation $\sigma_{\hat{0},\tau}^2 = 1/SNR_L$ is adopted where SNR_L is the signal-to-noise ratio in the tracking loop. For SNR_L , the noise power is, in general, given as $N = B_L N_0$. In this case, the noise density N_0 is approximated as a ratio of the overall interference plus noise power divided by the signal bandwidth. The loop bandwidth B_L is proportional to the maximum Doppler shift f_D that depends on the velocity and defines the severity of fading. In addition to this

$$\varepsilon_a = \frac{A - \hat{A}(1 - \varepsilon_\tau)}{A} = \frac{\Delta A + \hat{A}\varepsilon_\tau}{A} = \varepsilon_A + \varepsilon_\tau(1 - \varepsilon_A), \quad (81)$$

where ε_τ is the spreading code delay estimation error and $\varepsilon_A = (A - \hat{A})/A = 1 - \hat{A}/A$ is the relative amplitude estimation error. E.g., for noncoherent estimation, there is an expression [332]

$$\frac{\hat{A}}{A} = \sqrt{\frac{\pi}{4y}} \exp\left(-\frac{y}{2}\right) \left\{ 1 + yI_0\left(\frac{y}{2}\right) + yI_1\left(\frac{y}{2}\right) \right\}, \quad (82)$$

where $I_0(\cdot)$ and $I_1(\cdot)$ are the zeroth and first order modified Bessel functions, respectively, and y is the signal-to-noise ratio.

4.3 Imperfect rake receiver

As a well-established benchmark for capacity evaluation, a conventional rake receiver [329] is employed. It is based on matched filtering at each diversity branch. Branch weighting is based either on equal gain or maximal ratio combining, as described in the previous section.

4.3.1 User capacity and sensitivity

For a conventional single-user rake receiver, (57) can be rewritten into form

$$y_k = \frac{r_k^{(L_0)} G}{f(\mathbf{a}) K_{MF} + \sigma_n^2} \quad (83)$$

where $r_k^{(L_0)}$ refers to the rake efficiency of the desired user (i.e., received energy by the rake, index L_0 is the number of rake fingers), G is the processing gain, K_{MF} is the

average number of active users that can be served at the predefined SNR target Y_0 , $f(\mathbf{a}) = \mathbb{E}[I_{oc}] = w_{kr}^2 L_0 LM \alpha$ is the intracell interference (MAI) density, w_{kr} is the rake combiner coefficient and $\alpha = 1/(LM)$ is the average power of the multipath components.

The maximum number of simultaneous active users, i.e., user capacity at $y_k = Y_0$, can be solved from (83) to be

$$K_{MF} = \left\lfloor \frac{r_k^{(L_0)} G - Y_0 \sigma_n^2}{Y_0 f(\mathbf{a})} \right\rfloor \quad (84)$$

where $\lfloor \cdot \rfloor$ refers to the floor function rounding K_{MF} downwards to the largest integer. The maximum capacity K_{MF}^{\max} is achieved from (84) in the absence of estimation errors, i.e., while the maximum Doppler frequency and estimation error variances are zero. Then the sensitivity function that represents the relative user capacity lost due to imperfections can be expressed as

$$\mathfrak{R}_{MF} = \frac{K_{MF}^{\max} - K_{MF}}{K_{MF}^{\max}}. \quad (85)$$

4.3.2 Numerical examples

Table 1 summarizes the most relevant parameters assumed in the upcoming numerical capacity and sensitivity results. The chosen processing gain corresponds to the WCDMA concept [111] chip rate 3.84 Mcps at the coded data rate of 15 kbps. For MRC, the upper limit derived in Section 4.2.2 is adopted. It should be noted that the upper and lower limits turned out to be so tight that only at the largest normalized Doppler frequencies, minor visible differences in capacity appear. Therefore, the upper MRC limit is used exclusively in the upcoming numerical examples.

Table 1. Key parameters for the numerical illustrations.

Processing gain G	256 (24 dB)
Required signal-to-noise ratio Y_0	3.98 (6 dB)
Data modulation	BPSK
Number of multipaths L	4
Number of receive antennas M	2
Temporal MIP decay parameter λ_l	0.5, 0.75
Spatial MIP decay parameter λ_m	0.5, 0.75
Normalized max. Doppler shift $f_D T$	$[0, 0.25, 0.5, 0.75, 1, 1.25, 1.5, 1.75, 2] \times 10^{-2}$
Number of utilized diversity branches L_0	1, 2, 3, 4, 5, 6, 7, 8
Phase and code delay error variance $\sigma_{\theta, \tau}^2$	$1/SNR_L$
Amplitude estimation error (MRC) ε_a	According to (81) and (82)

Table 2 shows the relative channel tap gains of the examined space-time multipath intensity profiles² (normalized with respect to the first branch) in dB scale.

Table 2. Multipath intensity profiles considered in the numerical examples.

$\lambda_l = \lambda_m$	$\overline{\alpha_{00}}$ [dB]	$\overline{\alpha_{01}}, \overline{\alpha_{10}}$ [dB]	$\overline{\alpha_{11}}, \overline{\alpha_{20}}$ [dB]	$\overline{\alpha_{21}}, \overline{\alpha_{30}}$ [dB]	$\overline{\alpha_{31}}$ [dB]
0.5	0	-2.17	-4.34	-6.51	-8.69
0.75	0	-3.26	-6.51	-9.77	-13.03

Fig. 2 shows user capacity surface as a function of diversity order and fading rate in the case of equal gain rake combiner with the multipath intensity profile parameters $\lambda_l = \lambda_m = 0.5$. It is clearly seen that without impairments the number of supported users/cell increases gradually with the diversity order. However, at large normalized Doppler spreads the capacity flats out or even degrades at high diversity orders. Fig. 3 illustrates the same setup for maximal ratio rake combiner. Now the achievable user capacities are slightly higher than in the case of EGC. Even with the imperfections the capacity steadily increases with the number of combined diversity branches.

With more impulsive (i.e., less diversity gain) MIP with $\lambda_l = \lambda_m = 0.75$, the capacities diminish as expected. This is demonstrated in Fig. 4 (EGC) and in Fig. 5 (MRC). In this scenario, the EGC performs poorly at full diversity ($L_0 = 8$) while the imperfections are maximal ($f_D T = 0.02$).

Capacity sensitivity to impairments is plotted in Fig. 6 for EGC, $\lambda_l = \lambda_m = 0.5$. Sensitivity increases with the fading rate. Over 40% of the maximum capacity is lost at $L_0 = 8$ and $f_D T = 0.02$. For MRC in Fig. 7, the sensitivity surface is quite similar, except somewhat lower absolute values. Fig. 8 shows the sensitivity with EGC, $\lambda_l = \lambda_m = 0.75$ and Fig. 9 with MRC, respectively. Of these cases, the highest sensitivity function value is recorded in Fig. 8 where it nears 60%. This means that 60% of the capacity is lost due to imperfections. Sensitivity can be reduced with better estimators at the cost of higher complexity and energy consumption. Careful optimization and tradeoff analysis with respect to these topics is required. Adaptive implementation techniques can be applied to deal with these important issues.

² These channel profiles have been chosen as appropriate representatives of different, yet realistic propagation channels.

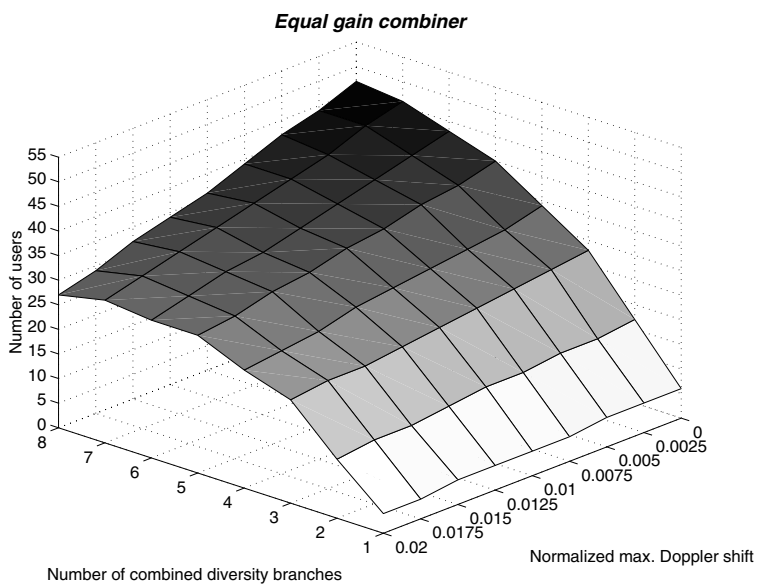


Fig. 2. User capacities with the rake receiver (EGC, $\lambda_l = \lambda_m = 0.5$).

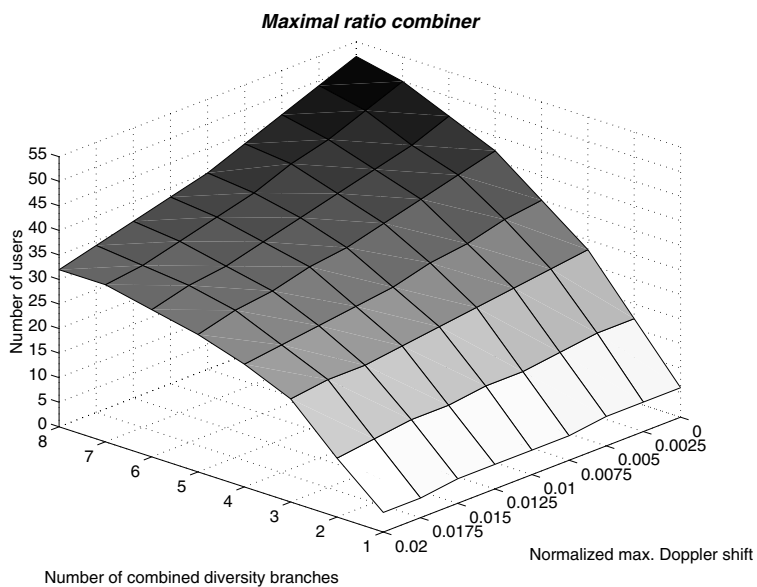


Fig. 3. User capacities with the rake receiver (MRC, $\lambda_l = \lambda_m = 0.5$).

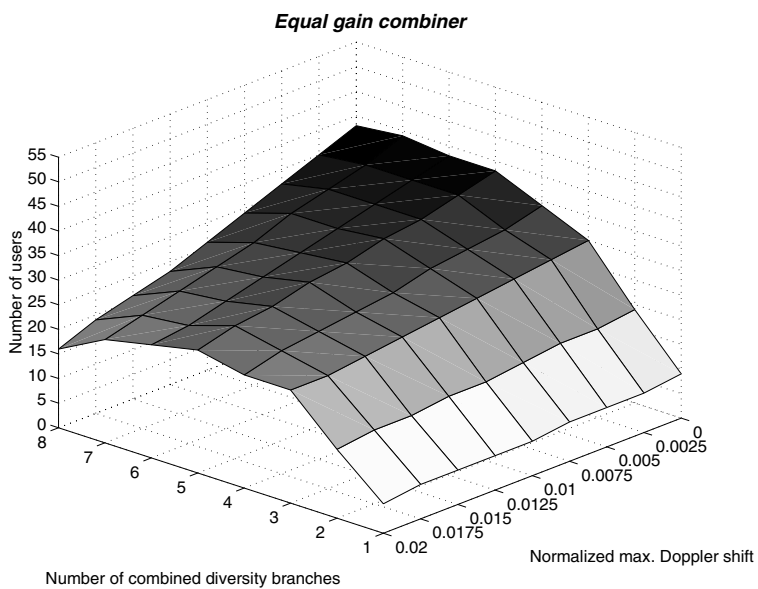


Fig. 4. User capacities with the rake receiver (EGC, $\lambda_l = \lambda_m = 0.75$).

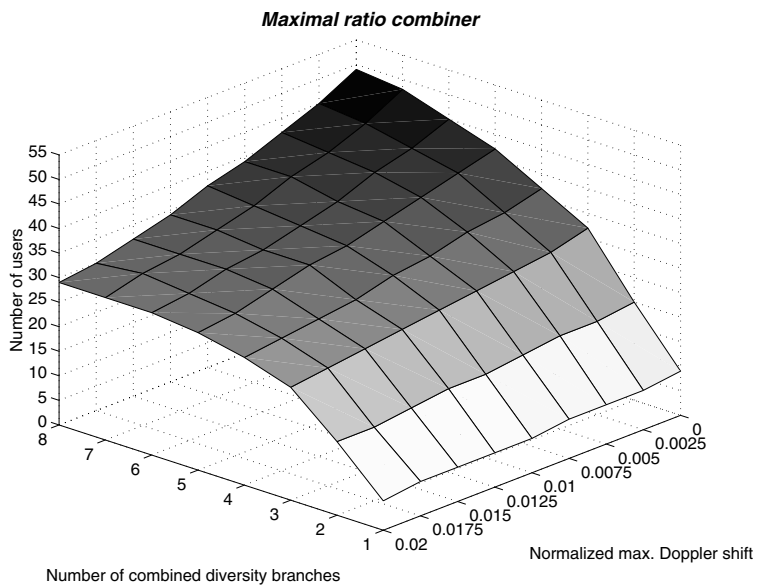


Fig. 5. User capacities with the rake receiver (MRC, $\lambda_l = \lambda_m = 0.75$).

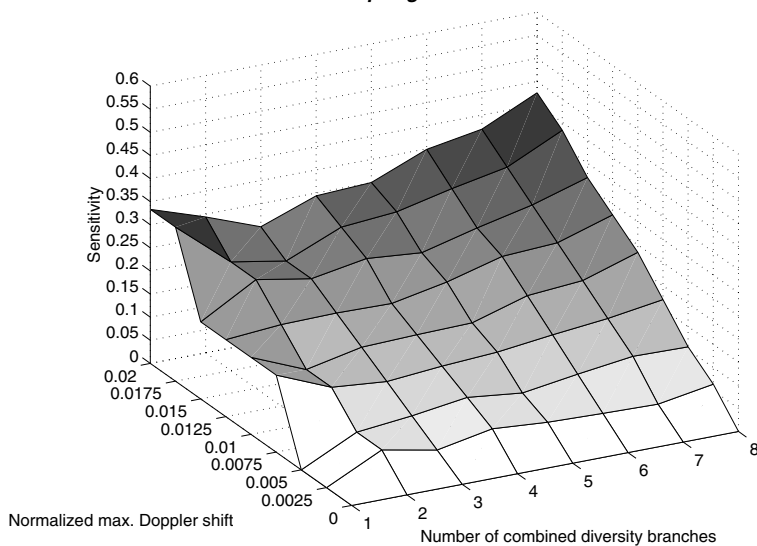
Equal gain combiner

Fig. 6. Sensitivity of the rake receiver (EGC, $\lambda_l = \lambda_m = 0.5$).

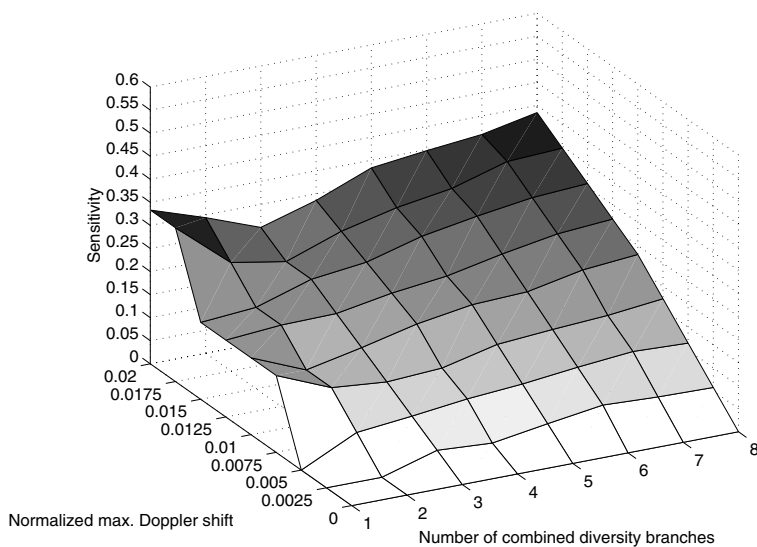
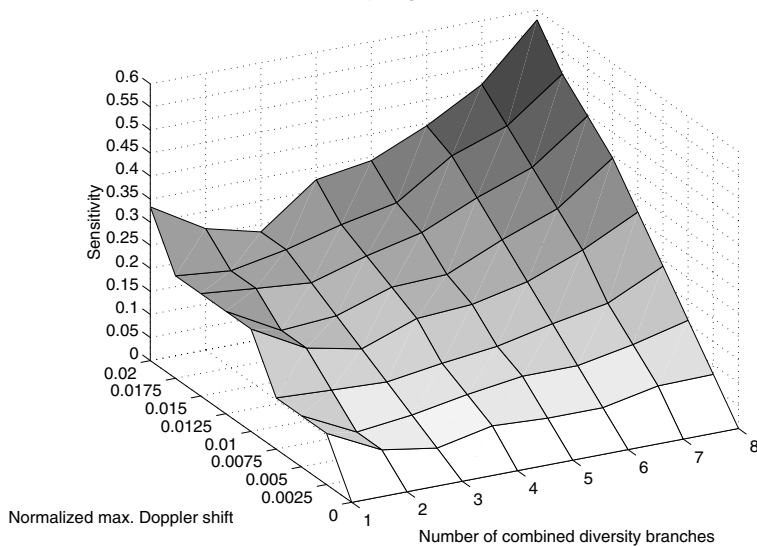
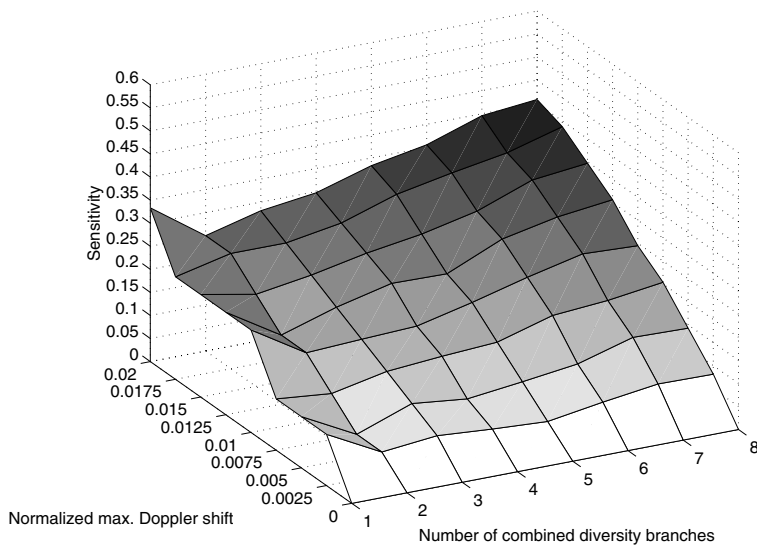
Maximal ratio combiner

Fig. 7. Sensitivity of the rake receiver (MRC, $\lambda_l = \lambda_m = 0.5$).

Equal gain combiner**Fig. 8. Sensitivity of the rake receiver (EGC, $\lambda_l = \lambda_m = 0.75$).****Maximal ratio combiner****Fig. 9. Sensitivity of the rake receiver (MRC, $\lambda_l = \lambda_m = 0.75$).**

4.4 Imperfect linear multiuser detector (decorrelator)

In this section, a linear decorrelator is used for interference cancellation in the system. The detector will operate with the inverse of the estimated correlation matrix $\hat{\mathbf{R}}^{-1}$ where the observed correlation matrix of the system can be divided into the perfect estimate and difference (or error) components, i.e., $\mathbf{R} = \hat{\mathbf{R}} + \Delta\mathbf{R}$. It is assumed that the elements of $\Delta\mathbf{R}$ are Gaussian distributed with zero-mean and variance given by (38). This assumption is validated in the numerical examples.

So, after decorrelation by using $\hat{\mathbf{R}}^{-1}$ the residual noise in the receiver will have variance

$$\text{var}\{\hat{\mathbf{R}}^{-1}(\mathbf{n}_r + \mathbf{n})\}, \quad (86)$$

where Gaussian noise components of vector \mathbf{n} have variance σ_n^2 . Gaussian approximated residual noise vector \mathbf{n}_r has variance σ_r^2 that can be approximated as

$$\sigma_r^2 = \sum_{k,l,m} \alpha_{k,l,m} \sigma_{\Delta_{k,l,m}}^2. \quad (87)$$

The average value of this variance can be represented as

$$\overline{\sigma_r^2} \cong \alpha KLM \sigma_{\Delta R}^2, \quad (88)$$

where $\sigma_{\Delta R}^2$ is given by (38). After the rake combiner, the overall noise variance becomes

$$\sigma^2 \cong \zeta_0 R_{kk}^+ (\sigma_r^2 + \sigma_n^2) = \Sigma_r^2 + \Sigma_n^2, \quad (89)$$

where R_{kk}^+ is the kk th component of $\hat{\mathbf{R}}^{-1}$. In (89), Σ_r^2 is contribution of system imperfections due to the overall noise variance σ^2 and Σ_n^2 is contribution of Gaussian noise after decorrelation (noise enhancement). So, the equivalent noise variance is expressed in terms of phase and code delay estimation errors (see (38)).

If decorrelation is performed prior to parameter estimation, N_0 is obtained from the equivalent noise having the variance defined by (89). If parameter estimation is used without decorrelation, then the overall noise consists of MAI and Gaussian noise.

4.4.1 User capacity and sensitivity

Formulation of effective user capacity will be started with the average signal-to-noise ratio that can be expressed as

$$\bar{Y}_b = \frac{Sr^{(L_0)}G}{\sigma^2} = \frac{Sr^{(L_0)}(K)G}{\sigma^2(K)} = \bar{Y}_b(K) \quad (90)$$

where the rake efficiency $r^{(L_0)}$ was given in Section 4.2, σ^2 is given by (89) and G is the processing gain. Rake receiver efficiency and overall noise variance depend on the number of active users K in the desired cell. Assuming that a certain quality of transmission is accepted, i.e., bit error probability/rate $P_e = 10^{-e}$. This performance can be achieved with given signal-to-noise ratio $Y_0 = \bar{Y}_b(K = K_{DEC})$, where K_{DEC} is the user capacity. Then, in the case of the perfect channel estimation, the maximum user capacity per cell (reference) is obtained as

$$K_{DEC}^{\max} = \left[\underset{K}{\text{solution}} \left\{ Y_0 = \frac{Sr^{(L_0)}(K)G}{\Sigma_n^2(K)} \right\} \right]. \quad (91)$$

Similarly, in the case of the imperfect channel estimation the effective user capacity becomes

$$K_{DEC} = \left[\underset{K}{\text{solution}} \left\{ Y_0 = \frac{Sr^{(L_0)}(K)G}{\Sigma_r^2(K) + \Sigma_n^2(K)} \right\} \right]. \quad (92)$$

Based on (91) and (92) the system sensitivity function can now be defined as

$$\mathfrak{R}_{DEC} = \frac{K_{DEC}^{\max} - K_{DEC}}{K_{DEC}^{\max}}. \quad (93)$$

4.4.2 Numerical examples

This section presents some practical numerical examples to illustrate user capacity and sensitivity functions for the decorrelator, based on the definitions presented in the previous sections. The main system parameters are compatible with Table 1 and Table 2 given in Section 4.3.2 for the plain 2-D rake receiver.

Validity of the Gaussian zero-mean approximation for the additional noise component ΔR in (37) was tested through simulations. Totally 500000 samples of each parameter were generated in these simulations. Parameters ρ , ε_τ and $\Delta\varepsilon$ were modeled as zero-mean

Gaussian random variables with variances $1/G$, 0.01 and 0.01, respectively. Parameter ε was assumed to be uniformly distributed over $[0, 2\pi)$. The squared magnitude of the correlation slope represented in (38) was fixed to $\sigma_p^2 = 1$.

Fig. 10 shows the simulated histogram according to (37) for a single interference component. The shape of the $I_e = \Delta R$ distribution in the presence of estimation errors appears to be zero-mean and peaky resembling a Laplace distribution. Fig. 11 depicts the same case for the sum of eight independent and identically distributed (i.i.d.) parameters corresponding, e.g., the joint effect of one user with four multipaths and two receiver antennas ($I_e = KLM\Delta R = 8\Delta R$). It can be observed that even so few components are enough for the Gaussian approximation to hold. In practice, there are far more elements to be summed up.

In contrast to the previous results, the actual correlation matrix was generated according to the asynchronous multiuser model (e.g., [122]) with random binary spreading codes of length 256. The resulting noise enhancement due to crosscorrelation matrix inversion is demonstrated in Fig. 12 as a function of the number of users. Circles in the plot are simulated points and the solid line denotes the second order polynomial fitted to the simulation results. It can be noted that with relatively low user loads the noise enhancement increases almost linearly. However, when the load approaches the spreading code length the noise enhancement explodes rapidly.

Equal gain combined user capacity surface at $\lambda_l = \lambda_m = 0.5$ is depicted in Fig. 13. Capacity losses of the estimated cases increase according to the normalized maximum Doppler shifts. The optimal number of combined diversity branches is in the range of three to five at large Doppler shifts (that result in large estimation errors). Without estimation errors the maximum capacity is reached when all available diversity is utilized. For the maximal ratio combiner (Fig. 14) in the same scenario the capacity surface is almost identical in shape. Only the absolute user capacities are slightly higher.

Equal gain combined user capacity surface for multipath intensity profile $\lambda_l = \lambda_m = 0.75$ is plotted in Fig. 15. In comparison to the previous figures the edges of the plane are now sharper. Clearly, the optimal diversity order diminishes as the MIPs become steeper.

The relative sensitivity function defined in (93) is another way to consider capacity losses. Fig. 17 shows the sensitivity function versus the normalized maximum Doppler shift value with $\lambda_l = \lambda_m = 0.5$ and the number of combined diversity branches being a parameter. The sensitivity of the system increases substantially when the diversity order and/or the Doppler spread increases. The difference between EGC and MRC is minimal. Similar illustrations for parameter setting $\lambda_l = \lambda_m = 0.75$ in Fig. 19 and Fig. 20 reveal that almost all capacity can be lost in fast fading channels due to combining many weak multipaths. In other words, the significant potential capacity gain of the decorrelator (over plain rake) may completely vanish due to the imperfections in a practical implementation.

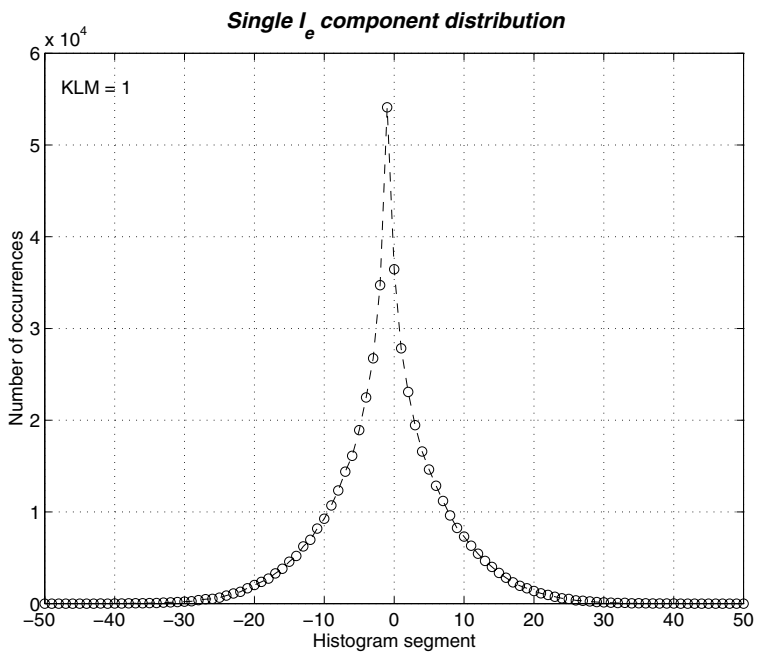


Fig. 10. Simulated histogram for a single interference component ($I_e = \Delta R$).

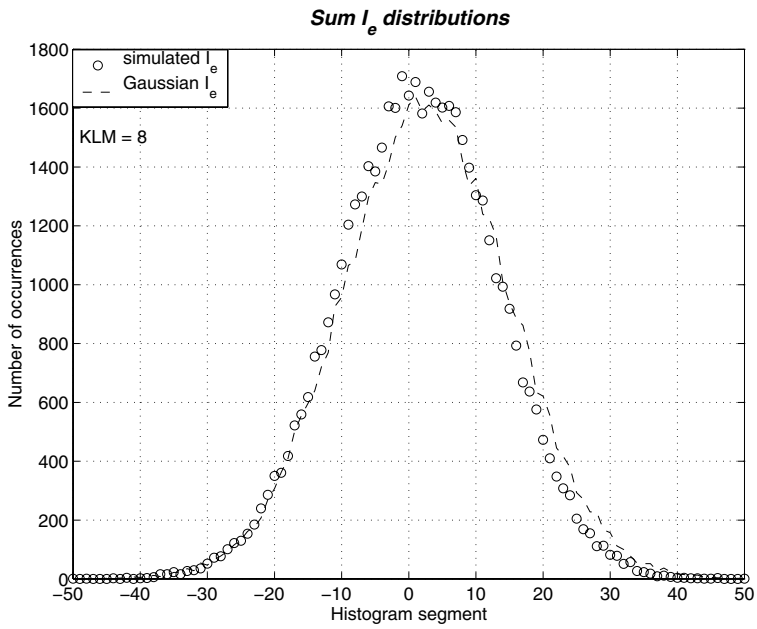


Fig. 11. Histograms for the sum of 8 i.i.d. interference elements ($I_e = 8\Delta R$).

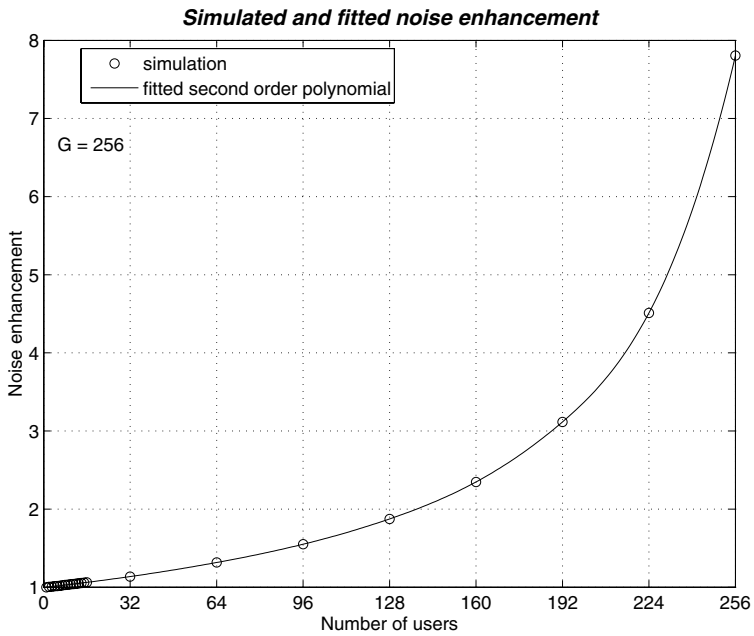


Fig. 12. Simulated and fitted noise enhancement of the decorrelator.

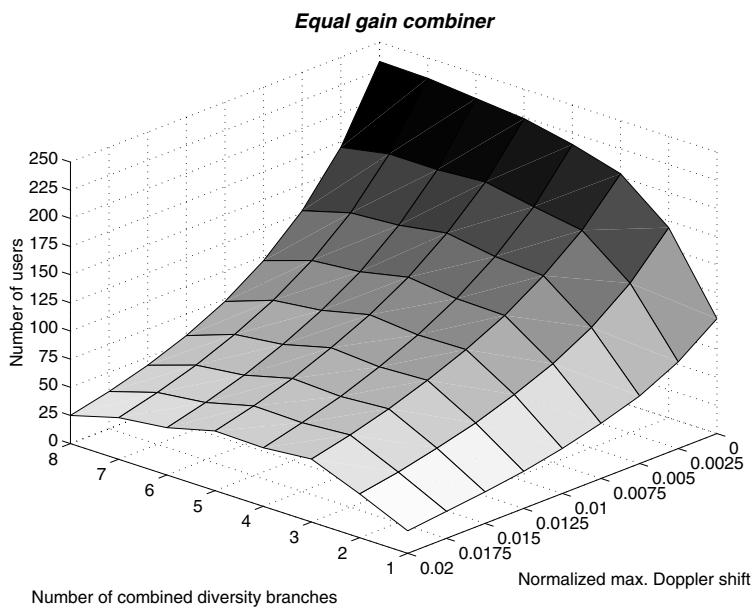


Fig. 13. User capacities with the decorrelator enhanced rake receiver (EGC, $\lambda_l = \lambda_m = 0.5$).

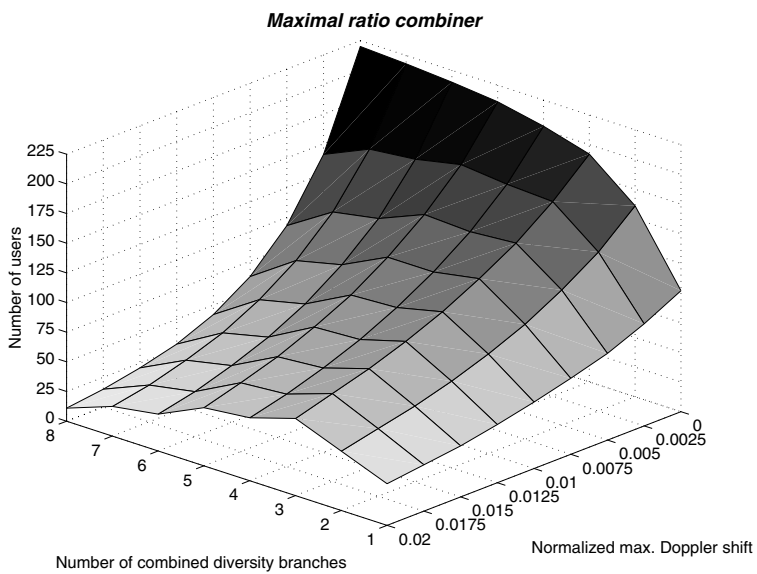


Fig. 14. User capacities with the decorrelator enhanced rake receiver (MRC, $\lambda_l = \lambda_m = 0.5$).

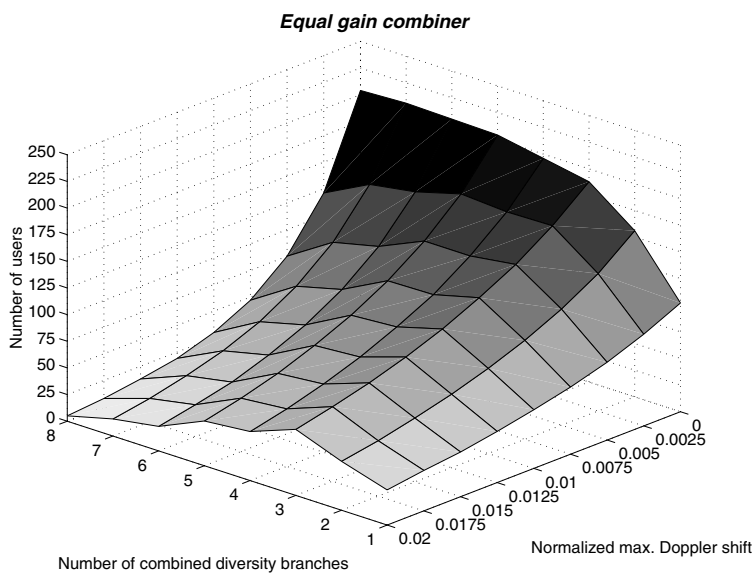


Fig. 15. User capacities with the decorrelator enhanced rake receiver (EGC, $\lambda_l = \lambda_m = 0.75$).

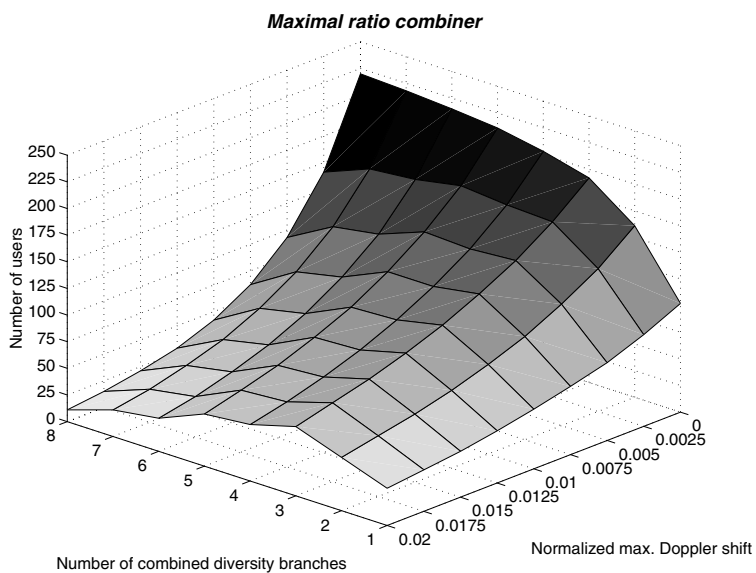


Fig. 16. User capacities with the decorrelator enhanced rake receiver (MRC, $\lambda_l = \lambda_m = 0.75$).

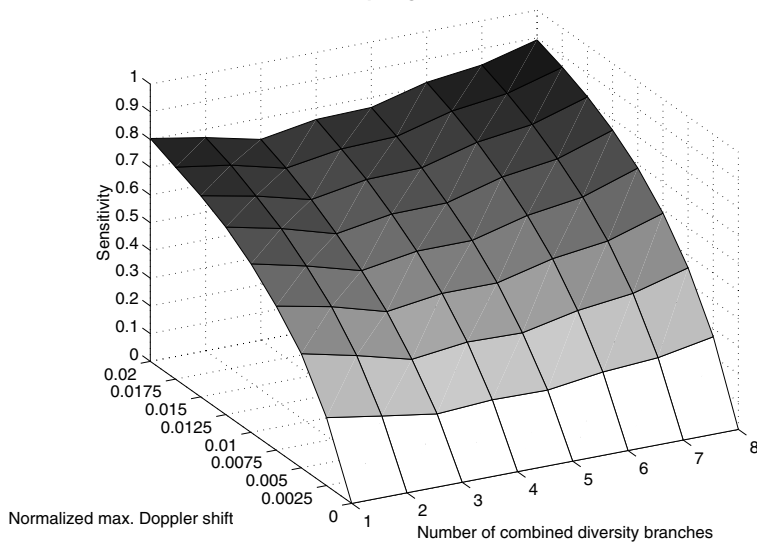
Equal gain combiner

Fig. 17. Sensitivity of the decorrelator enhanced rake receiver (EGC, $\lambda_l = \lambda_m = 0.5$).

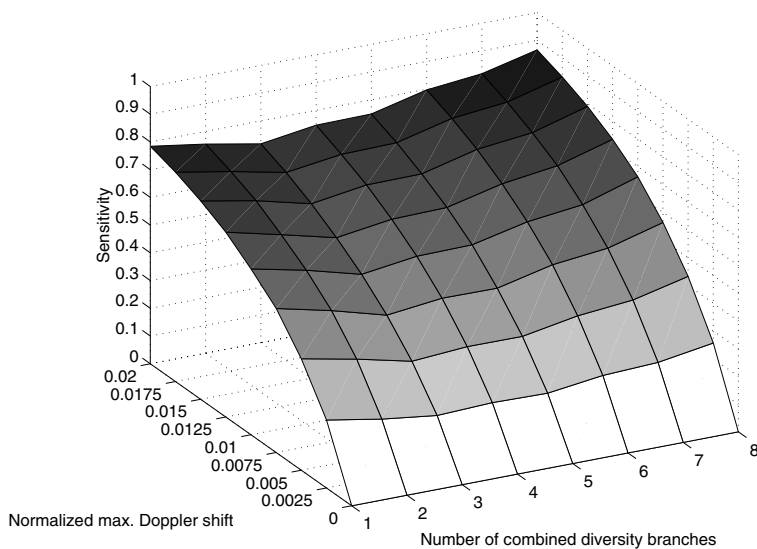
Maximal ratio combiner

Fig. 18. Sensitivity of the decorrelator enhanced rake receiver (MRC, $\lambda_l = \lambda_m = 0.5$).

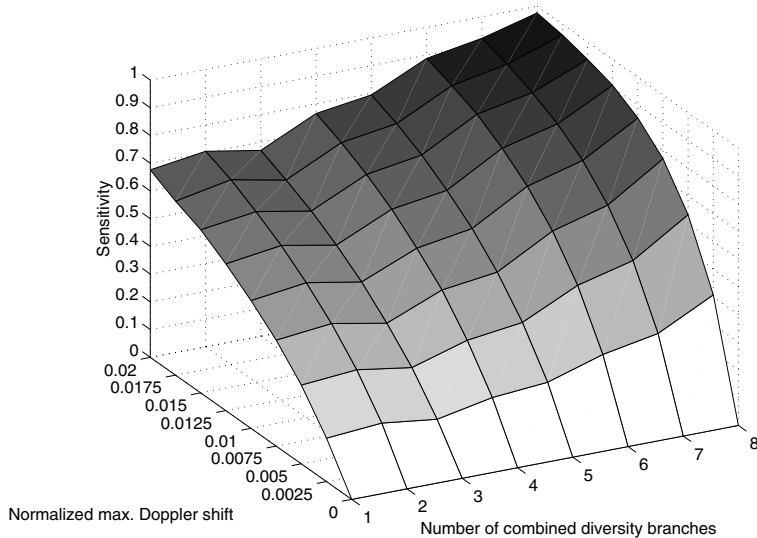
Equal gain combiner

Fig. 19. Sensitivity of the decorrelator enhanced rake receiver (EGC, $\lambda_l = \lambda_m = 0.75$).

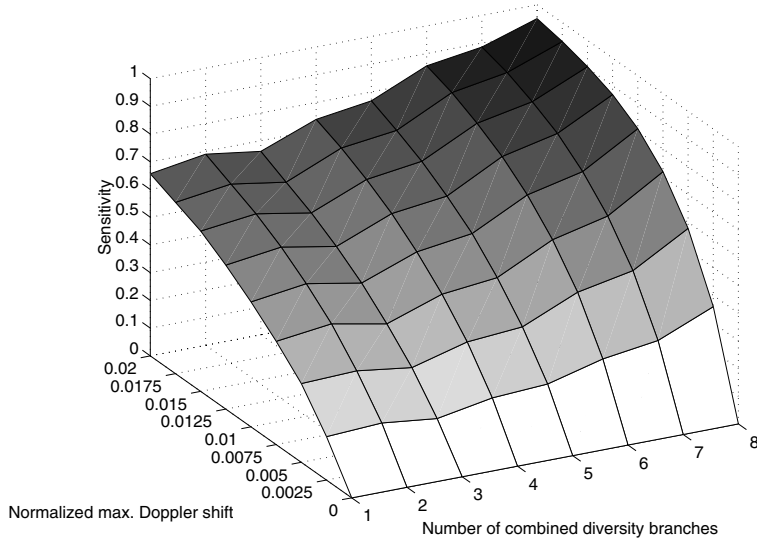
Maximal ratio combiner

Fig. 20. Sensitivity of the decorrelator enhanced rake receiver (MRC, $\lambda_l = \lambda_m = 0.75$).

4.5 Imperfect nonlinear multiuser detector

Let us revise the signal-to-noise ratio modeling started in Section 4.2. If L_0 -fingers rake receiver ($L_0 \leq LM$) with combiner coefficients w_{kr} ($r = 1, 2, \dots, L_0$) and interference canceller are used, the signal-to-noise ratio (65) will become

$$Y_{bk} = \frac{r_k^{(L_0)}}{I_{oc}(k, \mathbf{a}, \mathbf{c}, \mathbf{r})K + \zeta_0 \eta R_b / S}, \quad (94)$$

where ζ_0 has already been defined in (67) and is due to Gaussian noise processing in the rake receiver, and the noise density η_0 becomes η due to additional signal processing. The intracell multiuser interference is of the form

$$\begin{aligned} I_{oc}(k, \mathbf{a}, \mathbf{c}, \mathbf{r}) &= \frac{1}{K} \sum_{\substack{k'=1 \\ k' \neq k}}^K \sum_{r=1}^{L_0} \sum_{l=1}^L \sum_{m=1}^M w_{kr}^2 \alpha_{k'lm} (1 - C_{k'lm}) + \frac{1}{K} \sum_{\substack{r=1 \\ l \neq r}}^{L_0} \sum_{l=1}^L \sum_{m=1}^M w_{kr}^2 \alpha_{klm} (1 - C_{klm}) \\ &= \frac{1}{K} \left\{ \mathbf{w}_k \left(\mathbf{1} \cdot \boldsymbol{\alpha}_{klm} \cdot \mathbf{1}^T \right) \mathbf{w}_k^T \right\} \end{aligned} \quad (95)$$

with $\boldsymbol{\alpha}_{klm}$ being a matrix of size $K \times LM$ with coefficients $\|\alpha_{k'lm}(1 - C_{k'lm})\|$ except for $\alpha_{krm}(1 - C_{krm}) = 0$ and C_{klm} is efficiency of the canceller. The following equation relates bit error probability P_e to the average bit values b and their estimates \hat{b} as

$$\overline{\hat{b}\hat{b}} = 1 - 2P_e. \quad (96)$$

For the system performance evaluation a model for the canceller efficiency is needed. Linear multiuser structures have restrictions in the use for mobile communication systems applying long spreading codes. An alternative approach is nonlinear (multistage) multiuser detection that would include channel estimation parameters too. This would be based on interference estimation and cancellation schemes (OKI standard-IS-665/ITU recommendation M.1073 or UMTS defined by ETSI) [329, 330].

In general, if the estimates of (53) and (54) are denoted as $\hat{\mathbf{y}}_i$ and $\hat{\mathbf{y}}_q$ then the residual interference after cancellation can be expressed as

$$\Delta \mathbf{y}_i = \mathbf{y}_i - \hat{\mathbf{y}}_i, \quad \Delta \mathbf{y}_q = \mathbf{y}_q - \hat{\mathbf{y}}_q, \quad \Delta \mathbf{y} = \Delta \mathbf{y}_i + j \Delta \mathbf{y}_q = \text{vec}\{\Delta \mathbf{y}_\xi\}, \quad (97)$$

where index $\xi \Rightarrow k, l, m$ spans all combinations of k , l and m . By using (97) each component $\alpha_{klm}(1 - C_{klm})$ in (95) can be obtained as a corresponding entry of $\text{vec}\left\{ \left| \Delta \mathbf{y}_\xi \right|^2 \right\}$. To further elaborate these components a simplified notation and analysis will be performed.

After frequency downconversion and despreading, the received signal of user k through path l at the antenna m would have the form

$$\hat{S}_{klm} = \hat{A}_{klm} \hat{b}_k \cos \hat{\theta}_{klm} = (A_{klm} + \Delta A_{klm}) \hat{b}_k \cos(\theta_{klm} + \varepsilon_{\theta klm}) \quad (98)$$

for a single signal component and

$$\hat{S}_{klm}^i = \hat{A}_{klm} \hat{b}_{ki} \cos \hat{\theta}_{klm} + \hat{A}_{klm} \hat{b}_{kq} \sin \hat{\theta}_{klm}, \quad (99)$$

$$\hat{S}_{klm}^q = -\hat{A}_{klm} \hat{b}_{ki} \sin \hat{\theta}_{klm} + \hat{A}_{klm} \hat{b}_{kq} \cos \hat{\theta}_{klm} \quad (100)$$

for a complex (I&Q) signal structure. In a chosen receiver branch, components \hat{S}_{klm}^i and \hat{S}_{klm}^q correspond to Δy_{iklm} and Δy_{qklm} . Parameter A_{klm} includes both amplitude and correlation functions. In (98), ΔA_{klm} is the amplitude estimation error and $\varepsilon_{\theta klm}$ is the phase estimation error. The canceller will create $S_{klm} - \hat{S}_{klm} = \Delta S_{klm}$ and the power of this residual error would be

$$E_{\theta}[(\Delta S_{klm})^2] = E_{\theta}[A_{klm} b_k \cos \theta_{klm} - (A_{klm} + \Delta A_{klm}) \hat{b}_k \cos(\theta_{klm} + \varepsilon_{\theta klm})]^2, \quad (101)$$

where $E_{\theta}[\cdot]$ stands for averaging with respect to θ_{klm} and b_k . Parameter $(\Delta S_{klm})^2$ corresponds to $|\Delta y_{klm}|^2$. This can be represented as

$$E_{\theta}[(\Delta S_{klm})^2] = \alpha_{klm} [1 + (1 + \varepsilon_a)^2 - 2(1 + \varepsilon_a)(1 - 2P_e) \cos \varepsilon_{\theta}]. \quad (102)$$

From this equation we have

$$1 - C_{klm} = \frac{1}{\alpha_{klm}} E_{\theta}[(\Delta S_{klm})^2] \quad (103)$$

and

$$C_{klm} = 2(1 + \varepsilon_a)(1 - 2P_e) \cos \varepsilon_{\theta} - (1 + \varepsilon_a)^2. \quad (104)$$

By expanding $\cos \varepsilon_{\theta}$ to a truncated series $1 - \varepsilon_{\theta}^2 / 2$ and averaging gives

$$C_{klm} \cong 2(1 + \varepsilon_a)(1 - 2P_e)(1 - \sigma_{\theta}^2) - (1 + \varepsilon_a)^2. \quad (105)$$

For zero-mean ε_{θ}

$$\sigma_{\theta}^2 = E[\varepsilon_{\theta}^2 / 2] \quad (106)$$

is the carrier phase tracking error variance. For the complex (I&Q) signal structure, cancellation efficiencies in the I- and Q-channels can be represented as

$$C_{klm}^i = 4(1 + \varepsilon_a)(1 - 2P_e)(1 + \sigma_\theta^2) - 2(1 + \varepsilon_a)^2 - 1, \quad (107)$$

$$C_{klm}^q = 4(1 + \varepsilon_a)(1 - 2P_e)(1 + \sigma_\theta^2) - 2(1 + \varepsilon_a)^2 - 1. \quad (108)$$

So, in this case the canceller efficiency is expressed in terms of amplitude, phase and data estimation errors. These results should be now used for analysis of the impact of large scale of channel estimators on overall CDMA network sensitivity. The estimator dependent parameter estimation error variance should be directly used in (105), (107), and (108) for the cancellation efficiency and in (69)–(80) for the rake receiver. Again, previously defined expressions for carrier phase, code delay, and amplitude estimation error variances can be applied. If interference cancellation is performed prior to the parameter estimation, N_0 is obtained from $I_{oc}(\cdot)$ defined by (95). If parameter estimation is done without interference cancellation the same $I_{oc}(\cdot)$ is used with $C_{klm} = 0$.

4.5.1 Approximations

If the channel estimation is assumed to be perfect ($\varepsilon_a = \varepsilon_\theta = 0$) the cancellation efficiency C_{klm} becomes

$$C_{klm} = 2(1 - 2P_e) - 1 = 1 - 4P_e \quad (109)$$

with $P_e = (1/2)\exp(-y/2)$ for differentially coherent phase shift keying (DPSK) modulation [191] and $P_e = (1/2)\text{erfc}(\sqrt{y})$ for coherent phase shift keying (PSK) [191] in AWGN channel. Similarly, in uncoded flat Rayleigh fading 1-path channel $P_e = \frac{1}{2}\left(1 - \frac{y}{1+y}\right)$ for differentially coherent [191] and $P_e = \frac{1}{2}\left(1 - \sqrt{\frac{y}{1+y}}\right)$ for coherent PSK [191] are valid. For these modulation formats (109) becomes

$$C_{klm} = 1 - 2e^{-y} \text{ for DPSK in AWGN,} \quad (110)$$

$$C_{klm} = 1 - 2\text{erfc}(\sqrt{y}) \text{ for PSK in AWGN,} \quad (111)$$

$$C_{klm} = 2\frac{y}{1+y} - 1 \text{ for DPSK in Rayleigh channel, and} \quad (112)$$

$$C_{klm} = 2\sqrt{\frac{y}{1+y}} - 1 \text{ for PSK in Rayleigh channel.} \quad (113)$$

Fig. 21 illustrates theoretical bit error probabilities for the aforementioned modulation formats and channel models. The corresponding interference cancellation efficiencies (110)–(113) are depicted in Fig. 22. From Fig. 22 it is easy to observe that at large SNRs, cancellation coefficients approach a value of 1. At small SNRs, cancellation efficiencies asymptotically approach -1 . Let us look at DPSK modulation in AWGN as an example. From (110), we can simply approximate for small y , $e^{-y} \cong 1 - y$, which leads to $C_{klm} \cong 2y - 1$. Therefore, while $y \rightarrow 0$, $C_{klm} \rightarrow -1$. This can be presented as $C_{klm} = 2Y_{bk} - 1$, where Y_{bk} is given by (94). Bearing in mind that Y_{bk} depends on C_{klm} , the whole equation can be solved through an iterative procedure starting up with an initial value of $C_{klm} = 0$, $\forall k, l, m$. Similar approximations can be obtained for σ_θ^2 and ε_a . From a practical point of view, an attractive solution could be a scheme that would estimate and cancel only the strongest interference (e.g., successive interference cancellation schemes [157, 114]).

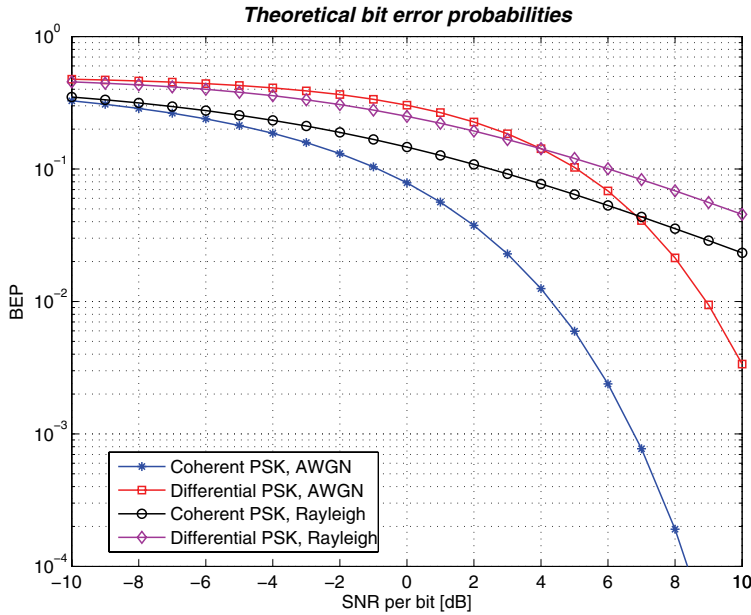


Fig. 21. Theoretical bit error probabilities for different modulation formats and channels.

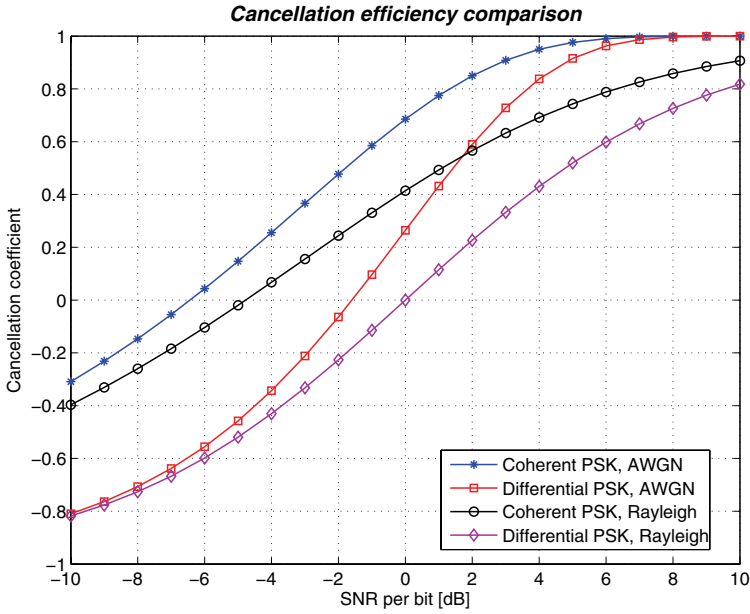


Fig. 22. Comparison of interference cancellation efficiencies in (110)–(113).

4.5.2 Outage probability

We will start from (94) and look at the average system performance for $\rho^2 = 1/G$ where $G = W/R_b$ is the system processing gain and W is the system bandwidth (chip rate). The average signal-to-noise ratio will be expressed as

$$\bar{Y}_b = \frac{r^{(L_0)}G}{I_{oc}(\mathbf{a})K + \zeta_0\eta'W/S}. \quad (114)$$

Again, assume that there is a performance criterion for the quality of transmission ($P_e = 10^{-e}$) that can be achieved with the given $\text{SNR} = Y_0$. Then the equivalent average interference density, in the absence of intracell interference, becomes $\eta_0 = I_{oic} + I_{oin} + \eta_{th}$, and the signal-to-noise ratio will be

$$Y_0 = \frac{r^{(L_0)}G}{\eta_0}. \quad (115)$$

While the outage probability P_{out} is used as a performance criterion, we need to evaluate [12]

$$\begin{aligned}
P_{out} &= \text{Prob.}(P_e > 10^{-e}) \\
&= \text{Prob.}\left(\text{MAI} + \frac{\eta W}{S} > \eta_0\right) \\
&= \text{Prob.}\left(\text{MAI} > \eta_0 - \frac{\eta W}{S}\right) \\
&= \text{Prob.}(\text{MAI} > \delta),
\end{aligned} \tag{116}$$

where δ is given as

$$\delta = \frac{r^{(L_0)}G}{Y_0} - \frac{\eta W}{S}. \tag{117}$$

It can be shown that this outage probability, P_{out} , can be represented by the Gaussian complementary distribution function as

$$P_{out} = Q\left(\frac{\delta - m_g}{\sigma_g}\right), \tag{118}$$

where m_g and σ_g are the mean value and the standard deviation of the overall interference, respectively. For brevity, the outage analysis is not carried out in this framework.

4.5.3 User capacity and sensitivity

From (114) we have the maximum system capacity without nonidealities as

$$K_{NL}^{\max} = \left\lfloor \frac{r_0^{(L_0)}G}{Y_0 I_{oc0}(\mathbf{a})} - \frac{\zeta_0 \eta W}{S I_{oc0}(\mathbf{a})} \right\rfloor. \tag{119}$$

Due to imperfections in the operation of the rake receiver and interference canceller the maximum capacity will be reduced to

$$K_{NL} = \left\lfloor \frac{r^{(L_0)}G}{Y_0 I_{oc}(\mathbf{a})} - \frac{\zeta_0 \eta W}{S I_{oc}(\mathbf{a})} \right\rfloor, \tag{120}$$

where the ideal parameters $r_0^{(L_0)}$ and $I_{oc0}(\mathbf{a})$ are now replaced by real parameters $r^{(L_0)}$ and $I_{oc}(\mathbf{a})$ that take into account imperfections in MAI cancellation and rake combining. The system sensitivity function is defined the same principle as in (85) for the rake receiver and in (93) for the decorrelator, leading to

$$\Re_{NL} = \frac{K_{NL}^{\max} - K_{NL}}{K_{NL}^{\max}} = \frac{1}{K_{NL}^{\max}} \left\{ \frac{\Delta r^{(L_0)} G}{Y_0 I_{oc}(\mathbf{a}) I_{oc0}(\mathbf{a})} - \frac{\zeta_0 \eta' W \Delta I_{oc}(\mathbf{a})}{S I_{oc}(\mathbf{a}) I_{oc0}(\mathbf{a})} \right\}, \quad (121)$$

where

$$\Delta r^{(L_0)} = r_0^{(L_0)} I_{oc}(\mathbf{a}) - r^{(L_0)} I_{oc0}(\mathbf{a}), \quad (122)$$

$$\Delta I_{oc}(\mathbf{a}) = I_{oc}(\mathbf{a}) - I_{oc0}(\mathbf{a}). \quad (123)$$

4.5.4 Numerical examples

In this section some numerical results are presented to illustrate effective user capacities and sensitivity functions for the combined use of rake and interference cancellation receiver. The results are obtained under the common parameters outlined previously for the rake receiver only in Section 4.3.2 on Table 1 and Table 2. Parameter estimation is made before interference cancellation (worst case). Cancellation efficiency for maximum capacity is calculated according to (113). When estimation errors are included, cancellation efficiencies are calculated according to (105).

Fig. 23 shows the user capacity versus the number of rake fingers and the normalized maximum Doppler shift for the equal gain combiner (EGC). The multipath intensity profile has decay parameter values $\lambda_l = \lambda_m = 0.5$. One can see that when the number of combined diversity branches becomes large enough, the capacity starts to saturate due to imperfections in the parameter estimation. The situation is more critical if the normalized fading rate ($f_D T$) is higher.

Similar capacity surface for maximal ratio combiner (MRC) is plotted in Fig. 24. Without any parameter estimation errors the MRC can utilize full diversity order, yielding very high peak capacity. However, in the presence of estimation errors, the capacity values do not deviate so much from the EGC comparables.

A more steeply decaying MIP, $\lambda_l = \lambda_m = 0.75$, is evaluated in Fig. 25 with an equal gain combining receiver. The capacity surface resembles the previous case but now the user capacity breaks down at a lower diversity order when the estimation errors increase. Again, the maximal ratio combiner represented in Fig. 26 offers gain over EGC without any estimation errors for $L_0 = 8$. Otherwise, the performance of EGC and MRC is in a close match.

To better illustrate sensitivity to capacity losses, the sensitivity function is used. In Fig. 27, user capacity sensitivity function versus the number of combined diversity branches and normalized maximum Doppler shift is plotted for EGC, $\lambda_l = \lambda_m = 0.5$. The sensitivity increases fairly linearly as a function of $f_D T$. Moreover, for large L_0 the sensitivity (percentage of lost capacity) is slightly increased due to imperfections in the parameter estimation process.

In the case of MRC, the sensitivity surface is shown in Fig. 28. In comparison to the EGC, the main difference is noted at high diversity orders ($L_0 > 4$). There the sensitivity rises very rapidly and becomes nonlinear with respect to $f_D T$. It is interesting to note, that at worst, the capacity loss can exceed 90%. When the estimation imperfections are large the MRC loses its performance more than the EGC because of the amplitude estimation errors.

Sensitivities for MIP with $\lambda_l = \lambda_m = 0.75$ are shown in Fig. 29 (EGC) and in Fig. 30 (MRC). Now the slopes in the surfaces are even steeper.

Figs. 31–34 illustrate intracell MAI cancellation coefficient C_{klm} values versus the number of EGC combined diversity branches and the number of users. In Fig. 31 and Fig. 32, the MIP is parameterized as $\lambda_l = \lambda_m = 0.5$ and the normalized maximum Doppler shift $f_D T = 0$ and $f_D T = 0.02$, respectively. In Figs. 33 and 34 $\lambda_l = \lambda_m = 0.75$. These results indicate that in perfect conditions the cancellation efficiency improves as a function of receiver diversity order. However, imperfections due to increased user load and faster fading are reflected in deteriorated performance. In the extreme conditions C_{klm} will be negative, which means that interference will be increased rather than decreased.

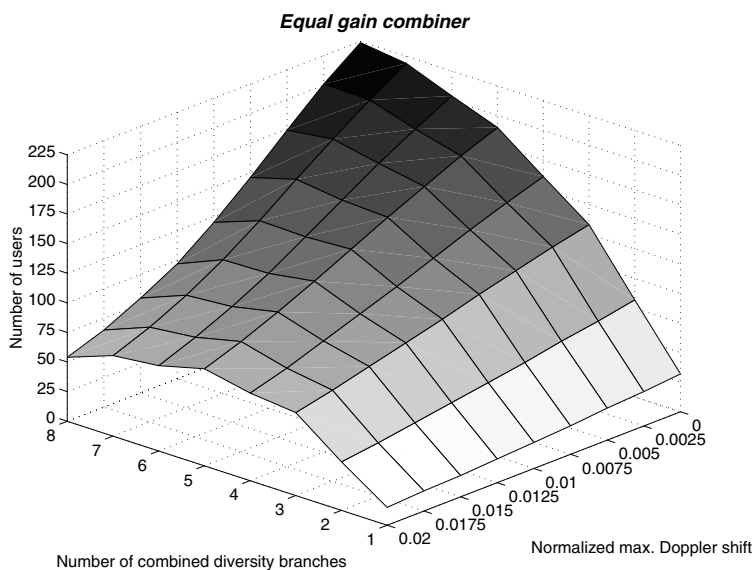


Fig. 23. User capacities with the nonlinear interference cancellation enhanced rake receiver (EGC, $\lambda_l = \lambda_m = 0.5$).

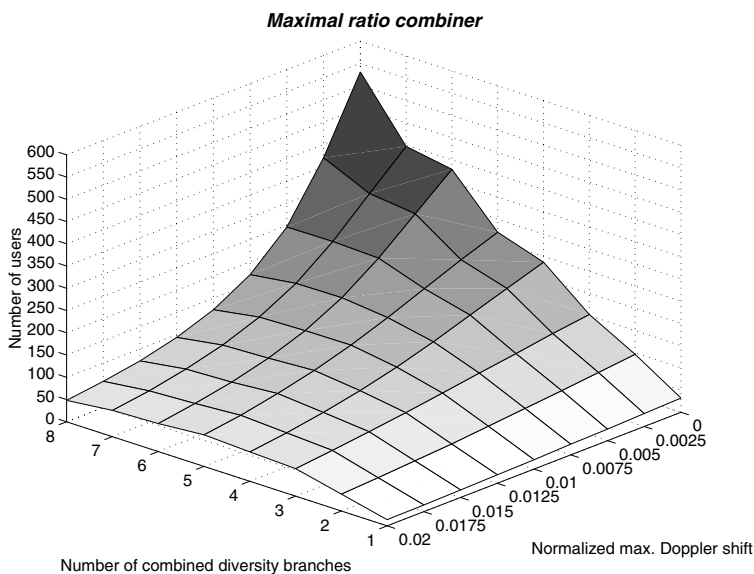


Fig. 24. User capacities with the nonlinear interference cancellation enhanced rake receiver (MRC, $\lambda_l = \lambda_m = 0.5$).

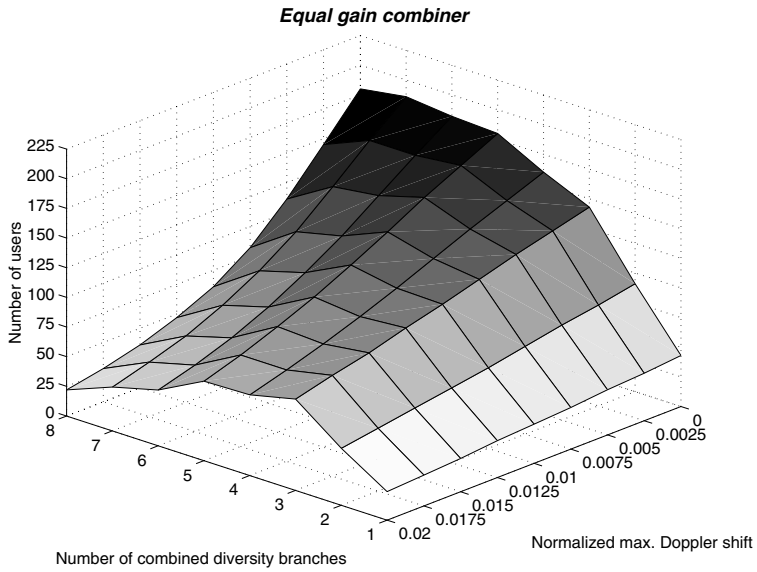


Fig. 25. User capacities with the nonlinear interference cancellation enhanced rake receiver (EGC, $\lambda_l = \lambda_m = 0.75$).

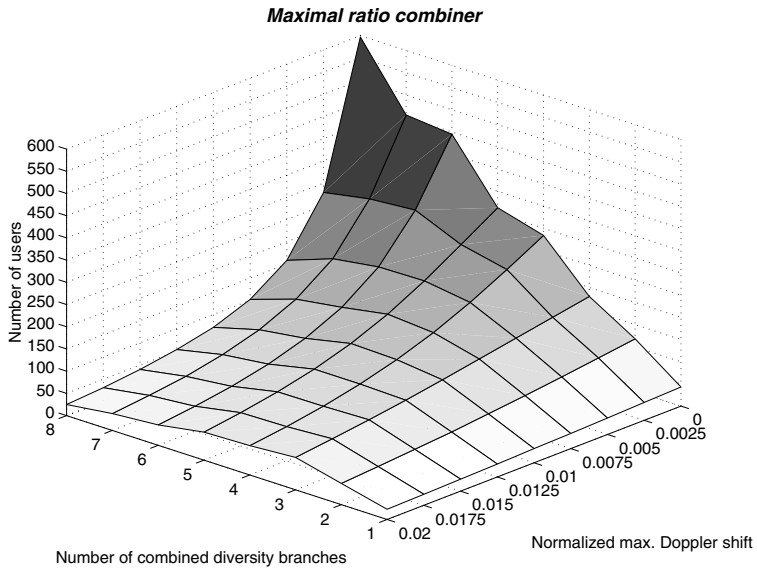


Fig. 26. User capacities with the nonlinear interference cancellation enhanced rake receiver (MRC, $\lambda_l = \lambda_m = 0.75$).

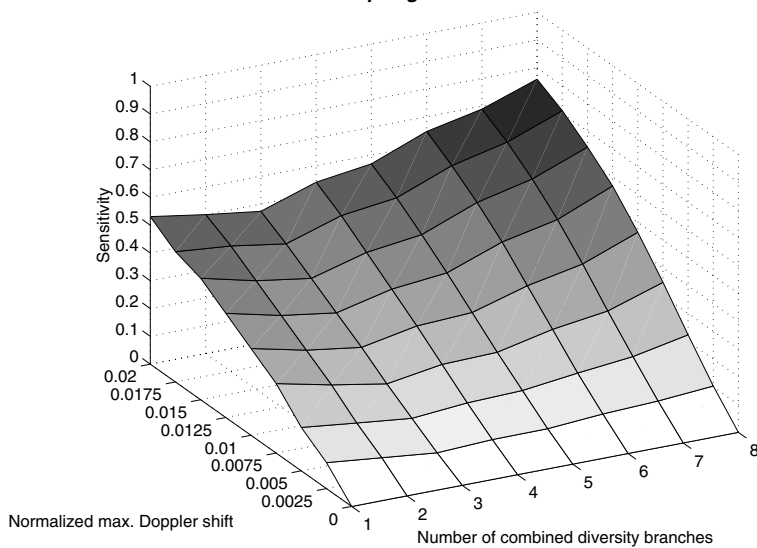
Equal gain combiner

Fig. 27. Sensitivity of the nonlinear interference cancellation enhanced rake receiver (EGC, $\lambda_l = \lambda_m = 0.5$).

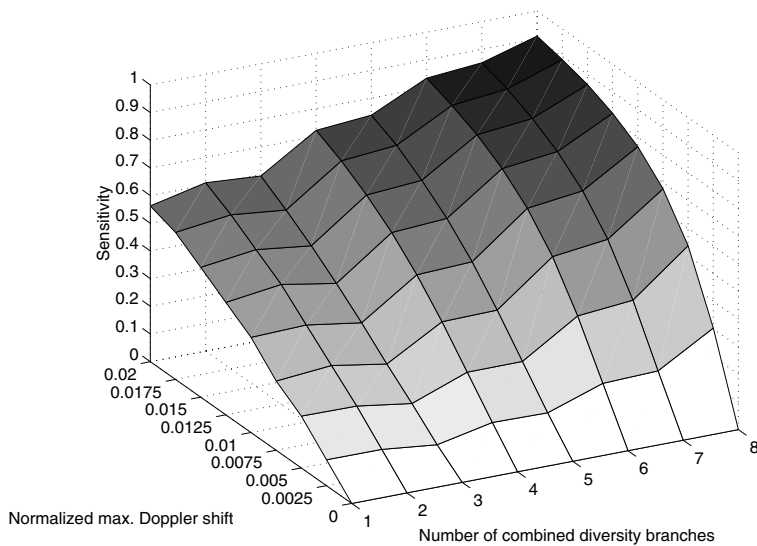
Maximal ratio combiner

Fig. 28. Sensitivity of the nonlinear interference cancellation enhanced rake receiver (MRC, $\lambda_l = \lambda_m = 0.5$).

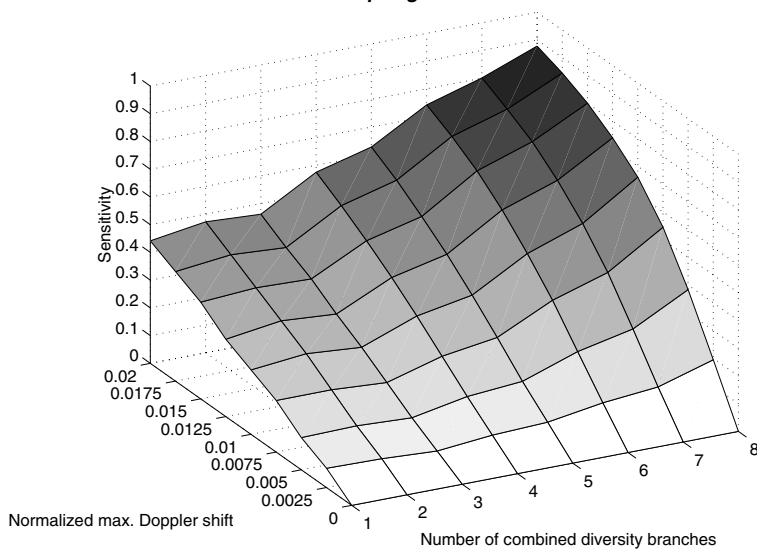
Equal gain combiner

Fig. 29. Sensitivity of the nonlinear interference cancellation enhanced rake receiver (EGC, $\lambda_l = \lambda_m = 0.75$).

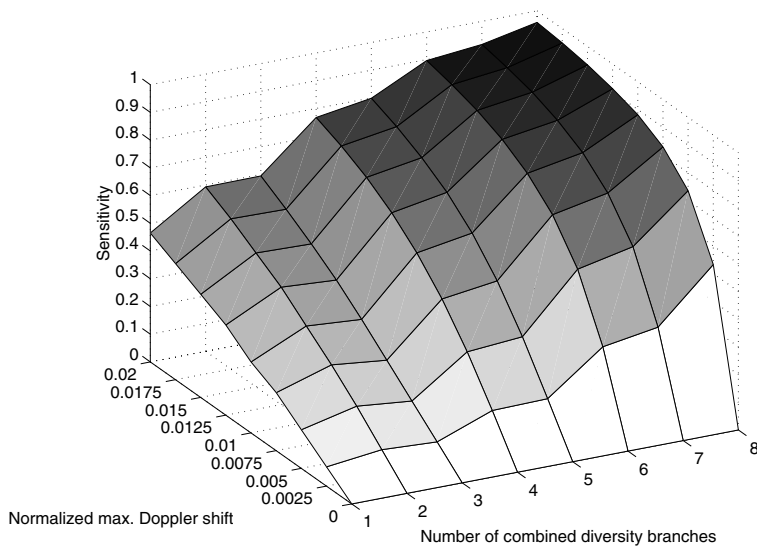
Maximal ratio combiner

Fig. 30. Sensitivity of the nonlinear interference cancellation enhanced rake receiver (MRC, $\lambda_l = \lambda_m = 0.75$).

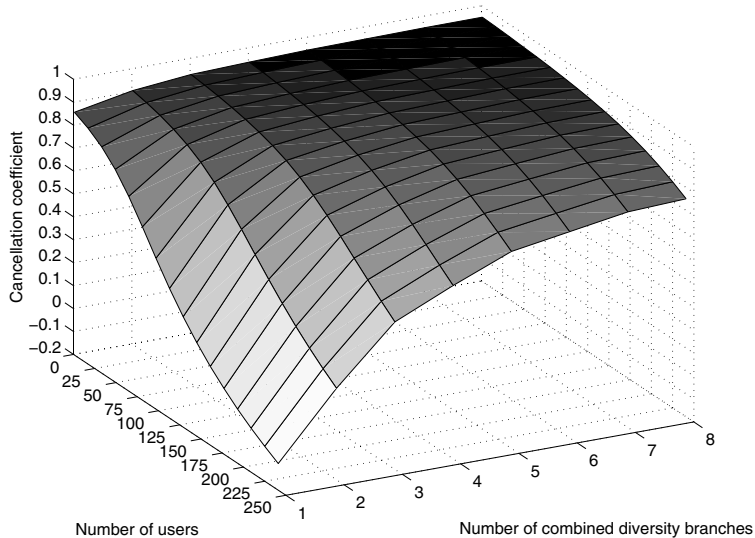
Equal gain combiner

Fig. 31. Interference cancellation efficiency (EGC, $\lambda_l = \lambda_m = 0.5$, $f_D T = 0$).

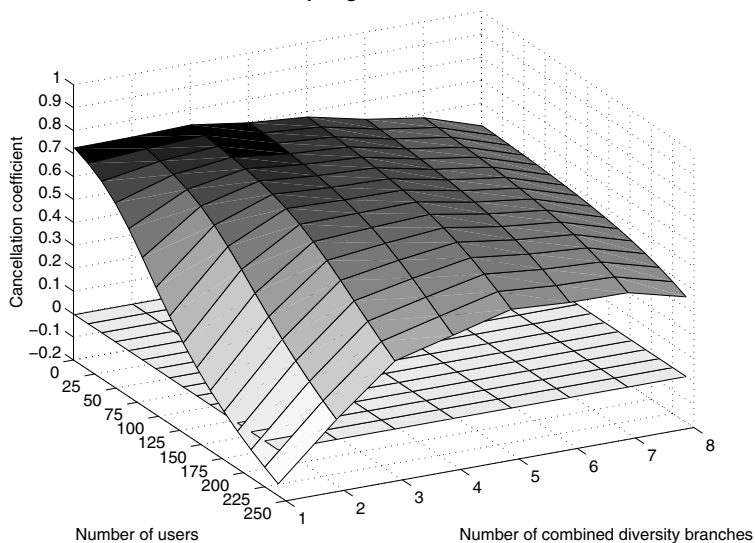
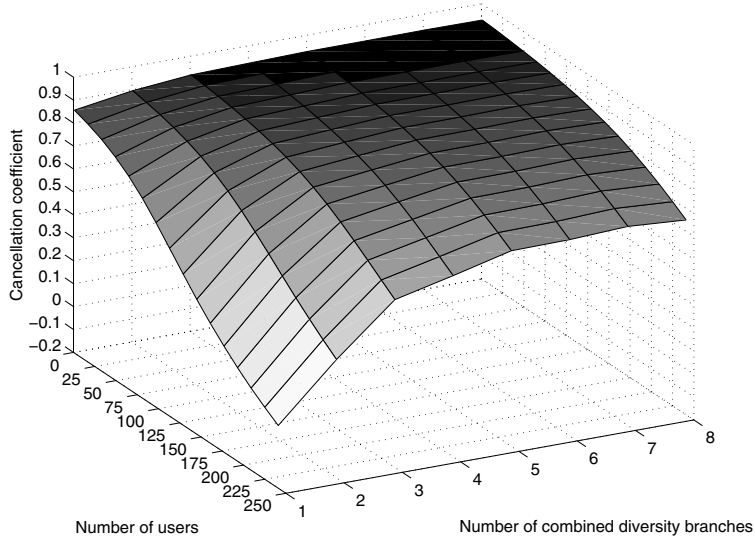
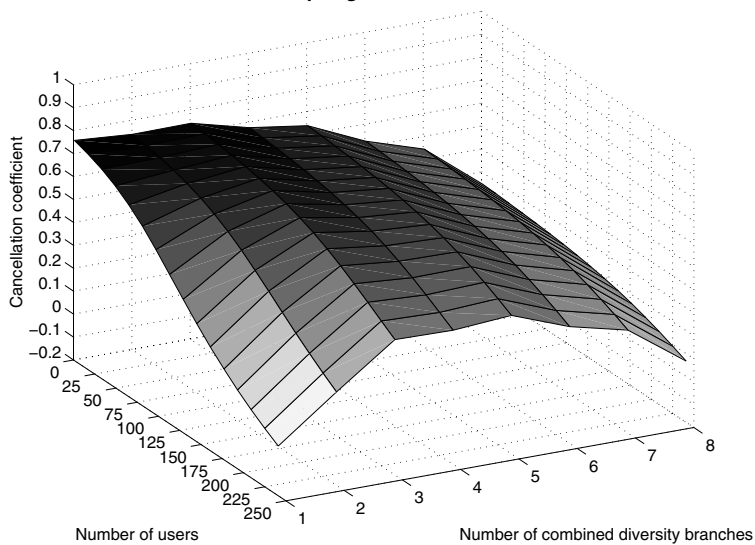
Equal gain combiner

Fig. 32. Interference cancellation efficiency (EGC, $\lambda_l = \lambda_m = 0.5$, $f_D T = 0.02$).

Equal gain combiner**Fig. 33. Interference cancellation efficiency (EGC, $\lambda_l = \lambda_m = 0.75, f_D T = 0$).****Equal gain combiner****Fig. 34. Interference cancellation efficiency (EGC, $\lambda_l = \lambda_m = 0.75, f_D T = 0.02$).**

4.6 Performance comparison

This section includes capacity comparison under unified parameter settings when plain space-time rake receivers, decorrelating space-time rake receivers, and nonlinear interference canceller enhanced space-time rake receivers are utilized as the receiver alternatives.

Fig. 35 shows user capacities at three normalized maximum Doppler shifts $f_D T = 0.01$, 0.015, and 0.02 for equal gain combining at $\lambda_l = \lambda_m = 0.5$. Clearly, the multiuser detectors outperform plain rake in most of the cases. For one or two combined diversity branches the decorrelator provides highest capacity. When the diversity order is increased the nonlinear interference cancellation becomes more efficient than decorrelation. However, both schemes suffer from significant losses as the fading worsens. It is also noteworthy to observe that the decorrelator can actually do worse than the plain rake combiner when the estimation errors are large.

Fig. 36 presents a similar comparison in the case of maximal ratio combining. Absolute user capacities are now slightly higher than with equal gain combining. Otherwise, similar behavior and relations between receiver variants is observed.

Figs. 37 and 38 illustrate EGC and MRC user capacities for channel profiles with $\lambda_l = \lambda_m = 0.75$. Due to the steeper decay than in the previous plots, less diversity is needed for the maximum capacity. Impairments accumulate severely when the diversity order is increased. As a result the capacity drop for multiuser receivers becomes more pronounced than in the previous examples. For the conventional rake receiver the capacity does not degrade so dramatically, if at all. For MRC, it is beneficial to maximize the available diversity order, even in the presence of channel impairments.

Fig. 39 depicts relative EGC capacities of the decorrelator $(K_{DEC} - K_{MF})/K_{MF}$ and nonlinear detector $(K_{NL} - K_{MF})/K_{MF}$ with respect to plain rake receiver capacity with various degrees of fading rates (comparable to Fig. 35). Quite high gains (up to 7) can be realized. However, in most of the ranges the multiuser receiver gain varies between one and three. The horizontal thick line at zero level corresponds to the reference capacity obtained with the plain rake receiver.

Fig. 40 respectively shows the corresponding capacity gains while the maximal ratio combining is employed at the receivers. Somewhat higher gains can be noticed. Otherwise, the EGC and MRC curves manifest strong similarity.

In the steeply decaying MIP the capacity gains are even more concentrated at low numbers of rake fingers. This is clarified in Fig. 41, which plots relative EGC capacities of Fig. 37. In order to maintain the gain at high diversity orders, more robust estimators against imperfections would be required.

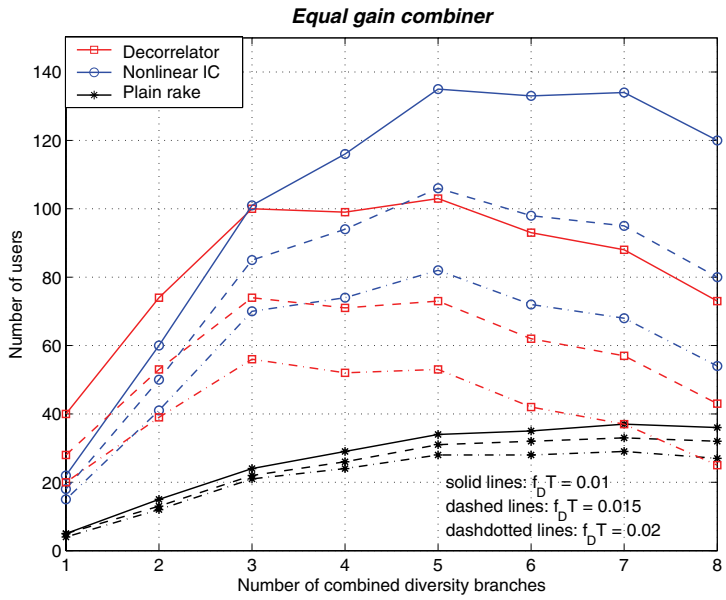


Fig. 35. Comparative user capacities (EGC, $\lambda_l = \lambda_m = 0.5$).

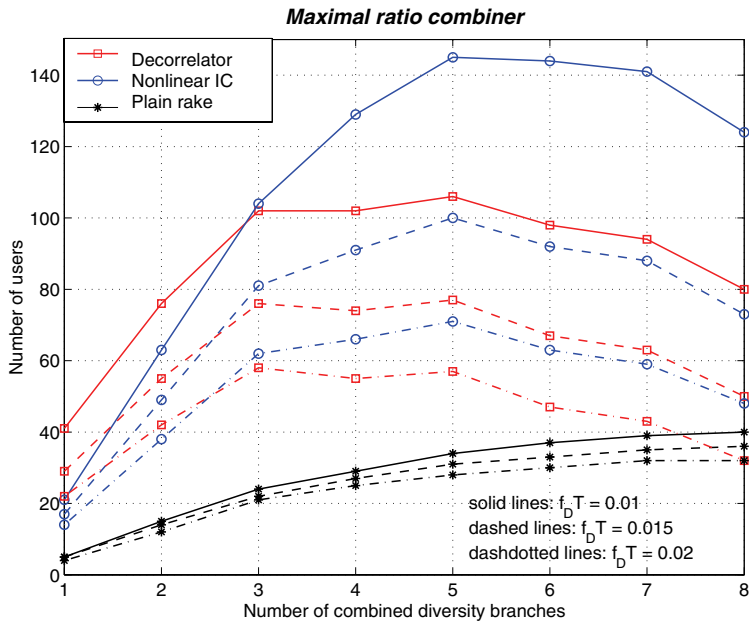


Fig. 36. Comparative user capacities (MRC, $\lambda_l = \lambda_m = 0.5$).

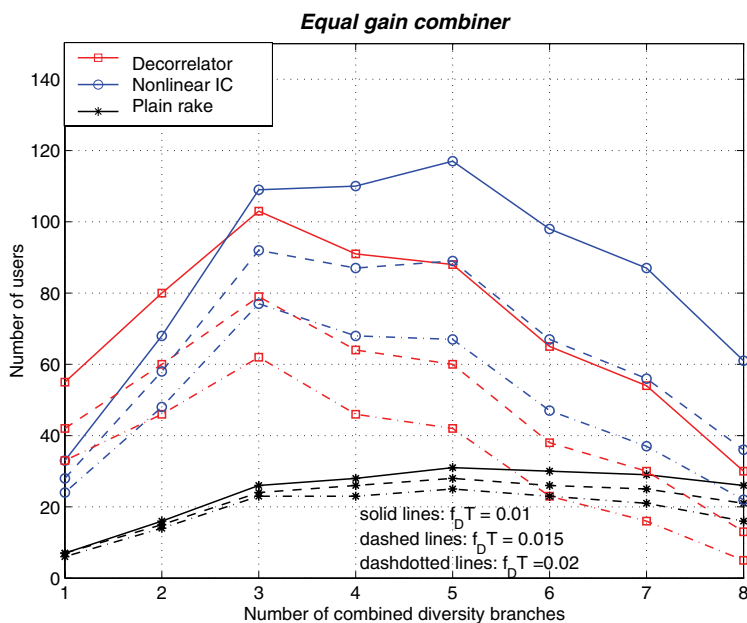


Fig. 37. Comparative user capacities (EGC, $\lambda_l = \lambda_m = 0.75$).

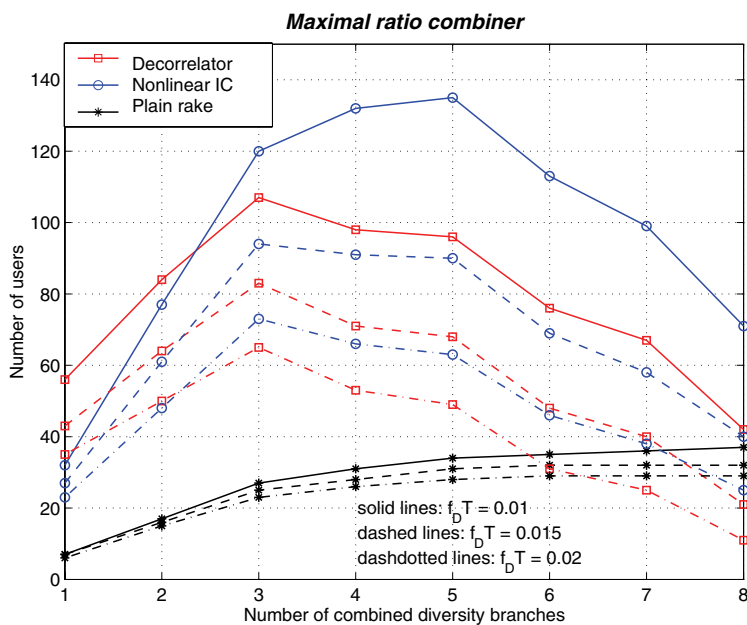


Fig. 38. Comparative user capacities (MRC, $\lambda_l = \lambda_m = 0.75$).

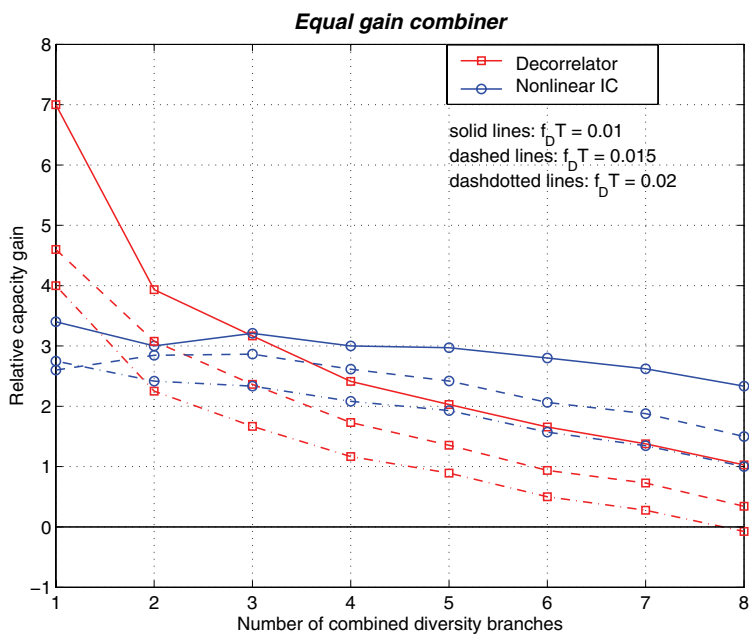


Fig. 39. Relative capacity gains of multiuser receivers over plain rake (EGC, $\lambda_l = \lambda_m = 0.5$).

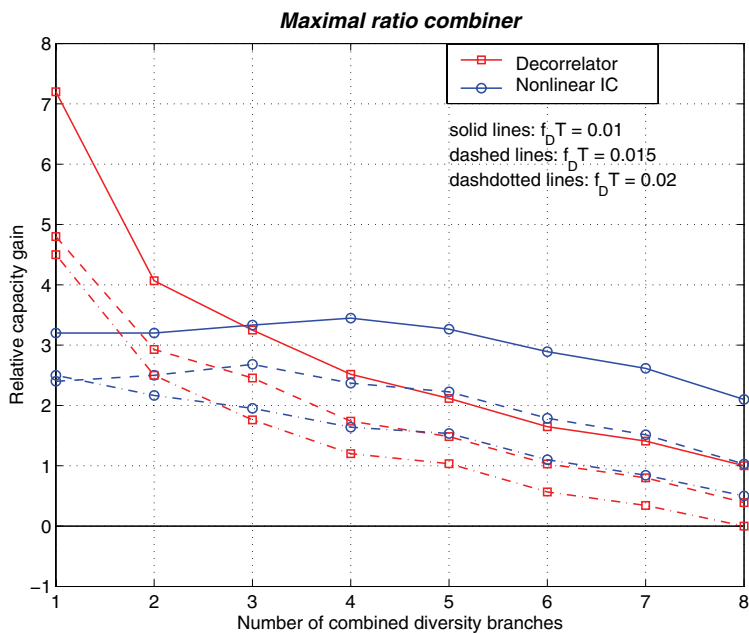


Fig. 40. Relative capacity gains of multiuser receivers over plain rake (MRC, $\lambda_l = \lambda_m = 0.5$).

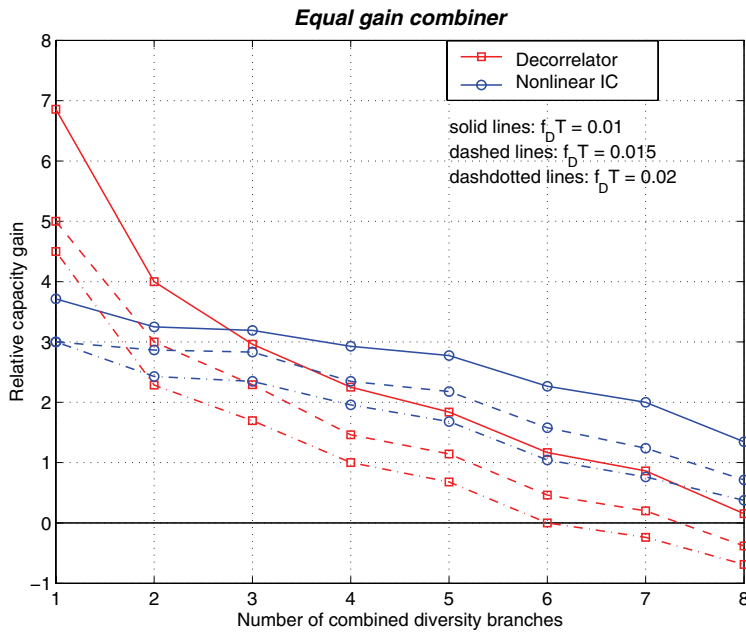


Fig. 41. Relative capacity gains of multiuser receivers over plain rate (EGC, $\lambda_l = \lambda_m = 0.75$).

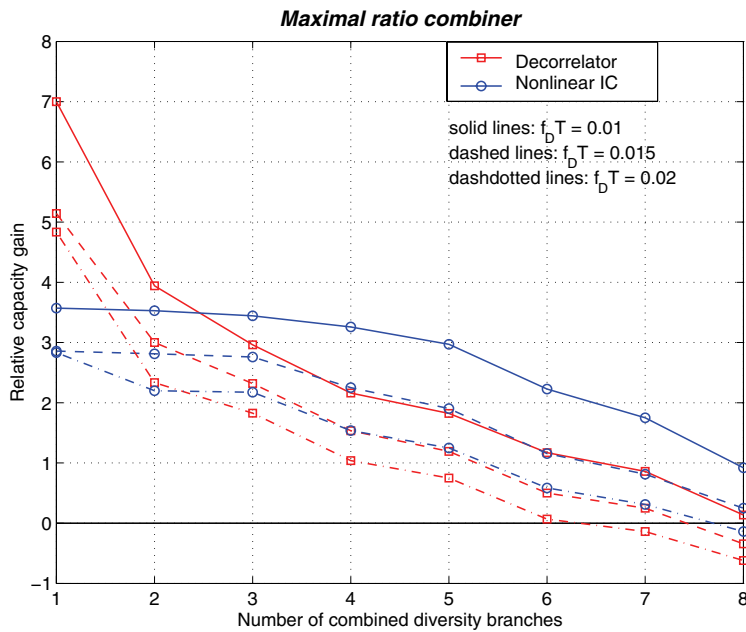


Fig. 42. Relative capacity gains of multiuser receivers over plain rate (MRC, $\lambda_l = \lambda_m = 0.75$).

4.7 Chapter summary

Wideband CDMA system effective capacity was studied in this chapter. Conventional rake receiver was used as a reference receiver. Linear and nonlinear multiuser receivers were utilized as enhancements over the reference structure. Imperfections in the EGC and MRC diversity schemes were derived and applied in the numerical capacity and sensitivity examples. Finally, capacities for the three receiver structures were compared in the same context.

Numerical results for the plain rake receiver showed that moderate capacities, in the order of 0–50 users/cell, can be achieved in the studied setups. The benefit of MRC over EGC became apparent at the steeper MIP. At the same time, sensitivity to imperfections was not very high for these simple reference receivers.

When the rake receiver was supplemented with the decorrelator, the capacity was shown to increase up to 250 users/cell in non-fading conditions. However, increasing the fading rate resulted in substantially reduced capacities due to escalating implementation losses. Thereupon, capacities diminished to the levels comparable to the reference receiver case. Capacity losses were also clearly demonstrated in the values of the sensitivity function. In the worst case, over 90% of the maximum capacity was lost.

The cancellation efficiency of the nonlinear interference cancellation receiver was illustrated to be sensitive to the modulation format and the operation point in the SNR region. This property was clearly seen in the best case MRC user capacity results ($f_D T = 0$, $L_0 = 8$), which were approximately threefold (600 versus 200) in comparison to corresponding EGC results. Elsewhere, MRC and EGC produced almost parallel results. The sensitivity increased quite steadily as a function of diversity order and normalized maximum Doppler shift.

The final comparative numerical capacity assessment enabled direct performance comparison between the studied schemes in relatively fast fading cases. The decorrelator could have 7-fold gain in effective user capacity over the plain rake receiver at $f_D T = 0.01$. The relative capacity gain for the nonlinear IC receiver remained below 4. But again, due to imperfections, the gains dropped significantly as a function of L_0 . For $L_0 = 7$ or 8 the capacities of multiuser receivers could even fall under the level obtainable by the plain rake receiver.

5 Ultra wideband spread spectrum framework

This chapter focuses on the evaluation of DS-UWB user capacity in lognormal fading multipath channels. The framework is introduced in Section 5.1. Section 5.2 describes the system model, including propagation channel modeling, derivation of link distance probability statistics for different cell topologies, and impact of UWB pulse waveform timing inaccuracies at the receiver. A procedure for outage probability analysis is explained in Section 5.3. A set of numerical results is presented in Section 5.4. Finally, a summary is provided in Section 5.5.

This chapter includes results of the research work performed towards the original publications [3, 6–8].

5.1 Introduction

Ultra wideband technology offers competitive solutions to high-rate short range wireless communication applications (e.g., home multimedia) [333]. Also, numerous practical applications for UWB are foreseen in the area of low data rate, low cost and complexity devices providing location and tracking capabilities [334] (e.g., wireless hospital applications). Inherent characteristics of UWB, such as high multipath resolution, low energy consumption, and peaceful coexistence with other radio frequency systems, are also favorable properties that will help the emergence of UWB. Impulse based UWB techniques can be seen as a special case of spread spectrum (SS) techniques. Both can utilize direct sequence (DS) and time hopping (TH) modulation. Matched filters and rake receivers can be used for energy collection from the multipath rich channel. This study assumes a generic DS-UWB system³ that requires some processing gain (integration of several pulses) to achieve the required quality of service.

System capacity can be measured by the number of users/devices/nodes that can be simultaneously supported within a predefined geographical area (cell). Capacity is therefore limited by the cochannel interference generated at the vicinity of the desired link receiver. Outage probability is a measure that links the aggregate interference to the

³ DS-UWB was shown in [235] to outperform TH-UWB in multipath fading and in the presence of interference.

quality of service. Channel amplitude is modeled to fluctuate according to a lognormal distribution. In the air-channel several signals overlap and sum up, which implies calculation of power sums of multiple lognormal signals. Unfortunately, there is no known closed-form solution for that case. However, several approximate methods have been presented in the literature, and been discussed in Section 2.5. Inherent frequency diversity of the extremely wide bandwidth UWB system helps to average out the signal fading. It is stated in [294] that the Fenton–Wilkinson approximation is fairly accurate at the tails of the distribution function (e.g., low outage probabilities) and with small standard deviations. For these reasons, and for simplicity, the Fenton–Wilkinson method is extensively applied in this study.

The main contributions of this segment of the framework can be summarized thus: 1) the adopted multipath channel model is described, 2) the dual-slope path loss model is incorporated, providing flexibility to model a wide range of physical environments (line-of-sight/non-line-of-sight) and wall penetration losses, 3) the spatial link distance distributions in circle-, square-, and hexagon-shaped cellular configurations are derived, simulated, and illustrated for centralized and distributed single and multiple cell configurations, and 4) the outage probability based user capacities are evaluated in these scenarios with various system parameter combinations.

5.2 System Description

5.2.1 Multipath channel model

Saleh and Valenzuela [239] have proposed a multicluster, exponentially decaying (per cluster), statistical channel model for indoor multipath propagation. Although the original model was proposed before UWB systems had gained real popularity, it provides a firm foundation for UWB channel modeling. The modified Saleh–Valenzuela models for UWB wireless personal area networks are described in [240, 335]. The UWB channel measurements analyzed in [335] indicate that a lognormal distribution fits better than a Rayleigh distribution for the multipath gain magnitudes. A lognormal fading model has been used, e.g., in [336] and [337]. The Nakagami distribution has also been reported to have high correlation with the measured data. Irrespective of the instantaneous short-term distribution, after some time averaging, the long-term distribution (shadowing) generally tends to be lognormal.

This thesis concentrates on system level studies and thus a simplified version of the modified Saleh–Valenzuela UWB model is employed. Adopting a tapped delay line model the channel impulse response can be written as

$$h(t) = \sum_{l=0}^{L-1} a_l \delta(t - \tau_l), \quad (124)$$

where l is the multipath delay index, L is the number of paths, a_l is the real-valued amplitude with lognormal distributed absolute value, and τ_l is the path delay of multipath

l . A generic exponentially decaying multipath intensity profile is assumed. MIP can also be referred as a power delay (or decay) profile (PDP). By using notation $E[a_l^2] = \alpha_l$, the mean power coefficients in a single cluster MIP with regular known tap delays can be expressed as

$$\overline{\alpha}_l = \overline{\alpha}_0 e^{-\lambda_l l} \quad l, \lambda_l \geq 0, \quad (125)$$

where λ_l is the temporal (delay) decay parameter. The number of multipath components and the decay exponent may be varied according to the propagation environments. Total power of the L -path MIP is normalized to unity as

$$\sum_{l=0}^{L-1} \overline{\alpha}_0 e^{-\lambda_l l} = 1. \quad (126)$$

5.2.2 Path loss model

The distance dependence of the average received power is taken into account in the path loss model. Dual-slope path loss model [338] is applied with the extension of the potential wall loss encountered at the breakpoint. The basic model in dB scale becomes

$$PL(d) = \begin{cases} 0, & 0 \leq d \leq 1 \\ c_0 \cdot \log_{10}(d), & 1 < d < d_{break} \\ c_1 + c_2 \cdot \log_{10}\left(\frac{d}{d_{break}}\right) + L_w, & d \geq d_{break}, \end{cases} \quad (127)$$

where distance d is in meters and c_0 , c_1 , and c_2 are constants that depend on the propagation environment. Distance d_{break} denotes the breakpoint of the path loss slopes and L_w accounts for the wall loss. Parameters c_0 and c_2 define the slopes at short and longer distances, respectively. It can be assumed that line-of-sight (LOS) conditions are valid at short link distances inside one room, when there are no walls or large objects obstructing the connection. Several UWB indoor channel measurement campaigns indicate that $c_0 = 17$ is a realistic value in this case [339]. Beyond the breakpoint the likelihood for non-line-of-sight (NLOS) conditions increases drastically (due to walls or other obstacles), leading to $c_2 = 35$, or even more. Constant $c_1 = c_0 \log_{10}(d_{break})$ guarantees continuity of the model at the breakpoint in the absence of wall loss.

Fig. 43 demonstrates graphically the effect of the dual-slope path loss model (127) when the breakpoint is altered. The wall loss is excluded in this illustration. It shows that up to 30 dB path loss can be experienced within the distance of 10 m with the chosen

parameter values. The wall loss would further increase the dynamic range of the attenuation.

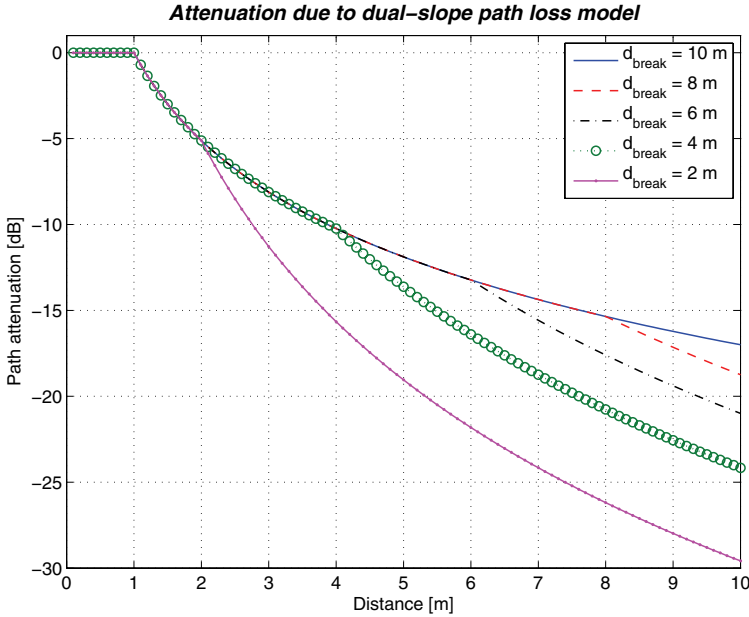


Fig. 43. The impact of path loss at variable breakpoint values without the wall loss.

5.2.3 Square cell network topologies and link distance distributions

5.2.3.1 Single cell scenarios

A rectangular cell shape is a reasonable assumption for indoor cells (rooms). A square-shaped cell is a special case of rectangular shape, and it has been chosen here for simplicity for further analysis. The methodology, however, can be extended to other regular or arbitrary cell shapes. Also, the following analysis is restricted to a two-dimensional plane, but can easily be generalized to a three-dimensional space. The size of the cell is dependent on the side of the square (denoted by a) that has been set to 5 m in the numerical examples. The desired and interfering users are assumed to be located within a square indoor cell (room) of the size 5 m \times 5 m. Four different spatial scenarios are considered. The first three are *centralized* (or master-slave, star topology) while the fourth is a *distributed* (or peer-to-peer, ad hoc) configuration. In the centralized model the fixed master node location is varied. *Scenario a* in Fig. 44 is optimized with respect to coverage by placing the master node at the center of the cell. Sub-optimum placements of the master node include the middle of the square side (*Scenario b*) and any corner of the

two sides (*Scenario c*). It is assumed that slave nodes are uniformly distributed over the cell area. In the distributed topology, (*Scenario d*), all nodes are treated equally (location uniformly distributed over the cell area) and they form peer-to-peer connections. A sample illustration of these topologies is depicted in Fig. 44. Solid lines correspond to the desired link and dashed lines represent three interfering links as an example.

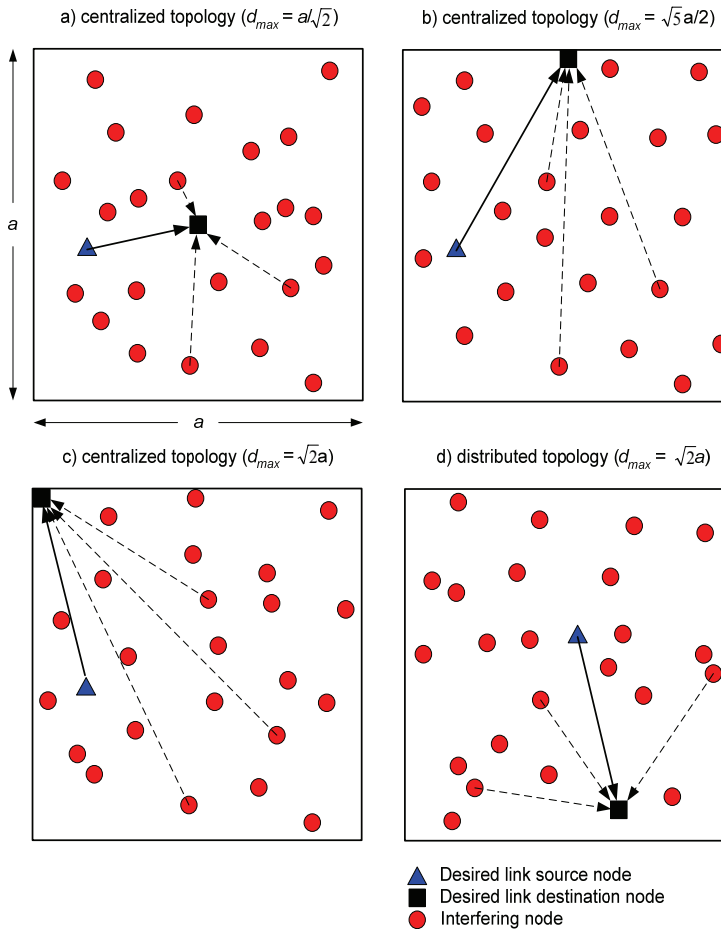


Fig. 44. Four different spatial topologies within a square cell.

Probability density functions for the link lengths have been solved in closed-form for certain regular cell topologies (e.g., [340–343] and references therein). For the centralized topology links, i.e., having the other end fixed and the other end randomly (uniformly) picked within a predefined regular area, the link distance PDF can also be derived in a straightforward manner. The generic link length PDF will be equal to arc length normalized by the sectional area [341]. With this rule, and basic school

trigonometry and geometry, it is possible to resolve distance PDFs within polygon and circular cell configurations. According to these principles, the PDF for the link distance in the centralized *Scenario a* of Fig. 44 can be expressed as

$$p_{s_a}^c(d) = \begin{cases} \frac{2\pi d}{a^2}, & 0 \leq d \leq \frac{a}{2} \\ \frac{2\pi d}{a^2} - \frac{8d}{a^2} \cos^{-1}\left(\frac{a}{2d}\right), & \frac{a}{2} < d \leq \frac{a}{\sqrt{2}}. \end{cases} \quad (128)$$

Subscript s in (128) refers to the square, sub-subscript denotes the scenario from Fig. 44 and superscript refers to the centralized topology.

The PDF for the link distance in *Scenario b* is slightly more complicated because it is composed of three segments. After some graphical geometry sketching and trigonometric calculations, the following formula was derived

$$p_{s_b}^c(d) = \begin{cases} \frac{\pi d}{a^2}, & 0 \leq d \leq \frac{a}{2} \\ \frac{\pi d}{a^2} - \frac{2d}{a^2} \cos^{-1}\left(\frac{a}{2d}\right), & \frac{a}{2} < d \leq a \\ \frac{2d}{a^2} \left[\sin^{-1}\left(\frac{a}{d}\right) - \cos^{-1}\left(\frac{a}{2d}\right) \right], & a < d \leq \frac{\sqrt{5}a}{2}. \end{cases} \quad (129)$$

In *Scenario c*, the probability density function closely resembles the one derived for *Scenario a*, and it becomes

$$p_{s_c}^c(d) = \begin{cases} \frac{\pi d}{2a^2}, & 0 \leq d \leq a \\ \frac{\pi d}{2a^2} - \frac{2d}{a^2} \cos^{-1}\left(\frac{a}{d}\right), & a < d \leq \sqrt{2}a. \end{cases} \quad (130)$$

Similarly, for the distributed peer-to-peer topology in a square cell, the corresponding PDF has been used in the random waypoint mobility model [342] and *square line picking* [343], and it is written as

$$p_{s_d}^d(d) = \begin{cases} \frac{2d}{a^2} \left(\frac{d^2}{a^2} - \frac{4d}{a} + \pi \right), & 0 \leq d \leq a \\ \frac{4d}{a^2} \left[\sin^{-1}\left(\frac{a}{d}\right) - \cos^{-1}\left(\frac{a}{d}\right) - 1 \right] + \frac{8d}{a^3} \sqrt{d^2 - a^2} - \frac{2d^3}{a^4}, & a < d \leq \sqrt{2}a. \end{cases} \quad (131)$$

The probability density functions (128)–(131) are plotted in Fig. 45 for $a = 5$ m. The validity of these equations has been cross-checked against PDFs extracted from the Monte Carlo simulations. In these simulations, 100000 randomly generated positions were generated for the square cell configurations of Fig. 44, from which the probability density histograms were created. It can be noted that the simulation results agree very well with the derived analytical expressions.

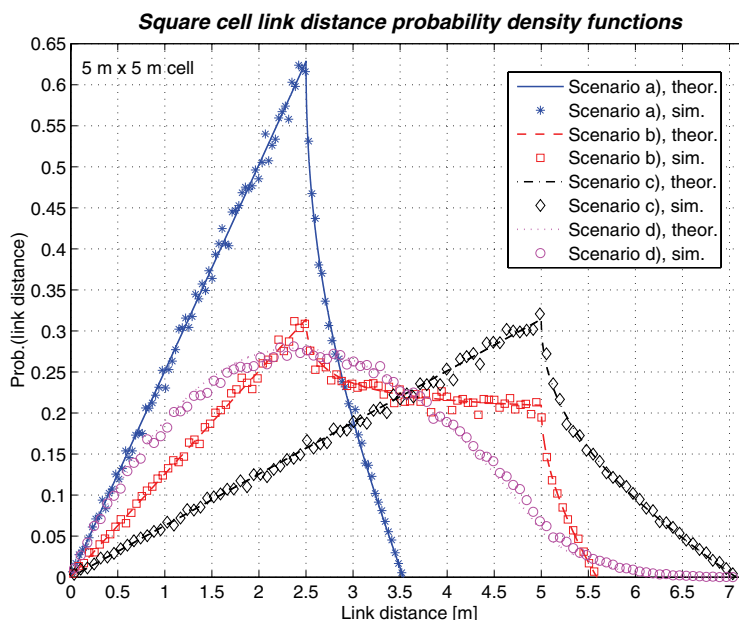


Fig. 45. Link distance PDFs for different topologies within a square cell.

These PDFs correspond to the arc length at each link distance divided by the covered area. As an example in the *Scenario a* the PDF of link distance grows linearly in proportion to the circumference of the circle until the breakpoint $a/2$ which is the longest distance allowing a circle to fit inside the square cell. The largest link distances can only be realized when the slave nodes are near some of the corners. The corresponding probability mass function (arc length) diminishes rapidly as a function of link length. The median link distances in *Scenario b* and *Scenario c* increase clearly in comparison to *Scenario a*. Drawbacks of these less favorable access point positions may be compensated with directional antennas.

The smooth shape of the distributed topology (*Scenario d*) distance PDF is evident because of the randomness in the generation of both ends of the link. The small tail of this distribution represents the longest link distances that can only be realized when both ends of the link are located at the vicinity of opposite corners.

Cumulative link distance distribution functions (CDF) can be calculated by integrating the PDFs over the whole range of possible link distances, e.g.,

$$P_{CDF}(d_{\min} \leq x \leq d_{\max}) = \int_{d_{\min}}^{d_{\max}} p_{PDF}(x) dx, \quad (132)$$

where $d_{\min} = 0$ in the case of (128)–(131).

Variations due to the different spatial configurations can now be quantified by taking percentile segments of the link distance CDF. This method helps to avoid the time-consuming Monte Carlo simulations in the further analysis that needs link distance dependent path losses. Even if the link distance PDF and CDF are generated through simulation the sufficient statistics can be extracted from only one simulation per scenario. Table 3 summarizes the link distances at each tenth of the cumulative distribution function in single square cell scenarios a) – d).

Table 3. Single square cell link distances according to CDF percentiles.

CDF [%]	Scenario a	Scenario b	Scenario c	Scenario d
10	0.89 m	1.26 m	1.78 m	0.97 m
20	1.26 m	1.78 m	2.53 m	1.44 m
30	1.55 m	2.18 m	3.10 m	1.83 m
40	1.78 m	2.51 m	3.58 m	2.20 m
50	1.99 m	2.91 m	4.00 m	2.56 m
60	2.19 m	3.34 m	4.38 m	2.93 m
70	2.36 m	2.79 m	4.72 m	3.31 m
80	2.52 m	4.25 m	5.05 m	3.75 m
90	2.67 m	4.73 m	5.58 m	4.29 m
100	3.54 m	5.58 m	7.07 m	7.07 m

The path loss model (127) in decibels scales the mean value of each desired and interfering lognormal signal component by

$$m_{PL} = m_0 - PL(d_{scen_{0j}}^x), \quad (133)$$

where m_0 is the mean of the initial signal and $d_{scen_{0j}}^x$ is the link distance whose subscript specifies the spatial scenario (c denotes the centralized and d denotes the distributed topology), sub-subscript indices 0 and $j \in [0, 1, 2, (1&2)]$ set the link ends to the respective cells and the superscript denotes the chosen link distance CDF percentile $x \in [10, 100]$ extracted from (132).

5.2.3.2 Multiple cell scenarios

Single cell analysis can be extended to larger networks, including multiple cells that will act as a source of intercell interference. In cellular systems, several surrounding layers may be required for a reliable estimate of the intercell interference statistics. However, due to the nature of the indoor environment and the very low transmission powers

assumed in this study, it is unlikely that significant cochannel interference would originate from distant cells. Signals will be even more isolated if there are thick walls between rooms. For these reasons, and because of complexity restrictions, only one surrounding layer of square cells is modeled as a potential origin of intercell interference. An illustrative example of the centralized multicell interference scenario is depicted in Fig. 46.

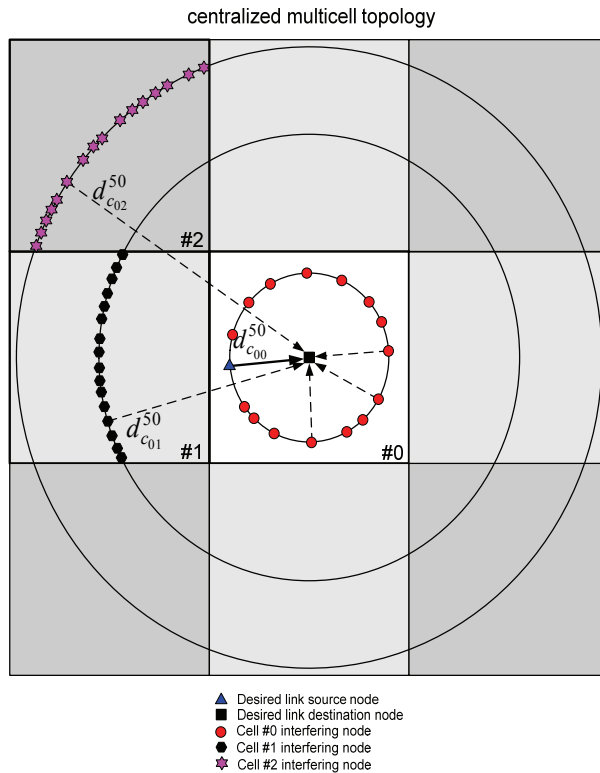


Fig. 46. Centralized multiple square cell configuration.

The central cell in Fig. 46, marked with #0, is the desired cell incorporating the link of interest and intracell interference links. The surrounding eight cells are divided into subgroups #1 (light grey) and #2 (dark grey), both including four square cells. Three circles with radii $d_{c_{00}}^{50}$, $d_{c_{01}}^{50}$, and $d_{c_{02}}^{50}$ represent median link distances⁴ between a destination node in cell #0 and source nodes in cells #0, #1, and #2, respectively. Due to geometrical symmetry only these three cells are adequate to fully characterize the link distance distributions of the scenario.

Interfering intercell link distance PDFs can be calculated the same way as in the single cell case. Restricting oneself only to the centralized topology of Fig. 46, the link distance

⁴ The circles drawn at median link distances divide the source cell in two equal area segments.

PDF between the fixed central node in cell #0 and a uniformly distributed node position in cell #1 can be derived as

$$p_{s_{01}}^c(d) = \begin{cases} \frac{2d}{a^2} \cos^{-1}\left(\frac{a}{2d}\right), & \frac{a}{2} \leq d \leq \frac{a}{\sqrt{2}} \\ \frac{2d}{a^2} \sin^{-1}\left(\frac{a}{2d}\right), & \frac{a}{\sqrt{2}} < d \leq \frac{3a}{2} \\ \frac{2d}{a^2} \left[\sin^{-1}\left(\frac{a}{2d}\right) - \cos^{-1}\left(\frac{3a}{2d}\right) \right], & \frac{3a}{2} < d \leq \frac{\sqrt{10}a}{2}. \end{cases} \quad (134)$$

Similarly, between the fixed central node in cell #0 and a random node position in cell #2, the link distances the PDF becomes

$$p_{s_{02}}^c(d) = \begin{cases} \frac{\pi d}{2a^2} - \frac{2d}{a^2} \sin^{-1}\left(\frac{a}{2d}\right), & \frac{a}{\sqrt{2}} \leq d \leq \frac{\sqrt{10}a}{2} \\ \frac{\pi d}{2a^2} - \frac{2d}{a^2} \cos^{-1}\left(\frac{3a}{2d}\right), & \frac{\sqrt{10}a}{2} < d \leq \frac{3a}{\sqrt{2}}. \end{cases} \quad (135)$$

Finally, without division into subgroups, the link distance PDF between the central node in cell #0 and a randomly placed node within the combined area of cells #1 and #2 is formulated as

$$p_{s_{0(1\&2)}}^c(d) = \begin{cases} \frac{d}{a^2} \cos^{-1}\left(\frac{a}{2d}\right), & \frac{a}{2} \leq d \leq \frac{a}{\sqrt{2}} \\ \frac{\pi d}{4a^2}, & \frac{a}{\sqrt{2}} < d \leq \frac{3a}{2} \\ \frac{\pi d}{4a^2} - \frac{d}{a^2} \cos^{-1}\left(\frac{3a}{2d}\right), & \frac{3a}{2} < d \leq \frac{3a}{\sqrt{2}}. \end{cases} \quad (136)$$

These analytical PDF expressions are compared to the simulated distributions in Fig. 47. Generally, a good match between theoretical and simulation results is shown. Only the middle segment of link 01 simulation has not been fully averaged out with the chosen number of samples. It is worth noting that the shapes of link distance PDFs for links 01 and 02 differ drastically. However, it is easy to understand these differences intuitively by visually examining the cell geometry and the way the arc length changes along the distance. The link distance 0(1&2) PDF falls naturally between the other curves as expected.

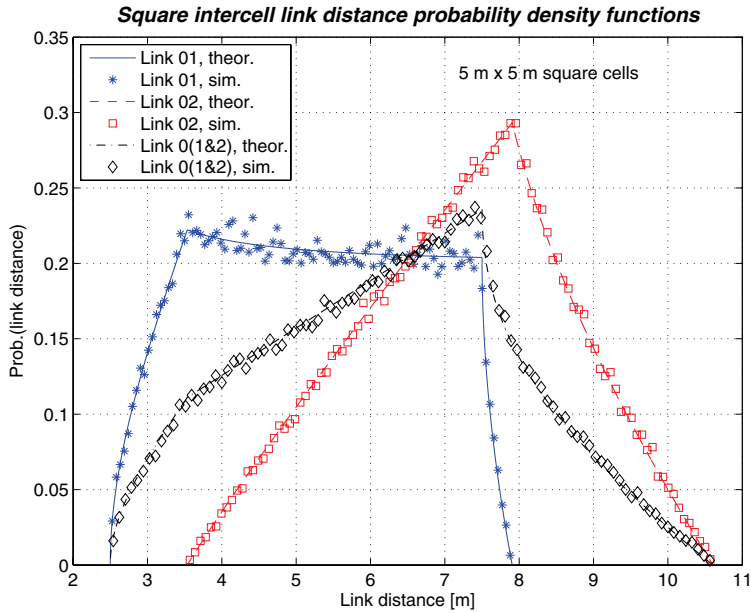


Fig. 47. Intercell link distance PDFs for centralized square cell topologies.

For the distributed topology the intercell link distance statistics have not been derived. Instead, statistics based on simulations have been extracted. An example of simulated link distance CDFs according to (132) and topologies in Figs. 44 and 46 is depicted graphically in Fig. 48 and numerically in Table 4. It can be seen that, in general, the centralized scenario CDFs are steeper than distributed scenario counterparts because of the more limited range in distances. As a result, the main differences between centralized and distributed topologies are at the low and high regions of CDFs. Around median link distances there are only moderate deviations between them.

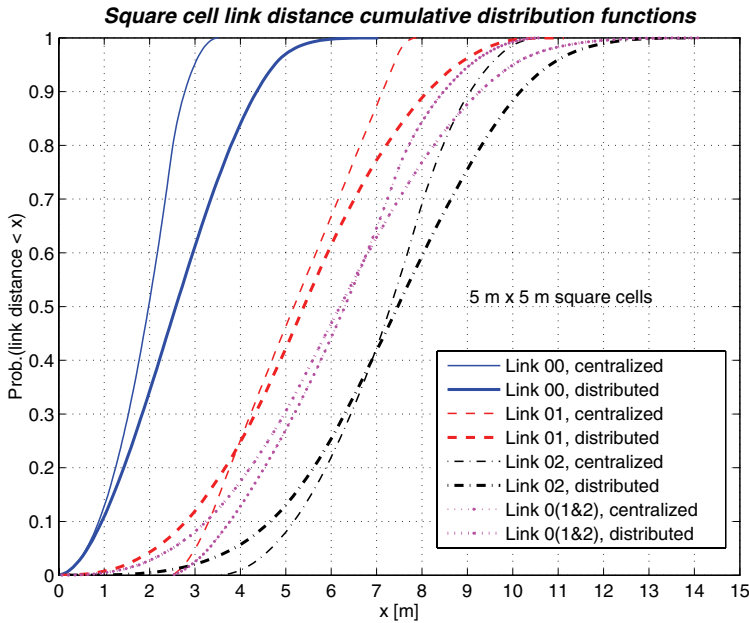


Fig. 48. Simulated link distance CDFs for different square cell topologies.

Table 4. Square intercell link distances according to CDF percentiles.

CDF [%]	Centralized topology			Distributed topology		
	Link 01	Link 0(1&2)	Link 02	Link 01	Link 0(1&2)	Link 02
10	3.33 m	3.78 m	5.19 m	2.88 m	3.55 m	4.73 m
20	3.79 m	4.55 m	5.91 m	3.73 m	4.56 m	5.64 m
30	4.25 m	5.20 m	6.45 m	4.37 m	5.30 m	6.28 m
40	4.72 m	5.78 m	6.92 m	4.91 m	5.93 m	6.85 m
50	5.21 m	6.31 m	7.33 m	5.41 m	6.56 m	7.39 m
60	5.69 m	6.79 m	7.70 m	5.92 m	7.18 m	7.93 m
70	6.18 m	7.25 m	8.05 m	6.49 m	7.84 m	8.50 m
80	6.66 m	7.72 m	8.48 m	7.17 m	8.59 m	9.14 m
90	7.15 m	8.48 m	9.07 m	8.06 m	9.56 m	9.95 m
100	7.91 m	10.61 m	10.61 m	11.18 m	14.14 m	14.14 m

5.2.4 Comparison of link distance statistics in different cellular models

To study the effect of cell shape to link distance statistics two additional widely used non-overlapping cell models are introduced, namely circular and hexagonal. Fig. 49 depicts the cellular structures that have been chosen for closer inspection.

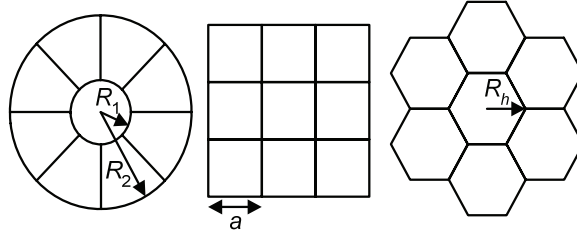


Fig. 49. Three cellular configurations selected for the comparison.

5.2.4.1 Single cell comparisons

To ensure a fair comparison, the areas of each cell type in Fig. 49 are normalized. Therefore, the requirement $A_c = \pi R_1^2 \Leftrightarrow A_s = a^2 \Leftrightarrow A_h = \frac{3\sqrt{3}}{2} R_h^2$ has to be satisfied. Taking the square a as a reference metric, relations $R_1 = a/\sqrt{\pi} \approx 0.564a$ and $R_h = \sqrt{2a}/\sqrt{3\sqrt{3}} \approx 0.620a$ can be derived.

The simplest case to analyze is a single circular cell. Assuming the other link end (master node) is located at the center of the cell, link distance PDF from the center to spatially uniformly distributed link end can be expressed in closed-form as

$$p_c^c(d) = 2d/R_1^2, \quad 0 \leq d \leq R_1, \quad (137)$$

where d is the link distance and R_1 is the cell radius.

Within the centralized hexagonal cell, the link distance PDF is of the form

$$p_h^c(d) = \begin{cases} \frac{4\pi d}{3\sqrt{3}R_h^2}, & 0 \leq d \leq \frac{\sqrt{3}R_h}{2} \\ \frac{8d \left[\sin^{-1} \left(\frac{\sqrt{3}R_h}{2d} - \frac{\pi}{3} \right) \right]}{\sqrt{3}R_h^2}, & \frac{\sqrt{3}R_h}{2} < d \leq R_h. \end{cases} \quad (138)$$

There are also some closed-form expressions for distributed single cell topologies in the literature. For example, the online reference [344] discusses *disc line picking* that provides a link distance PDF solution for a circular cell as

$$p_c^d(d) = \frac{4d}{\pi R_1^2} \cos^{-1} \left(\frac{d}{2R_1} \right) - \frac{2d^2}{\pi R_1^3} \sqrt{1 - \frac{d^2}{4R_1^2}}, \quad 0 \leq d \leq 2R_1. \quad (139)$$

Fig. 50 shows theoretical and simulated link distance probability density functions in a single circle, square, and hexagon cell with both the centralized and distributed node strategy. The simulations are based on 100000 randomly generated links in the area of interest. Distance statistics are collected into 100 histogram bins from which the required distributions are obtained. It can be noted that the effect of cell shape to the PDF curves is minor. On the other hand, the difference between master-slave and peer-to-peer configurations is evident. Simulated and theoretical results are in good agreement.

Fig. 51 depicts the corresponding cumulative distribution functions (CDFs) that have been generated by integrating simulated PDFs over the whole range of link distances. Percentiles of link distance CDFs will be used in the numerical examples. Clearly, the impact of cell shape is almost negligible. For example, up to the 80th percentile contours in centralized configurations the curves are practically identical for all cell models.

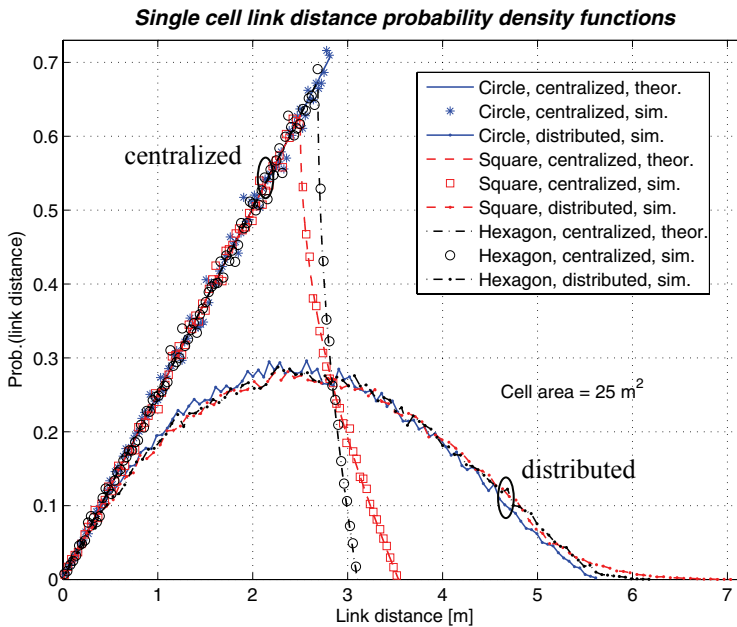


Fig. 50. Intracell link distance probability density functions.

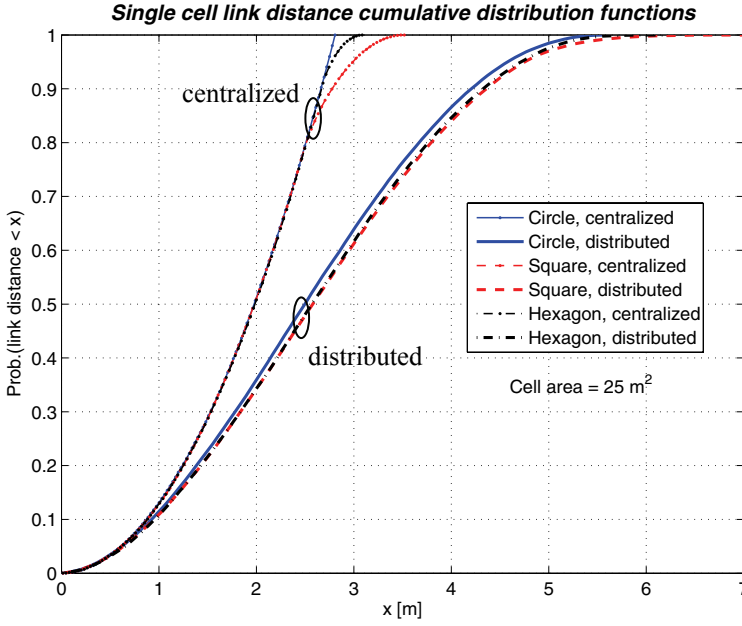


Fig. 51. Intracell link distance cumulative distribution functions.

5.2.4.2 Multiple cell comparisons

Accounting for the total area of cells depicted in Fig. 49 the normalization requires $9A_c = 9A_s = 7A_h$. Therefore, $9a^2 = \pi R_2^2$, resulting in $R_2 = 3a/\sqrt{\pi} \approx 1.693a$. It can be noted that the hexagonal model includes two cells less than the other models. This can be compensated in the total area by scaling the hexagonal cell radius as $R_h = \sqrt{6}a/\sqrt{7\sqrt{3}} \approx 0.703a$.

The link distance PDF between the origo and random, uniformly distributed location in the disc area limited by the circles of radii R_1 and R_2 , is expressed by

$$p_{cc}^c(d) = 2d/(R_2^2 - R_1^2), \quad R_1 < d \leq R_2, \quad (140)$$

where the double subscript cc is used to distinguish single cell (intracell) links from the multiple cell (intercell) links.

Finally, in the case of hexagonal centralized topology, the link distance PDF of the middle cell center and any random point in the surrounding cell layer will be defined. The resulting equation is determined in four pieces as

$$p_{hh}^c(d) = \begin{cases} \frac{4d}{3\sqrt{3}R_h^2} \cos^{-1}\left(\frac{\sqrt{3}R_h}{2d}\right), & \frac{\sqrt{3}R_h}{2} \leq d \leq R_h \\ \frac{2\pi d}{9\sqrt{3}R_h^2}, & R_h < d \leq 2R_h \\ \frac{4d \sin^{-1}\left(\frac{\sqrt{3}R_h}{d}\right) - \frac{2\pi d}{3}}{3\sqrt{3}R_h^2}, & 2R_h < d \leq \frac{3\sqrt{3}R_h}{2} \\ \frac{4d \sin^{-1}\left(\frac{\sqrt{3}R_h}{d}\right) - \frac{2\pi d}{3} - 4d \cos^{-1}\left(\frac{3\sqrt{3}R_h}{2d}\right)}{3\sqrt{3}R_h^2}, & \frac{3\sqrt{3}R_h}{2} < d \leq \sqrt{7}R_h. \end{cases} \quad (141)$$

Fig. 52 shows the link distance PDF statistics and Fig. 53 the link distance CDF statistics for intercell links in multiple cell scenarios. Slightly more variation is seen in the PDFs and CDFs, which is partly due to the wider range of distances. Still, the analytical and simulation results overlap well. In link distance CDFs, the difference of cell shapes is again largest at the high-end of the distributions.

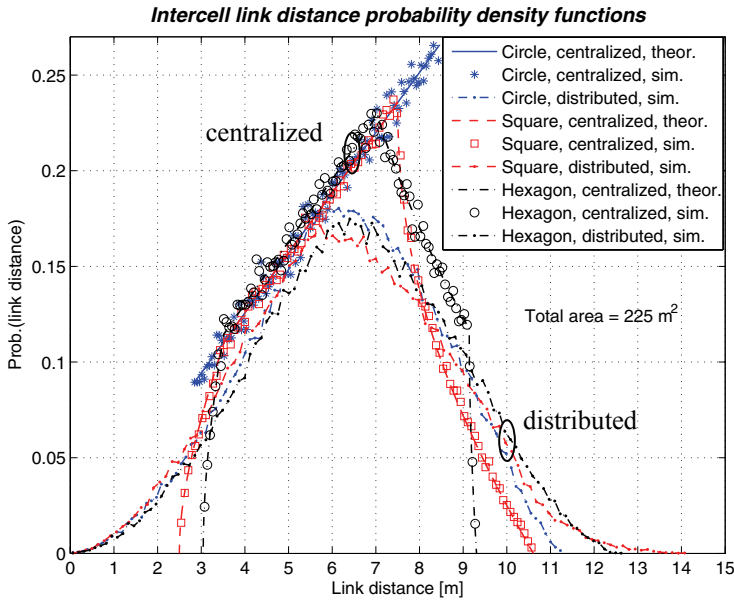


Fig. 52. Intercell link distance probability density functions.

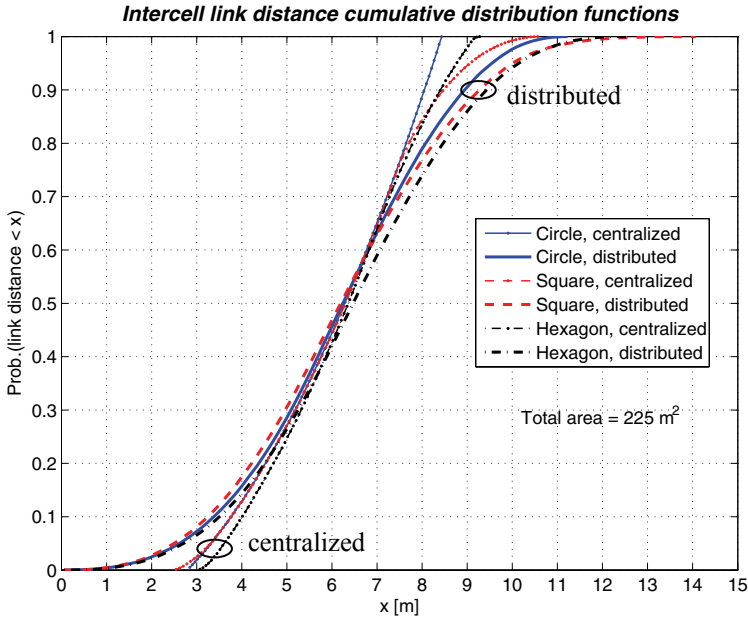


Fig. 53. Intercell link distance cumulative distribution functions.

5.2.5 UWB pulse waveforms and impact of timing errors

A Gaussian monocycle is one of the most commonly assumed pulse waveforms in impulse radio (IR) based UWB systems. The basic (zeroth derivative) zero-mean pulse can be defined as [345]

$$w_{G_0}(t) = \frac{A}{\sqrt{2\pi}\sigma} \exp\left(-\frac{t^2}{2\sigma^2}\right), \quad (142)$$

where σ is the standard deviation of the Gaussian distribution and A is a generic amplitude scaling constant. Derivative waveforms can be generated by direct differentiation of (142) with respect to time as

$$w_{G_n}(t) = \frac{d^n}{dt^n} w_{G_0}(t), \quad (143)$$

where n indicates the order of the derivative. Higher n th order derivations can also be defined recursively from the two lower order ($n - 2$) and ($n - 1$) waveforms as

$$w_{G_n}(t) = -\frac{n-1}{\sigma^2} w_{G_{n-2}}(t) - \frac{t}{\sigma^2} w_{G_{n-1}}(t). \quad (144)$$

According to the studies in [345], the 5th time derivative of (142), i.e., $w_{G_5}(t)$, is the lowest order waveform satisfying the Federal Communications Commission (FCC) indoor spectral emission mask requirements. Passing signal through an antenna can also be approximated as a first-order differentiation of the pulse waveform [346]. Therefore, the generated waveform at the transmitter should be at least the 4th derivative of (142). The waveform seen at the receiver antenna output would then be the 6th derivative of (142), yielding

$$w_{G_6}(t) = A \left(\frac{t^6/\sigma^6 - 15t^4/\sigma^4 + 45t^2/\sigma^2 - 15}{\sqrt{2\pi}\sigma^7} \right) \exp\left(-\frac{t^2}{2\sigma^2}\right). \quad (145)$$

To ensure that most of the pulse energy will be captured, the pulse duration is set to $T_p = 10\sigma$. Fig. 54 shows normalized timing offset versus squared autocorrelation function at the output of the correlation receiver for the basic Gaussian pulse (142) and its 6 first derivatives. Clearly, the susceptibility to timing errors increases as a function of derivation order as the main correlation lobe becomes narrower and narrower. If the time axis would be plotted further, the sidelobes of high-order derivative waveforms would appear and cause periodic fluctuation in squared autocorrelation magnitudes.

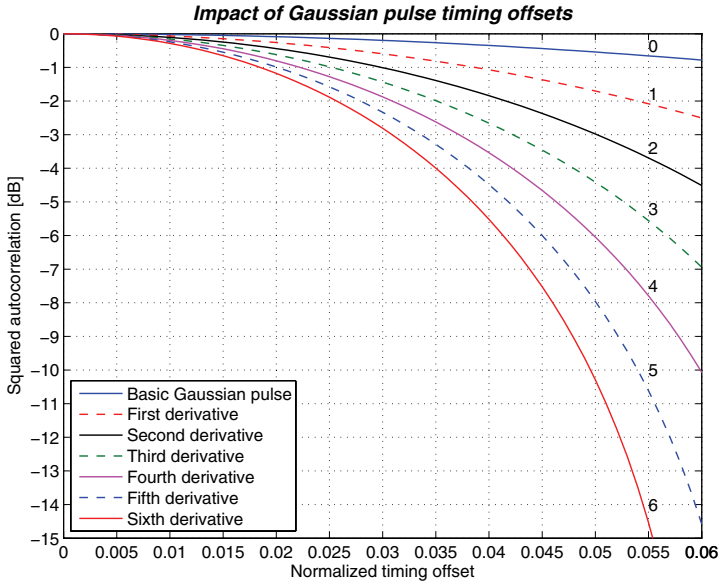


Fig. 54. Effect of timing errors of basic Gaussian pulse waveform and their derivatives.

The impact of timing errors (delay estimation, jitter) of the pulse waveforms in each receiver rake finger will be included by the following equations

$$\overline{\alpha}_l(\varepsilon_t) = R^2(\varepsilon_t) \overline{\alpha}_l, \quad (146)$$

$$\sigma_l^2(\varepsilon_t) = \sigma_l^2 + (1 - R^2(\varepsilon_t)) \frac{\overline{\alpha}_0}{\overline{\alpha}_l}, \quad (147)$$

where $R^2(\varepsilon_t)$ is the squared correlation function of the pulse waveform (145) with the normalized timing error $\varepsilon_t = t/T_p$. Variance in (147) depends on the severity of shadowing σ_l^2 per path, pulse autocorrelation, and power ratio of multipath components. Error variance, i.e., the latter term in (147), is assumed to be inversely proportional to the delay tracking loop signal-to-noise ratio.

5.3 Outage probability analysis

User capacity can be defined as the maximum number of admissible active cochannel interferers satisfying a predefined outage criterion. The conditional outage probability is expressed as

$$P_{out}(I|n, u, L, L_0) = P\left(\frac{S(L_0)}{[I_{INTRA}(n) + I_{INTER}(u)]I_{MPI}(L) + I_{IPI}(L_0(L-1))} < \left(\frac{S}{I}\right)_{tar}\right), \quad (148)$$

where $S(L_0)$ is the desired signal power combined by L_0 rake fingers, and $(S/I)_{tar}$ is the target link quality requirement. Cochannel interference sources are n active multiaccess users in the desired cell (intracell interference I_{INTRA}) denoted by symbol n and u users in the neighboring cells (intercell interference I_{INTER}). All these signals spread over multiple propagation paths (I_{MPI}). The interpaths of the desired user link (I_{IPI}) also produce interference that depends on the number of rake fingers deployed at the receiver. The system is assumed to be interference limited, i.e., the thermal noise power is significantly lower than the cochannel interference power, and therefore omitted.

The overall outage probability can be calculated by unconditioning (148) with the probability density function of n intracell interferers being active while keeping u , L , and L_0 fixed. Therefore, we can write

$$P_{out}(I) = \sum_{n=1}^N P_{out}(I|n, u, L, L_0) P_n(n), \quad (149)$$

where $P_{out}(I)$ denotes the outage probability that accounts for the interference probability density function of n active interferers $P_n(n)$. Assuming a binomial PDF [191] for $P_n(n)$, it becomes

$$P_n(n) = \binom{N}{n} P_{act}^n (1 - P_{act})^{N-n}, \quad (150)$$

where N is the maximum number of cochannel interferers and P_{act} is the activity factor of these interfering sources.

In any spread spectrum system there is a simple relation between channel signal-to-interference ratio and baseband bit energy-to-interference power spectral density. It can be formulated as

$$\frac{S}{I} = \frac{R_b E_b}{R_c I_0} = \frac{E_b/I_0}{PG}, \quad (151)$$

where $PG = R_c/R_b$ is the processing gain, i.e., a ratio of the spread chip rate R_c and the bit rate R_b . The required E_b/I_0 values depend on various link level parameters (e.g., data rate, modulation, bit error rate), and can be obtained via simulations. However, this study simply focuses on the generic S/I target.

Fig. 55 shows a block diagram for the S/I and outage evaluation procedure. The desired signal with power S travels along the upper branch. It will be attenuated by the distance dependent path loss (block PL) and finally the strongest L_0 fingers are combined in the selective rake receiver ($L_0 \leq L$) [241]. The lower branches represent interference that is a sum of N desired cell multiple access signals through L -path channels, U neighboring cell multiple access signals through L -path channels and interpath interference of the desired user through $L_0(L - 1)$ paths. The last block in the chain entitled unconditioning refers to calculus shown in (149).

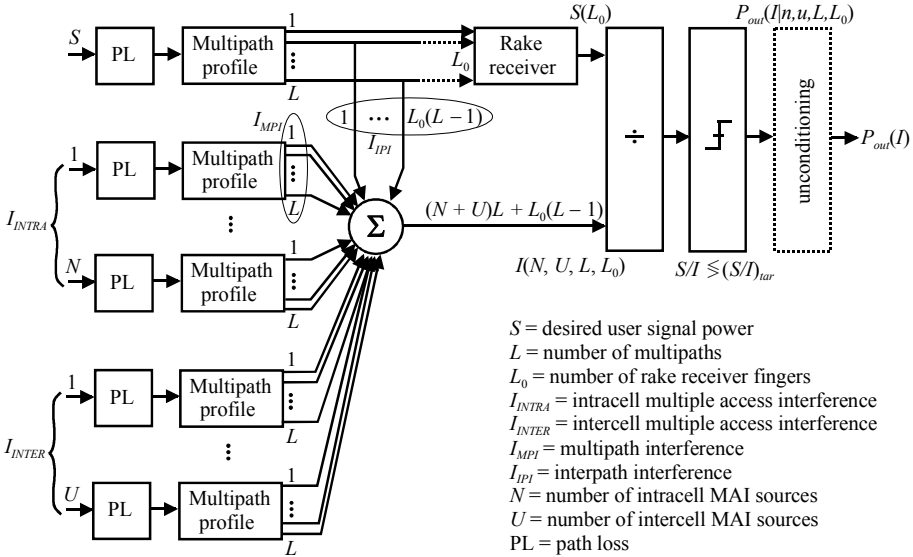


Fig. 55. System model for signal-to-interference ratio and outage calculation.

Equation (148) depends on the mean and variance of the lognormal sum distribution. By further conditioning the outage probability on n intracell interferers, u intercell interferers, and L_0 rake fingers, a slightly modified expression from [294] can be derived as

$$P_{out}(I|n, u, L, L_0) = 1 - Q \left(\frac{\ln(S/I)_{tar} - m_d(L_0) + m_z(n, u, L, L_0)}{\sqrt{\sigma_d^2(L_0) + \sigma_z^2(n, u, L, L_0) - 2r_{dz}\sigma_d(L_0)\sigma_z(n, u, L, L_0)}} \right), \quad (152)$$

where $Q(x) = \frac{1}{\sqrt{2\pi}} \int_x^\infty e^{-v^2/2} dv$ is a zero-mean, unit variance Gaussian complementary distribution function [191], v is a dummy integration variable, $m_d(L_0)$ is the area mean desired signal power at the output of L_0 -finger rake, $m_z(n, u, L, L_0)$ is the area mean total cochannel interference power, $\sigma_d(L_0)$ is the standard deviation of the desired signal at the output of L_0 -finger rake, $\sigma_z(n, u, L, L_0)$ is the standard deviation of the total cochannel interference, and r_{dz} is the correlation coefficient of the desired signal and joint interference.

The overall cochannel interference mean and standard deviation in (152) can be calculated through successive use of the lognormal sum approximation. Composite contributions in the total sum distribution can be divided into intracell, intercell, and desired link interpath interference components as

$$m_z(n, u, L, L_0) = \sum_n m_{INTRA}(L) + \sum_u m_{INTER}(L) + m_{IPI}(L_0(L-1)), \quad (153)$$

$$\sigma_z(n, u, L, L_0) = \sum_n \sigma_{INTRA}(L) + \sum_u \sigma_{INTER}(L) + \sigma_{IPI}(L_0(L-1)). \quad (154)$$

Aggregate interference is calculated with respect to indices $n = 1, \dots, N$, and $u = 1, \dots, U$, i.e., the number of active intra- and intercell interference sources. All multipath profiles include L independent components. The number of interpath interference components depends on the diversity order L_0 in the rake combiner in addition to the number of multipaths. Fig. 56 represents a flow chart on the mean and standard deviation of the interpath interference accumulation (last summands in (153) and (154)), depending on the number of rake fingers.

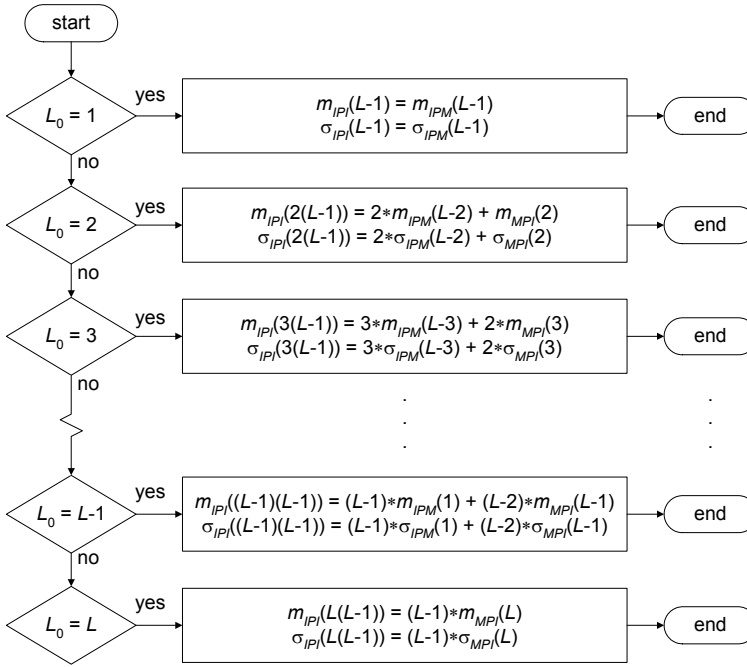


Fig. 56. Flow chart of the interpath interference statistics calculation.

The lognormal sum statistics m_{MPI} and σ_{MPI} are calculated from the MIP presented in (125). If the power coefficients of the exponential multipath profile are collected into vector $\vec{\alpha} = [\alpha_0 \alpha_1 \dots \alpha_{L-2} \alpha_{L-1}]$ the argument explains how many strongest paths are summed up. For statistics m_{IPM} and σ_{IPM} the process is otherwise similar with the exception that the path gain vector is reversed as $\vec{\alpha} = [\alpha_{L-1} \alpha_{L-2} \dots \alpha_1 \alpha_0]$. Now the argument refers to the number of weakest paths contributing to the sum.

5.4 Numerical examples

A generic spread spectrum DS-UWB system is assumed, targeted for $S/I = -17$ dB. The basic assumption is that all signal components are uncorrelated. The selective rake receiver of the desired user combines L_0 strongest paths as non-coherent⁵ lognormal power sum. Path loss breakpoints and wall losses are set for the desired cell links as $d_{break} = d_{d_{00}}^{100}$ that ensures the wall loss $L_w = 0$ dB inside the desired cell. For the intercell interference links, the corresponding parameters are $d_{break} = d_{d_{0(1\&2)}}^{10}$ and $L_w = 10$ dB. Table 5 includes more parameters and variables chosen for the forthcoming numerical results.

⁵ Assuming simple, low-complexity energy detection based devices.

Bold-faced numbers are the default values. The exceptions and variations in these will be specifically pointed out in the upcoming illustrations.

Table 5. Key parameters in the numerical examples.

Number of multipaths L	24 ⁶
Number of rake fingers L_0	1, ..., 9 , ..., 24
MIP decay parameter λ_i	1/4.3 \approx 0.23256
$m_d(1) = m_z(1)$ [dB]	-6.8135
$\sigma_d(1) = \sigma_z(1)$ [dB]	2.4, 2.9, 3.4 , 3.9, 4.4
S/I target $(S/I)_{tar}$ [dB]	-20, -19, -18, -17 , -16, -15, -14
Link distance CDF [%]	10, ..., 50 , ..., 100
Interferer activity factor P_{act}	0.1, ..., 1
Path loss constant c_0	17
Path loss constant c_2	35
Max. number of intracell interferers N	23
Max. number of intercell interferers U	8 \times 24
Normalized timing error ε_t [t/T_p]	0 , ..., 0.045
Multipath correlation r_{mpi}	0 , 0.25, 0.5, 0.75, 0.99

Figs. 57 and 58 demonstrate the dependence of conditional outage probability on the number of rake fingers at the receiver. In Fig. 57, the centralized single cell topology is chosen (see Fig. 44a). The desired link and intracell interference link distances are set to $d_{c_{00}}^{50} \approx 1.99$ m. It can be seen that the optimum number of fingers is relatively insensitive to the varying load in the cell, staying between 7 and 10. Fig. 58 shows quite different system setting for a heavily loaded distributed multiple cell geometry. In this case, all the desired cell link distances are fixed to $d_{d_{00}}^{50} \approx 2.56$ m. Link lengths from the surrounding cells are set to $d_{d_{0(1\&2)}}^{10} \approx 3.55$ m. The impact of all 192 intercell nodes is accounted for. The optimal selection of rake fingers remains tightly between 10 and 11. These quite different network configurations and outage levels produce very similar outcome. As a conclusion of both cases, it can be stated that only moderate complexity (approximately 9 rake fingers) is needed for optimal noncoherent combining even in the multipath rich channel. Therefore, the number of rake fingers is fixed to 9 in most of the remaining numerical examples.

⁶ E.g., modified Saleh-Valenzuela model CM 1 [240, 335] has 24 significant multipaths.

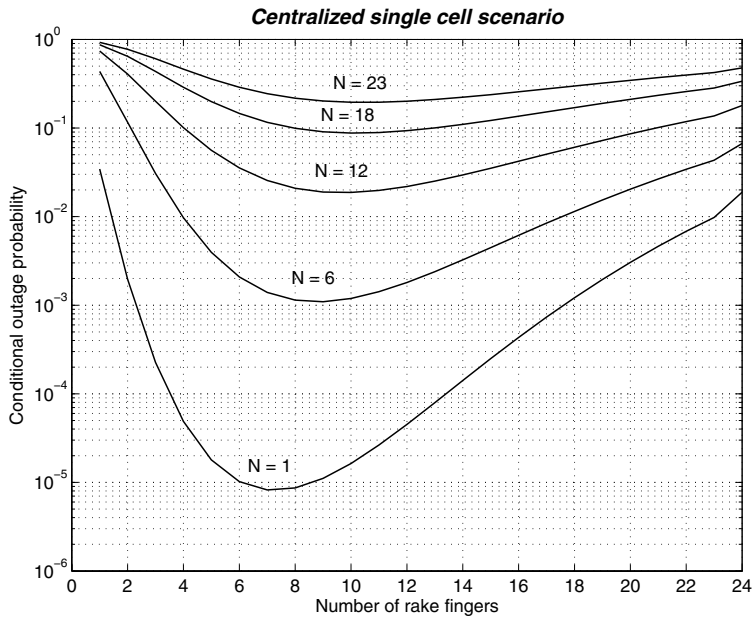


Fig. 57. Number of rake fingers vs. conditional outage probability in a centralized single cell configuration.

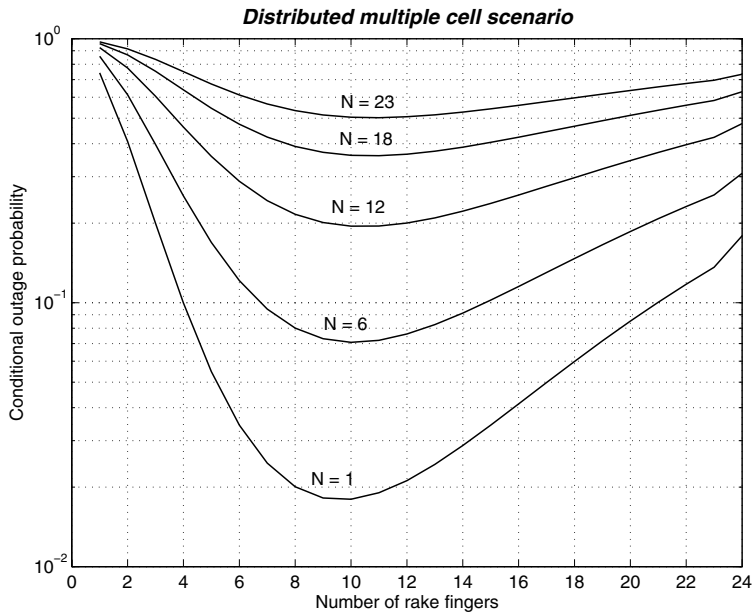


Fig. 58. Number of rake fingers vs. conditional outage probability in a distributed multiple cell configuration ($U = 192$).

Fig. 59 depicts the differences of three centralized single cell geometries a) – c) from Fig. 44 while the desired link distance CDF percentile varies between 10% and 90% contours and the interfering link distances are maintained at their respective spatial median (i.e., 50%) values. Nine rake fingers are employed at the receiver. Some observations can be made from these curves. First, the variation in the conditional outage performance is largest for *Scenario b* and smallest for *Scenario a*, as expected. Second, *Scenario a* and *Scenario c* provide practically identical results at intermediate desired link lengths. Third, clear disparities in PDF statistics shown in Fig. 45 do not fully show up in outage based evaluation, because it is based on relative measure between the desired and interfering signals instead of absolute one.

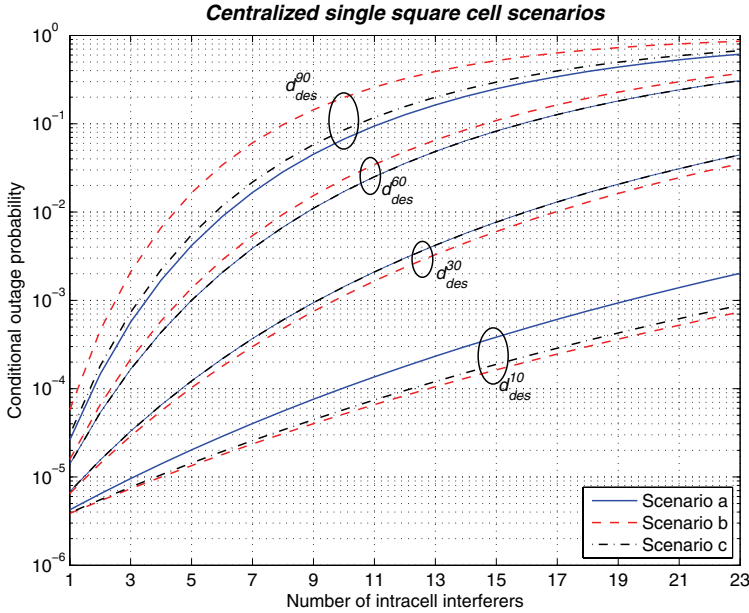


Fig. 59. Comparison of conditional outage probabilities in three single cell scenarios.

Fig. 60 depicts the impact of intercell load to conditional outage probability at desired link distances $d_{des}^{10} = d_{c_{00}}^{10} \approx 0.89$ m, $d_{des}^{50} = d_{c_{00}}^{50} \approx 1.99$ m, and $d_{des}^{90} = d_{c_{00}}^{90} \approx 2.68$ m, while the intracell interferer link distances are maintained at $d_{intra}^{50} \approx 1.99$ m. On the other hand, the effect of intercell interference is emphasized by locating the surrounding cell layer nodes near the center cell border at link distances $d_{inter}^{10} \approx 3.78$ m. It can be noted that as the load in the desired cell increases, the contribution of interference from other cells becomes less and less significant. At light intracell loading, however, the aggregate intercell interference affects substantially the desired link conditional outage probability. Naturally, the geometry of the link of interest plays a key role in the observed outage level so that the intercell interference effect is most profound in the worst-case scenario from the desired user point of view (i.e., at long distances).

Fig. 61 shows the impact of the desired link distance CDF and load variability to the conditional outage probability in a centralized multiple cell scenario. A reference plane is plotted at the conditional outage probability of 10^{-2} in order to better illustrate the cross-section and shape of the surface. For comparison, a similar graphical illustration for a distributed configuration is represented in Fig. 62. Overall, there are no significant deviations between these figures. On closer examination we notice that at the tails of the cumulative distributions the distributed topology bears more dynamics. As a result, the outage probability gets higher using upper percentiles of distance CDF and slightly lower at the shortest distance contours.

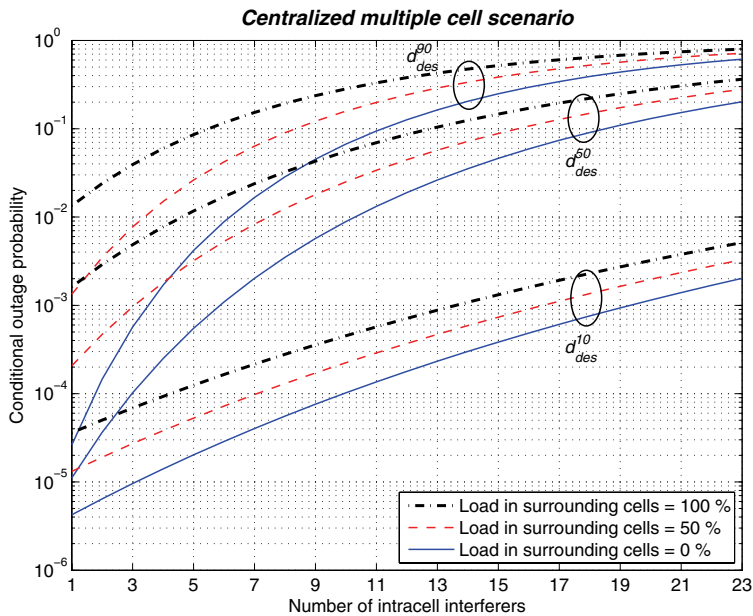


Fig. 60. Impact of the intercell interference to the conditional outage probability.

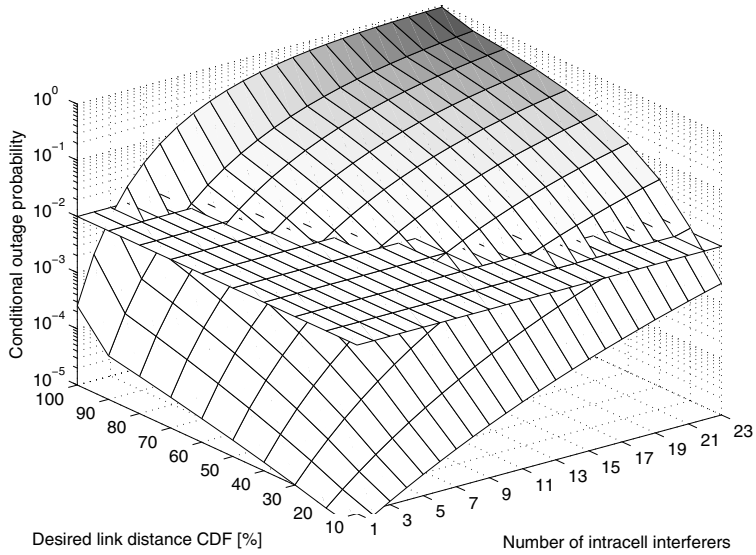
Centralized multiple cell scenario

Fig. 61. Impact of the desired link distance CDF to the conditional outage probability (centralized multiple cell configuration, $U = 96$).

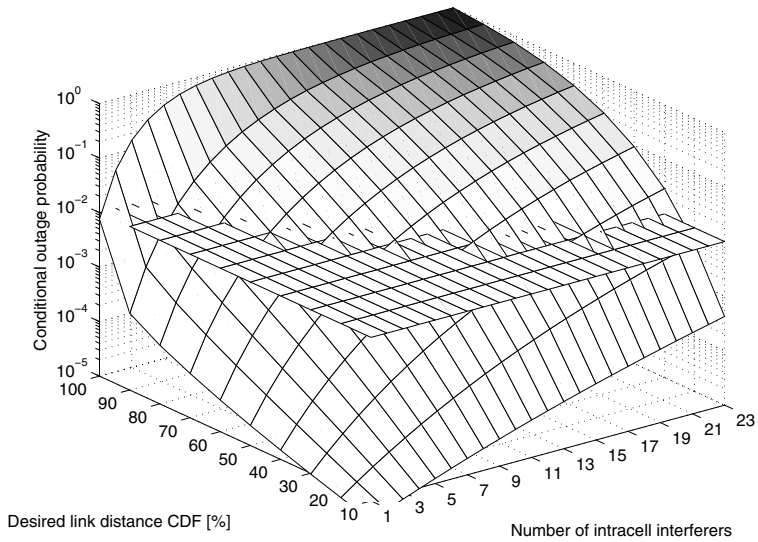
Distributed multiple cell scenario

Fig. 62. Impact of the desired link distance CDF to the conditional outage probability (distributed multiple cell configuration, $U = 96$).

Fig. 63 and 64 show how the outage probability (according to (148) and (149)) behaves as a function of desired link distance CDF percentile and intracell interference activity factor in centralized and distributed configurations. Nine rake fingers are deployed according to the previously shown results. Intercell interference sums up from the 8×12 active links (50% load). Intracell interference link distances are set to $d_{c_{00}}^{50} \approx 1.99$ m. Intercell interference link distances are $d_{c_{01}}^{50} \approx 5.21$ m and $d_{c_{02}}^{50} \approx 7.33$ m, respectively. As expected, the outage probability increases smoothly as a function of both variables. The difference in scenarios is minor but most evident at the lowest and highest link distance contours.

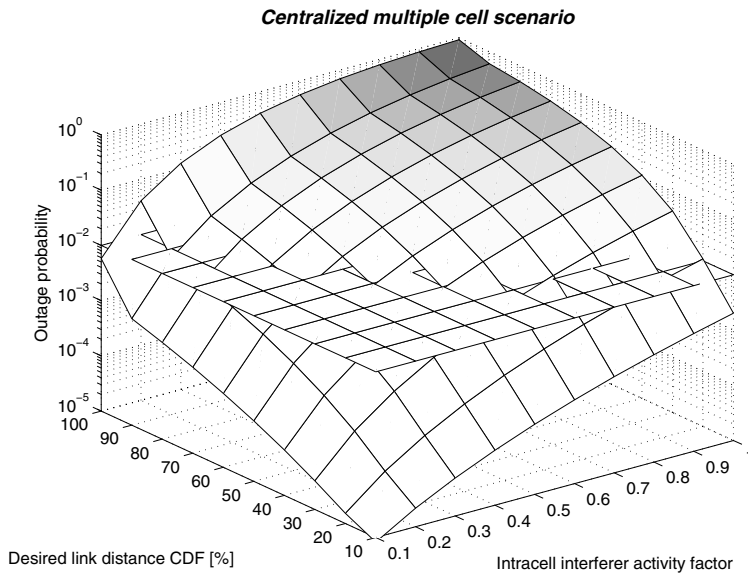


Fig. 63. Outage probability as a function of intracell interferer activity factor and desired link distance percentile in a centralized multiple cell scenario ($N = 23$, $U = 96$).

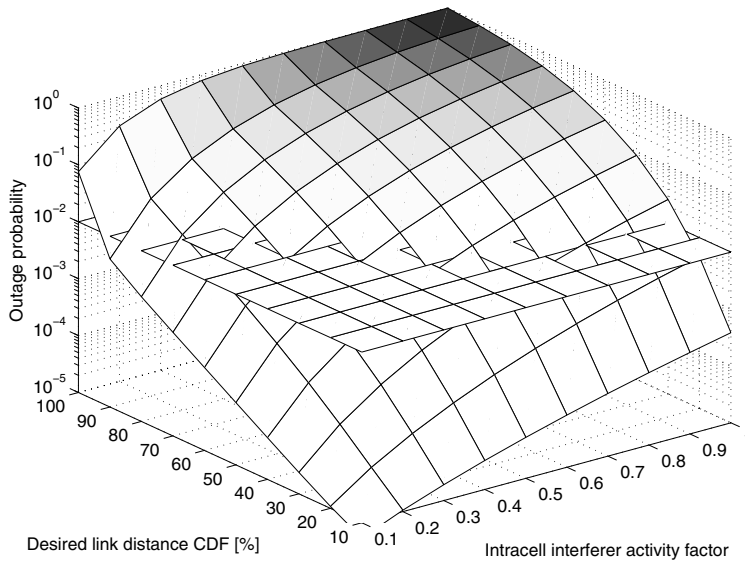
Distributed multiple cell scenario

Fig. 64. Outage probability as a function of intracell interferer activity factor and desired link distance percentile in a distributed multiple cell scenario ($N = 23$, $U = 96$).

Fig. 65 illustrates the impact of normalized timing errors in the reception of the 6th derivate of the Gaussian pulse according to delay estimation errors extracted from (146) and (147). All link distances are set to median values in the centralized multiple cell scenario. The intracell load is limited to $N = 1$, and intercell load is set to 50% ($U = 8 \times 12$). High sensitivity to offsets in receiver timing is observed. The optimal number of rake fingers remains unchanged in the presence of timing errors. The reference outage level is exceeded at any number of rake fingers for timing errors larger than $0.03T_p$.

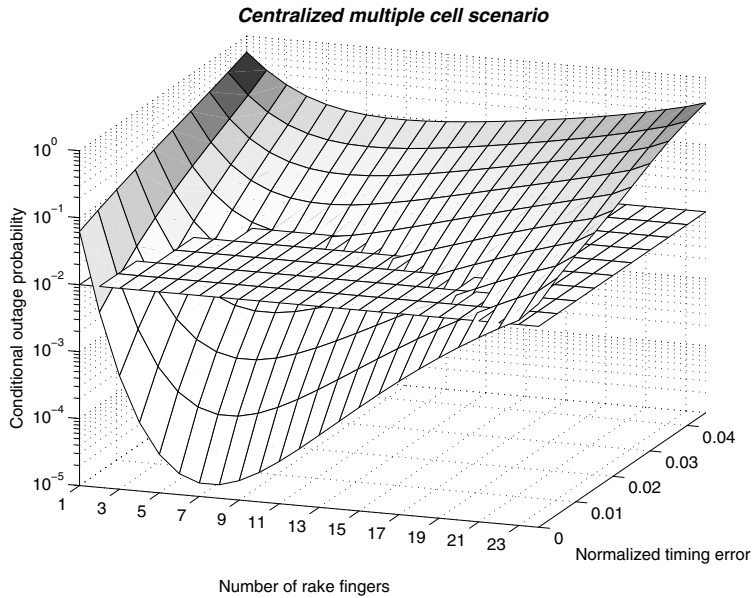


Fig. 65. Effect of timing error (Gaussian 6th derivative waveform, $N = 1$, $U = 96$).

Sensitivity to the S/I target variation is illustrated in Fig. 66. We can observe that on the average, one dB change in the target performance scales P_{out} up or down one magnitude order at low probability values. Loosening $(S/I)_{tar}$ by 1 dB gains more than is lost by tightening the target by 1 dB. As shown in (151), the actual target will be a trade-off between several system parameters.

Fig. 67 compares the sensitivity of conditional outage probability to the alternated single signal standard deviations. In addition to the FW approximation, the Ho's modified SY approximation and Monte Carlo simulation results are depicted. All methods provide a close match in results for lognormal signals having standard deviations $\sigma < 3$ dB. In the default case, $\sigma = 3.4$ dB, the Monte Carlo simulation points fall between the FW and SY approximation results, yet closer to the SY curve. For larger initial variances the FW approximation becomes gradually more and more pessimistic.

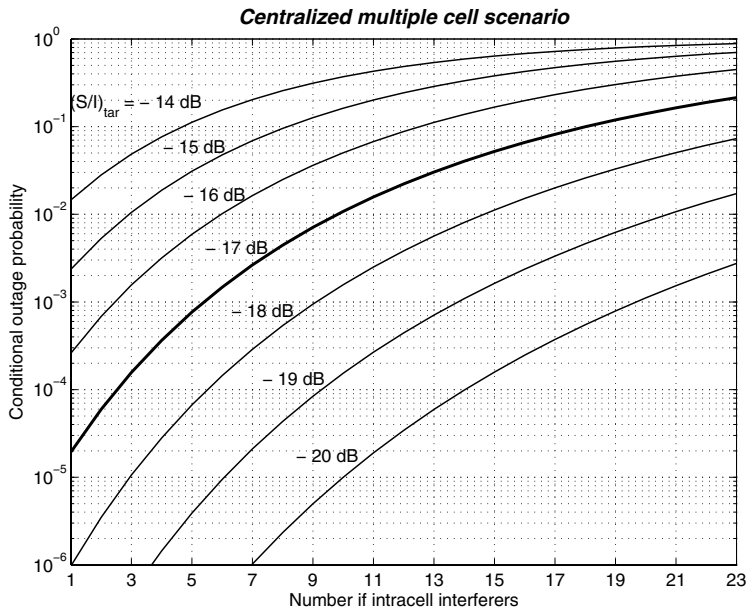


Fig. 66. Impact of the signal-to-interference target variation to the conditional outage probability in a centralized multiple cell scenario ($U = 96$).

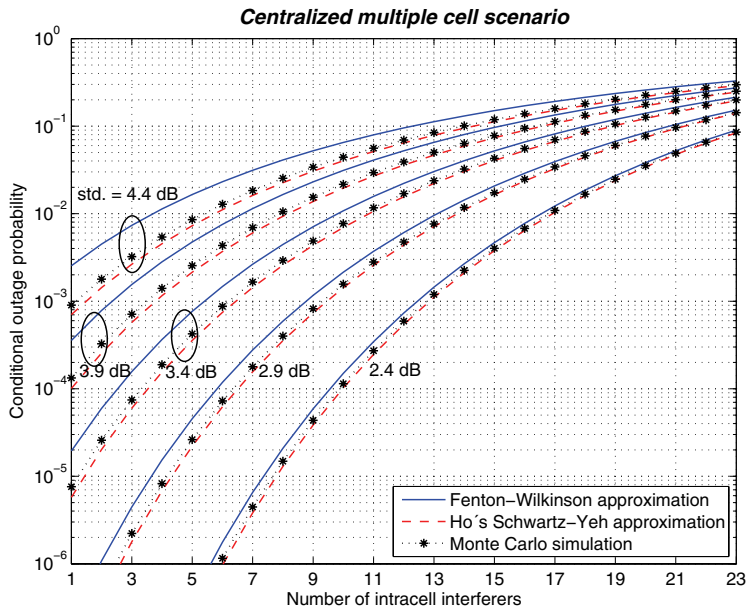


Fig. 67. Outage probability sensitivity to signal variance in a centralized multiple cell scenario with three different lognormal sum evaluation methods ($U = 96$).

Fig. 68 illustrates the impact of multipath correlation r_{mpi} to the conditional outage probability at the centralized topology with 96 active intercell interferers. All link distances are set at the median values. The correlation coefficients are from top to bottom 0.99, 0.75, 0.5, 0.25, and 0. It can be concluded that at low intracell loads (i.e., small outages) both approximations are highly pessimistic in the presence of correlated random variables. The gap between the methods decreases at higher loads. The lowest set of curves ($r_{mpi} = 0$) shows a reasonably good match, especially between the SY and MC methods.

The setup in Fig. 69 is changed to the distributed multicell case with 192 intercell interferers. The multipath correlation is fixed to 0.5. The desired link distance is varied between 30 and 70 percentile contours of the link distance CDF. For the shortest link the difference in outage is at its most prominent (even multiple orders of magnitude). In other cases, when the intracell load is high enough, the approximations coincide fairly with the simulation points.

Fig. 70 depicts the surface plots of differences between simulated and FW approximated conditional outage probabilities in the same scenario as in Fig. 69. Now the desired link distance CDF is divided into 10 percentile segments in the range 10-100%. The absolute difference varies between -0.085 and 0.137 . It should be noted that the relative difference can be several orders of magnitude as was shown in Fig. 69. Because the difference gets both the negative and positive values, and abrupt changes along the plane occur, the valid usage area of the FW approximation becomes highly restricted.

Fig. 71 outlines the difference surface of the Ho's version of SY approximation and Monte Carlo simulation in the same scenario. It can be noted that the shape of this plot is almost identical to Fig. 70. However, in the numerical range, there are some deviations. The absolute minimum value is encountered now to be -0.058 and the maximum 0.152 .

Fig. 72 shows a similar illustration of SY and FW outage results. The outage difference of these methods varies between -0.032 and 0.012 . The magnitude is much less than when compared to the simulations. However, the shape of the plane resembles the previous examples (i.e., there is a cross-section where the magnitude order of the approximations switches).

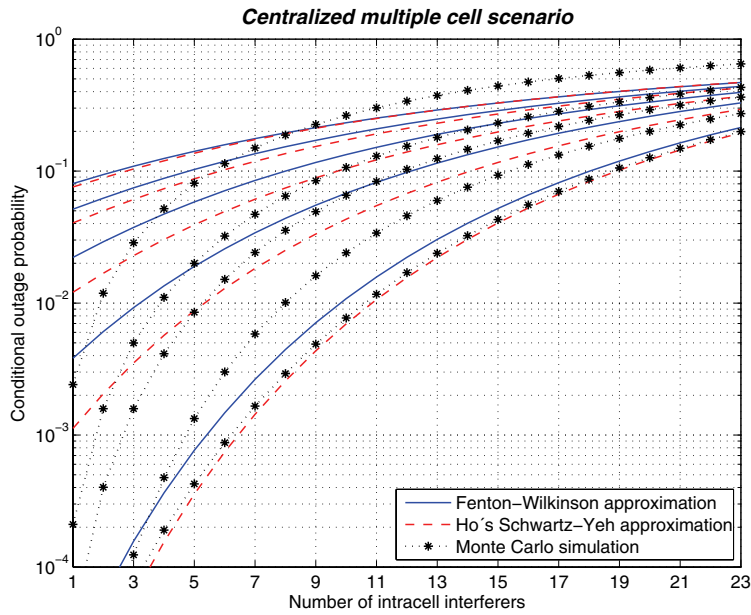


Fig. 68. Conditional outage probabilities with correlated multipaths in a centralized configuration ($r_{mpi} = 0.99, 0.75, 0.5, 0.25, 0$ from top to bottom, $U = 96$).

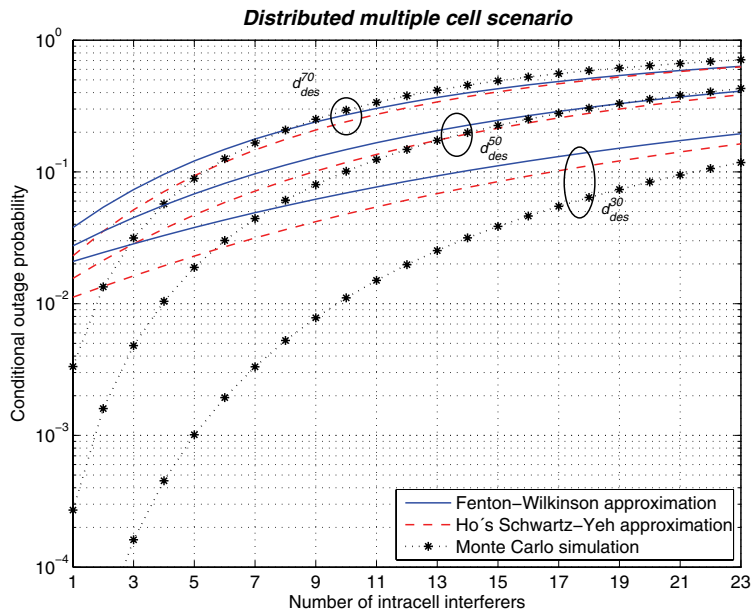


Fig. 69. Conditional outage probabilities with correlated multipaths ($r_{mpi} = 0.5$) in a distributed configuration ($U = 192$).

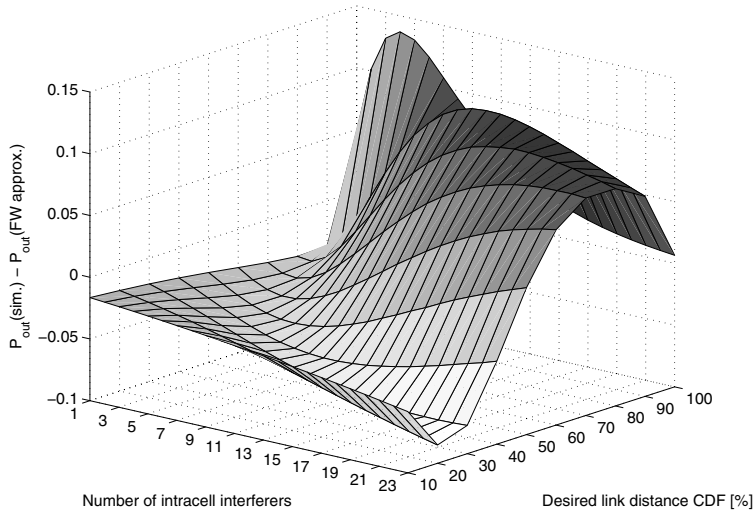
Distributed multiple cell scenario

Fig. 70. The difference of simulated and FW-approximated conditional outage probabilities in a distributed configuration ($r_{mpi} = 0.5$, $U = 192$).

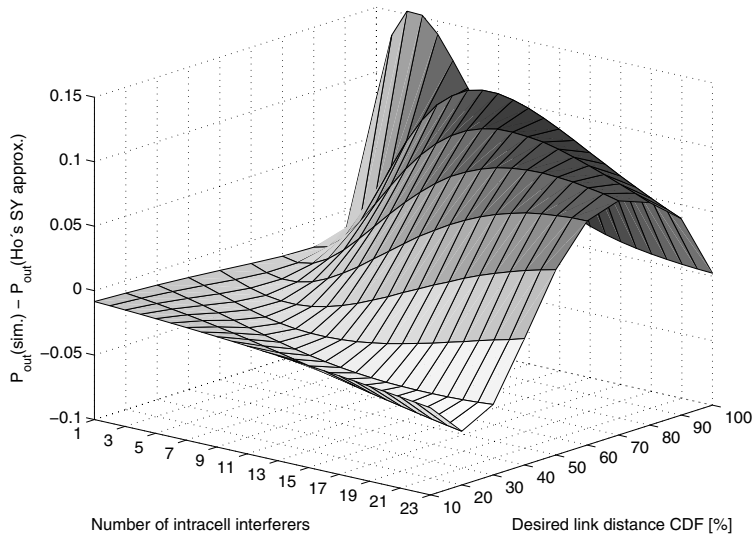
Distributed multiple cell scenario

Fig. 71. The difference of simulated and SY-approximated conditional outage probabilities in a distributed configuration ($r_{mpi} = 0.5$, $U = 192$).

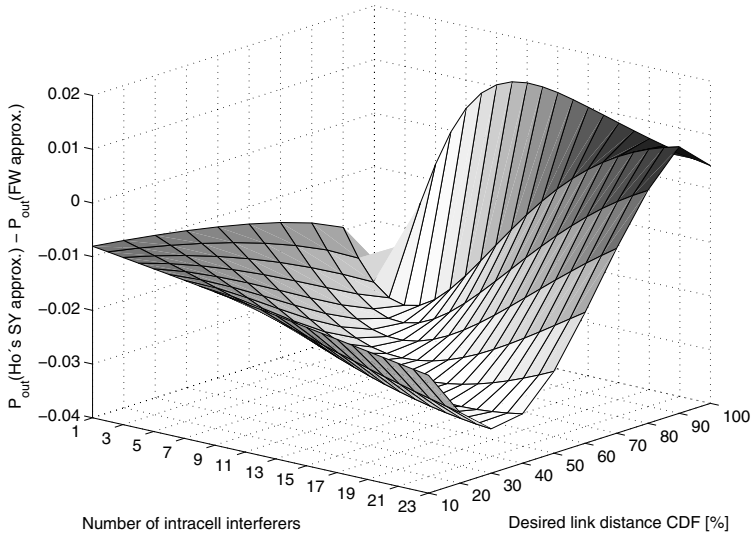
Distributed multiple cell scenario

Fig. 72. The difference of SY- and FW-approximated conditional outage probabilities in a distributed configuration ($r_{mpi} = 0.5$, $U = 192$).

5.5 Chapter summary

Analytical evaluations of the cochannel interference limited outage probabilities in DS-UWB systems were conducted. Square-shaped cell configurations with either centralized or distributed topologies were assumed, and link distance PDFs for these cell configurations were derived and simulated. Lognormal multipath propagation parameters, aggregate intra- and intercell multiuser interference, rake receiver finger allocation, and user activity were taken into account in the calculations. Numerical results showed that a moderate number of rake fingers ($L_0 = 9$ in these examples) is enough even in dense multipath channel. The optimal number of rake fingers was observed to be rather insensitive to parameter variations. Relative distances and path losses of the desired link and interfering links had a strong impact on the detected outage probability. Intracell interference had a much stronger impact on outage performance than intercell interference. Sensitivity to UWB pulse waveform timing uncertainty was evident for the 6th derivate Gaussian pulse template waveform at the correlator receiver (5th derivate waveform in the radio channel). Differences between centralized and distributed topology link distance probability density functions were obvious but much less notable in cumulative distribution functions and thereby in outage probability performance. Likewise, circular and hexagonal cell model geometries closely resembled the cellular model constructed of squares. In correlated multipath fading channels the studied lognormal sum approximations were not accurate in the outage probability assessment.

6 Conclusions and future work

6.1 Summary and conclusions

Analytical frameworks for the effective capacity analysis of advanced wideband direct sequence CDMA and UWB networks were presented in the thesis. The first approach assessed system user capacity in the presence of various imperfections in the multipath channel with single user space-time rake receivers and their two multiuser detection enhancements. Chapter 2 reviewed the prior and parallel literature in the research areas closely related to the thesis. In Chapter 3, the wideband signal model was derived for complex transmitted signal. Mathematical formulas for the transmitted and received waveforms and radio channel were given. A generic exponentially decaying space-time multipath intensity profile was adopted for the analysis.

Chapter 4 was devoted to the wideband CDMA performance analysis. CDMA system average capacity was approached from the overall signal-to-noise ratio point of view, where the desired cell multiple access interference was modeled in more detail, while other interference was embedded into an additional Gaussian noise component. Models for equal gain and maximal ratio combiners accounting for parameter estimation errors were derived. Then, effective user capacities and sensitivity functions for the relative capacity loss were defined for three chosen imperfect space-time receiver structures: 1) *rake*, 2) *rake+decorrelator*, and 3) *rake+nonlinear interference canceller*. Numerical capacity and sensitivity examples for each receiver type were presented at two multipath intensity profiles as a function of diversity order and normalized maximum Doppler shift. In these examples the carrier phase, code delay, and amplitude estimation errors were assumed to rely on phase- and delay-locked loop characteristics. Performance comparison demonstrated that both multiuser receiver structures can achieve multifold capacities compared to the plain single user rake receiver at slow fading channels and at low diversity orders. However, the gap diminished or vanished completely at high fading rates and/or at large number of combined diversity branches.

Chapter 5 outlined the second capacity analysis framework that concentrated on indoor DS-UWB personal area networks. User capacity was studied as a function of cochannel interference induced outage probability. Spatial cell configurations, based on

circular, square, and hexagonal shapes, were considered. Closed-form expressions were derived for the link distance probability density functions in centralized single- and multi-cell network topologies. Simulations were used to determine link distance statistics in distributed topologies and to confirm all analytical derivations. By utilizing these statistics, resorting to simulations can be reduced in search of the network performance limits. The desired link interpath interference and multipath interference from interfering links was modeled and taken into consideration in the numerical calculations. Lognormal power sum statistics were extracted mostly through the simple Fenton–Wilkinson method. In some cases, the Schwartz–Yeh approximation and Monte Carlo simulations were also included in the performance assessment. An easily scalable dual-slope path loss model was utilized with an option to account for wall losses.

Numerical results showed that the actual cell shape is not very decisive in the link distance statistics. On the other hand, the number of rake fingers, loading in the desired cell vs. surrounding cells, relative distances of the desired link and interfering links, path losses, timing errors, signal-to-interference target, fading statistics, and multipath correlation are major factors in the capacity and quality-of-service trade-off. It was also demonstrated that the SY and FW approximations fail to represent outage statistics in the presence of correlated multipaths. In such cases the Monte Carlo simulations or other more sophisticated approximations are viable alternatives to be exploited.

6.2 Future research directions

As discussed in Section 4.2.3 the numerical results in the thesis rely on simple suboptimal parameter estimators. Therefore, it would be interesting to extend the analysis to more advanced and complex estimation algorithms (e.g., joint maximum-likelihood based or Kalman filtering). It is expected that sensitivity to system impairments could be reduced significantly by utilizing these algorithms. However, the associated drawbacks would be increased implementation complexity and higher energy consumption. Further analysis and comparison of the power control algorithms listed in Section 4.1 would also be worth considering. Spatial diversity in the numerical examples was restricted to dual-antenna diversity in the numerical examples of the thesis. An approach towards generic MIMO concept with multiple transmit and receive antennas would be one way to extend the framework.

In the development of wireless personal area and sensor networks [347], one of the promising application scenarios is related to the concept of *wireless hospital* [348]. UWB technologies can offer wireless short range data communication links as well as accurate location and tracking services for hospital and healthcare needs. CWC is included in the WILHO (wireless technology in hospital operation management) consortium and program whose main goal is to enhance hospital management processes by using wireless technology. Two hospitals in Oulu are involved in running the related piloting projects. Participation in WILHO offers practical and meaningful platforms to apply theoretical results in real environments and use cases.

References

1. Glisic S & Pirinen P (1999) Wideband CDMA network sensitivity function. *IEEE Journal on Selected Areas in Communications* 17(10): 1781–1793.
2. Pirinen P & Glisic S (2006) Capacity losses in wireless CDMA networks using imperfect decorrelating space-time rake receiver in fading multipath channel. *IEEE Transactions on Wireless Communications* 5(8): 2072–2081.
3. Pirinen P (2006) Outage analysis of ultra-wideband system in lognormal multipath fading and square-shaped cellular configurations. *EURASIP Journal on Wireless Communications and Networking* 2006: 10 p. [online]. 2006 [cited Nov 8, 2006]. Available from: <http://www.hindawi.com/GetArticle.aspx?doi=10.1155/WCN/2006/19460&e=cta>.
4. Pirinen P & Glisic S (2001) Sensitivity of wideband CDMA capacity to various channel and system parameter imperfections. *Proc. IEEE International Conference on Communications (ICC)*, Helsinki, Finland, 10: 3000–3004.
5. Pirinen P (2003) CDMA capacity comparison using space-time rake based receivers in fading multipath channels. *Proc. the fourth Finnish Wireless Communications Workshop (FWCW)*, Oulu, Finland, 79–82 [CD-ROM].
6. Pirinen P (2004) Outage evaluation of ultra wideband spread spectrum system with rake combining in lognormal fading multipath channels. *Proc. IEEE International Symposium on Personal, Indoor and Mobile Radio Communications (PIMRC)*, Barcelona, Spain, 4: 2446–2450.
7. Pirinen P (2005) Ultra wideband system outage studies in a square cell with partial rake receiver and lognormal fading. *Proc. IEEE International Conference on Ultra-Wideband (ICU)*, Zurich, Switzerland, 230–235.
8. Pirinen P (2006) Cellular topology and outage evaluation for DS-UWB system with correlated lognormal multipath fading. *Proc. IEEE International Symposium on Personal, Indoor and Mobile Radio Communications (PIMRC)*, Helsinki, Finland, 5 p [CD-ROM].
9. Pickholtz RL, Milstein LB & Schilling DL (1991) Spread spectrum for mobile communications. *IEEE Transactions on Vehicular Technology* 40(2): 313–321.
10. Kohno R, Meidan R & Milstein LB (1995) Spread spectrum access methods for wireless communications. *IEEE Communications Magazine* 33(1): 58–67.
11. Lee WCY (1991) Overview of cellular CDMA. *IEEE Transactions on Vehicular Technology* 40(2): 291–302.

12. Gilhousen KS, Jacobs IM, Padovani R, Viterbi AJ, Weaver LA Jr. & Wheatley CE III (1991) On the capacity of a cellular CDMA system. *IEEE Transactions on Vehicular Technology* 40(2): 303–312.
13. Gaiani E, Muratore F & Palestini V (1993) Capacity evaluation in the up-link of a DS-CDMA system. *Proc. IEEE International Conference on Universal Personal Communications (ICUPC)*, Ottawa, Ont., Canada, 1: 304–308.
14. Levi L, Muratore F, Palestini V & Romano G (1993) Performance of a DS-CDMA system in a multipath fading environment. *Proc. IEEE International Conference on Universal Personal Communications (ICUPC)*, Ottawa, Ont., Canada, 1: 28–32.
15. Li Y, Woerner BD, Tanis W II & Hughes M (1993) Simulation of CDMA using measured channel impulse response data. *Proc. IEEE Vehicular Technology Conference (VTC)*, Secaucus, NJ, USA, 428–431.
16. Padgett JE (1994) Capacity analysis for unlicensed wireless communications. *Proc. IEEE Military Communications Conference (MILCOM)*, Fort Monmouth, NJ, USA, 3: 906–910.
17. Swales SC, Busby T, Purle DJ, Beach MA & McGeehan JP (1993) A comparison of CDMA techniques for third generation mobile radio systems. *Proc. IEEE Vehicular Technology Conference (VTC)*, Secaucus, NJ, USA, 424–427.
18. Gudmundson B, Sköld J & Uglund JK (1992) A comparison of CDMA and TDMA systems. *Proc. IEEE Vehicular Technology Conference (VTC)*, Denver, CO, USA, 2: 732–735.
19. Pupolin S, Tomba L & Zorzi M (1995) Forward link performance of multiple access schemes in cellular systems. *Proc. IEEE International Conference on Communications (ICC)*, Seattle, WA, USA, 2: 1070–1074.
20. Sari H, Steendam H & Moeneclaey M (1999) On the uplink capacity of cellular CDMA and TDMA over nondispersive channels. *Proc. IEEE Vehicular Technology Conference (VTC)*, Houston, TX, USA, 2: 1638–1642.
21. Heath MR & Newson P (1992) On the capacity of spread-spectrum CDMA for mobile radio. *Proc. IEEE Vehicular Technology Conference (VTC)*, Denver, CO, USA, 2: 985–988.
22. Huang CY & Daut DG (1996) Evaluation of capacity for CDMA systems on frequency-selective fading channels. *Proc. IEEE International Conference on Universal Personal Communications (ICUPC)*, Cambridge, MA, USA, 2: 975–979.
23. Kerr R, Wang Q & Bhargava VK (1992) Capacity analysis of cellular CDMA. *Proc. IEEE International Symposium on Spread Spectrum Techniques and Applications (ISSSTA)*, Yokohama, Japan, 235–238.
24. Shimizu M, Asano Y & Daido Y (1993) Reverse-link performance for microcellular DS-CDMA systems with orthogonal sequence spreading. *Proc. IEEE International Conference on Universal Personal Communications (ICUPC)*, Ottawa, Ont., Canada, 1: 224–248.
25. Simić JR & Simić ĐČ (1999) On the capacity of a cellular CDMA system employing power control on fading channels. *Proc. International Conference on Telecommunications in Modern Satellite, Cable and Broadcasting Services (TELSIKS)*, Niš, Yugoslavia, 2: 562–565.
26. Granzow W & Koch W (1992) Potential capacity of TDMA and CDMA cellular telephone systems. *Proc. IEEE International Symposium on Spread Spectrum Techniques and Applications (ISSSTA)*, Yokohama, Japan, 243–246.
27. Behbahani F & Hashemi H (1994) Performance and capacity evaluations of CDMA mobile radio systems – reverse link analysis. *Proc. IEEE Vehicular Technology Conference (VTC)*, Stockholm, Sweden, 1: 65–69.
28. Sathyendran A, Sowerby KW & Shafi M (1994) Performance evaluation of a multiple-cell CDMA radio system. *Proc. IEEE Vehicular Technology Conference (VTC)*, Stockholm, Sweden, 1: 26–30.

29. Milstein LB, Rappaport TS & Barghouti R (1992) Performance evaluation for cellular CDMA. *IEEE Journal on Selected Areas in Communications* 10(4): 680–689.
30. Jalali A & Mermelstein P (1994) Effects of diversity, power control, and bandwidth on the capacity of microcellular CDMA systems. *IEEE Journal on Selected Areas in Communications* 12(5): 952–961.
31. Oh SW & Li KH (1999) Forward-link analysis of a cellular DS-CDMA over generalised fading channels using saddlepoint integration. *IEE Proceedings Communications* 146(2): 138–143.
32. Oh SW, Cheah KL & Li KH (2000) Forward-link BER analysis of asynchronous cellular DS-CDMA over Nakagami-faded channels using combined PDF approach. *IEEE Transactions on Vehicular Technology* 49(1): 173–180.
33. Kim KI (1993) CDMA cellular engineering issues. *IEEE Transactions on Vehicular Technology* 42(3): 345–350.
34. Lau FCM & Tam WM (1995) Effects of increased capacity in CDMA cellular system. *Proc. URSI International Symposium on Signals, Systems, and Electronics (ISSSE)*, San Francisco, USA, 579–582.
35. Lau FCM (1998) Comments on “Overview of cellular CDMA”. *IEEE Transactions on Vehicular Technology* 47(1): 369–371.
36. Tonguz OK & Wang MM (1994) Cellular CDMA networks impaired by Rayleigh fading: system performance with power control. *IEEE Transactions on Vehicular Technology* 43(3): 515–527.
37. Lee C-C & Steele R (1996) Closed-loop power control in CDMA systems. *IEE Proceedings Communications* 143(4): 231–239.
38. Newson P & Heath MR (1994) The capacity of a spread spectrum CDMA system for cellular mobile radio with consideration of system imperfections. *IEEE Journal on Selected Areas in Communications* 12(4): 673–684.
39. Prasad R, Jansen MG & Kegel A (1993) Capacity analysis of a cellular direct sequence code division multiple access system with imperfect power control. *IEICE Transactions on Communications* E76-B(8): 894–905.
40. Jansen MG & Prasad R (1995) Capacity, throughput, and delay analysis of a cellular DS CDMA system with imperfect power control and imperfect sectorization. *IEEE Transactions on Vehicular Technology* 44(1): 67–75.
41. Kudoh E & Matsumoto T (1992) Effect of transmitter power control imperfections on capacity in DS/CDMA cellular mobile radios. *Proc. IEEE International Conference on Communications (ICC)*, Chicago, IL, USA, 1: 237–242.
42. Kudoh E & Matsumoto T (1992) Effects of power control error on the system capacity of DS/CDMA cellular mobile radios. *IEICE Transactions on Communications* E75-B(6): 524–529.
43. Stüber GL (1996) *Principles of Mobile Communication*. Kluwer Academic Publishers.
44. Soleimanipour M & Freeman GH (1996) A realistic approach to the capacity of cellular CDMA systems. *Proc. IEEE Vehicular Technology Conference (VTC)*, Atlanta, GA, USA, 2: 1125–1129.
45. Vatalaro F, Corazza GE, Ceccarelli F & De Maio G (1996) CDMA cellular systems performance with imperfect power control and shadowing. *Proc. IEEE Vehicular Technology Conference (VTC)*, Atlanta, GA, USA, 2: 874–878.
46. Miller JE & Miller SL (1996) DS-SS-CDMA uplink performance with imperfect power control and a base station antenna array. *Proc. IEEE Vehicular Technology Conference (VTC)*, Atlanta, GA, USA, 1: 66–70.
47. Falciassecca G, Gaiani E, Missiroli M, Muratore F, Palestini V & Riva G (1992) Influence of propagation parameters on cellular CDMA capacity and effects of imperfect power control. *Proc. IEEE International Symposium on Spread Spectrum Techniques and Applications (ISSSTA)*, Yokohama, Japan, 255–258.
48. Corazza GE, De Maio G & Vatalaro F (1998) CDMA cellular systems performance with fading, shadowing, and imperfect power control. *IEEE Transactions on Vehicular Technology* 47(2): 450–459.

49. Tam WM & Lau FCM (1997) Analysis of imperfect power control in CDMA cellular systems. Proc. IEEE International Symposium on Personal, Indoor and Mobile Communications (PIMRC), Helsinki, Finland, 3: 892–897.
50. Tam WM & Lau FCM (1997) Capacity analysis of a CDMA cellular system with power control schemes. Proc. IEEE International Conference on Universal Personal Communications (ICUPC), San Diego, CA, USA, 2: 608–612.
51. Ye W & Haimovich AM (1998) Outage probability of cellular CDMA systems with space diversity, Rayleigh fading, and power control error. IEEE Communications Letters 2(8): 220–222.
52. Sim ML & Chuah HT (2000) Performance analysis of reverse link wideband CDMA cellular system under fast closed-loop power. Proc. IEE First International Conference on 3G Mobile Communication Technologies, London, UK, 51–55.
53. Baiocchi A, Sestini & Delli Priscoli F (1996) Effects of user mobility on the capacity of a CDMA cellular network. European Transactions on Telecommunications 7(4): 305–314.
54. Sunay MO & McLane PJ (1995) Effects of carrier phase and chip timing errors on the capacity of a quadriphase spread BPSK modulated DS CDMA system. Proc. IEEE Global Telecommunications Conference (GLOBECOM), Singapore, 2: 1114–1120.
55. Panicker J & Kumar S (1996) Effect of system imperfections on BER performance of a CDMA receiver with multipath diversity combining. IEEE Transactions on Vehicular Technology 45(4): 622–630.
56. Wu J-S, Chung J-K & Wen C-C (1998) Hot-spot traffic relief with a tilted antenna in CDMA cellular networks. IEEE Transactions on Vehicular Technology 47(1): 1–9.
57. Nguyen T, Dassanayake P & Faulkner M (2001) Capacity of CDMA cellular systems with adaptive sectorisation and non-uniform traffic. Proc. IEEE Vehicular Technology Conference (VTC-Fall), Atlantic City, NJ, USA, 2: 1163–1167.
58. Viterbi AM & Viterbi AJ (1993) Erlang capacity of a power controlled CDMA system. IEEE Journal on Selected Areas in Communications 11(6): 892–900.
59. Landolsi MA, Veeravalli VV & Jain N (1996) New results on the reverse link capacity of CDMA cellular networks. Proc. IEEE Vehicular Technology Conference (VTC), Atlanta, GA, USA, 3: 1462–1466.
60. Liberti JC Jr. & Rappaport TS (1994) Analytical results for capacity improvements in CDMA. IEEE Transactions on Vehicular Technology 43(3): 680–690.
61. Naguib AF, Paulraj A & Kailath T (1994) Capacity improvement with base-station antenna arrays in cellular CDMA. IEEE Transactions on Vehicular Technology 43(3): 691–698.
62. Tomba L (1996) Outage probability in CDMA cellular systems with discontinuous transmission. Proc. IEEE International Symposium on Spread Spectrum Techniques and Applications (ISSSTA), Mainz, Germany, 2: 481–485.
63. Tomba L (1997) Computation of the outage probability in Rice fading radio channels. European Transactions on Telecommunications 8(2): 127–134.
64. Boyer P, Stojanovic M & Proakis J (2001) A simple generalization of the CDMA reverse link pole capacity formula. IEEE Transactions on Communications 49(10): 1719–1722.
65. Chebaro T & Godlewski P (1996) Average external interference in cellular radio CDMA systems. IEEE Transactions on Communications 44(1): 23–25.
66. Lee DD, Kim DH, Chung YJ, Kim HG & Whang KC (1996) Other-cell interference with power control in macro/microcell CDMA networks. Proc. IEEE Vehicular Technology Conference (VTC), Atlanta, GA, USA, 2: 1120–1124.
67. Wu J-S, Chung J-K & Yang Y-C (1996) Co-channel interference and capacity for two-tier CDMA cellular systems. Proc. IEEE International Symposium on Personal, Indoor and Mobile Radio Communications (PIMRC), Taipei, Taiwan, 1: 88–92.
68. Kim JY & Stüber GL (2002) CDMA soft handoff analysis in the presence of power control error and shadowing correlation. IEEE Transactions on Wireless Communications 1(2): 245–255.

69. Viterbi AJ & Viterbi AM, Gilhousen KS & Zehavi E (1994) Soft handoff extends CDMA cell coverage and increases reverse link capacity. *IEEE Journal on Selected Areas in Communications* 12(8): 1281–1288.
70. Viterbi AJ & Viterbi AM & Zehavi E (1994) Other-cell interference in cellular power-controlled CDMA. *IEEE Transactions on Communications* 42(2/3/4): 1501–1504.
71. Karlsson RS (1999) Radio resource sharing and capacity of some multiple access methods in hierarchical cell structures. *Proc. IEEE Vehicular Technology Conference (VTC-Fall)*, Amsterdam, Netherlands, 5: 2825–2829.
72. Stüber GL & Kchao C (1992) Analysis of a multiple-cell direct-sequence CDMA cellular mobile radio system. *IEEE Journal on Selected Areas in Communications* 10(4): 669–679.
73. Kchao C & Stüber GL (1993) Analysis of a direct-sequence spread-spectrum cellular radio system. *IEEE Transactions on Communications* 41(10): 1507–1516.
74. Kim DK & Adachi F (2001) Theoretical analysis of reverse link capacity for an SIR-based power-controlled cellular CDMA system in a multipath fading environment. *IEEE Transactions on Vehicular Technology* 50(2): 452–464.
75. Lee JS & Miller LE (1996) The effect of path diversity (rake) on link reliability in CDMA cellular systems - a realistic assessment of system capacity. *Proc. IEEE International Symposium on Personal, Indoor and Mobile Radio Communications (PIMRC)*, Taipei, Taiwan, 3: 1130–1134.
76. Mar J & Chen H-Y (1998) Performance analysis of cellular CDMA networks over frequency-selective fading channel. *IEEE Transactions on Vehicular Technology* 47(4): 1234–1244.
77. Sathyendran A, Sowerby KW & Shafi M (1999) A statistical approach to the analysis of DS/CDMA cellular systems employing rake receivers and sectorized antennas. *IEEE Transactions on Vehicular Technology* 48(1): 8–19.
78. Alouini M-S, Kim SW & Goldsmith A (1997) Rake reception with maximal-ratio and equal-gain combining for DS-CDMA systems in Nakagami fading. *Proc. IEEE International Conference on Universal Personal Communications (ICUPC)*, San Diego, CA, USA, 2: 708–712.
79. Bottomley GE, Ottosson T & Wang Y-PE (2000) A generalized rake receiver for interference suppression. *IEEE Journal on Selected Areas in Communications* 18(8): 1536–1545.
80. Efthymoglou GP, Piboongunon T & Aalo VA (2006) Performance of DS-CDMA receivers with MRC in Nakagami- m fading channels with arbitrary fading parameters. *IEEE Transactions on Vehicular Technology* 55(1): 104–114.
81. Choi W & Andrews JG (2005) On spatial multiplexing in cellular MIMO-CDMA systems with linear receivers. *Proc. IEEE International Conference on Communications (ICC)*, Seoul, Korea, 4: 2277–2281.
82. Kondo S & Milstein LB (1996) Performance of multicarrier DS CDMA systems. *IEEE Transactions on Communications* 44(2): 238–246.
83. Kim DK & Hwang S-H (2002) Capacity analysis of an uplink synchronized multicarrier DS-CDMA system. *IEEE Communications Letters* 6(3): 99–101.
84. Mandayam NB, Holtzman J & Barberis S (1995) Erlang capacity of an integrated voice/data DS-CDMA wireless system with variable bit rate sources. *Proc. IEEE International Symposium on Personal, Indoor and Mobile Radio Communications (PIMRC)*, Toronto, Ont., Canada, 3: 1078–1082.
85. Huang W & Bhargava VK (1996) Performance evaluation of a DS/CDMA cellular system with voice and data services. *Proc. IEEE International Symposium on Personal, Indoor and Mobile Radio Communications (PIMRC)*, Taipei, Taiwan, 2: 588–592.
86. Sampath A, Mandayam NB & Holtzman JM (1997) Erlang capacity of a power controlled integrated voice and data CDMA system. *Proc. IEEE Vehicular Technology Conference (VTC)*, Phoenix, AZ, USA, 3: 1557–1561.
87. Ayyagari D & Ephremides A (1999) Cellular multicode CDMA capacity for integrated (voice and data) services. *IEEE Journal on Selected Areas in Communications* 17(5): 928–938.
88. Choi W & Kim JY (2001) Forward-link capacity of a DS/CDMA system with mixed multirate sources. *IEEE Transactions on Vehicular Technology* 50(3): 737–749.

89. Hartmann C (2002) On capacity and blocking of multi service CDMA systems with smart antennas. Proc. IEEE Vehicular Technology Conference (VTC-Fall), Vancouver, BC, Canada, 1: 72–76.
90. Kim JY, Stüber GL & Akyildiz IF (2002) A simple performance/capacity analysis of multiclass macrodiversity CDMA cellular systems. IEEE Transactions on Communications 50(2): 304–308.
91. Kundu S & Chakrabarti S (2003) Outage and BER analysis of cellular CDMA for integrated services with correlated signal and interference. IEEE Communications Letters 7(10): 478–480.
92. Lee SJ, Lee HW & Sung DK (1999) Capacities of single-code and multicode DS-CDMA systems accommodating multiclass services. IEEE Transactions on Vehicular Technology 48(2): 376–384.
93. Mathar R & Remiche M-A (2001) The impact of different services on the outage probability in UMTS. Proc. IEEE Vehicular Technology Conference (VTC-Fall), Atlantic City, NJ, USA, 2: 934–937.
94. Akhtar S & Zeghlache D (1999) Capacity evaluation of the UTRA WCDMA interface. Proc. IEEE Vehicular Technology Conference (VTC-Fall), Amsterdam, Netherlands, 2: 914–918.
95. Benn H, O'Neill R, Owen R & Johnson C (1998) UMTS air interface simulation. Proc. IEE Colloquium on UMTS – The R Challenges, London, UK, 6/1–6/8.
96. García MR, Lati JEB Jerez JMR & Estrella AD (2000) Capacity analysis of an integrated wideband CDMA system. Proc. IEEE/AFCEA Information Systems for Enhanced Public Safety and Security (EUROCOMM), Munich, Germany, 204–211.
97. Sathyendran A, Sowerby KW & Shafi M (1999) Capacity estimation for 3rd generation CDMA cellular systems. Proc. IEEE Vehicular Technology Conference (VTC-Spring), Houston, TX, USA, 1: 356–360.
98. Schacht M, Dekorsy A & Jung P (2003) System capacity from UMTS smart antenna concepts. Proc. IEEE Vehicular Technology Conference (VTC-Fall), Lake Buena Vista, FL, USA, 5: 3126–3130.
99. Jana R & Dey S (2000) 3G wireless capacity optimization for widely spaced antenna arrays. IEEE Personal Communications, 32–35.
100. Zhang Q & Yue O-C (2001) UMTS air interface voice/data capacity – part 1: reverse link analysis. Proc. IEEE Vehicular Technology Conference (VTC-Spring), Rhodes, Greece, 4: 2725–2729.
101. Wang J & Chen J (2001) Performance of wideband CDMA systems with complex spreading and imperfect channel estimation. IEEE Journal on Selected Areas in Communications 19(1): 152–163.
102. Pirinen P (2000) Conditional outage probability evaluation in WCDMA at high data rates. Proc. IEEE International Symposium on Spread Spectrum Techniques and Applications (ISSSTA), New Jersey, USA, 1: 230–234.
103. Chan CC & Hanly SV (2001) Calculating the outage probability in a CDMA network with spatial Poisson traffic. IEEE Transactions on Vehicular Technology 50(1): 183–204.
104. Choi W & Andrews JG (2004) Outage probability for maximal ratio combining receivers in asynchronous CDMA channels. Proc. IEEE International Symposium on Spread Spectrum Techniques and Applications (ISSSTA), Sydney, Australia, 779–783.
105. Anand S, Chockalingam A & Sivarajan KN (2002) Outage and capacity analysis of cellular CDMA with admission control. Proc. IEEE Wireless Communications and Networking Conference (WCNC), Orlando, FL, USA, 2: 908–912.
106. Evans JS & Everitt D (1999) On the teletraffic capacity of CDMA cellular networks. IEEE Transactions on Vehicular Technology 48(1): 153–165.
107. Fapojuwo AO (1993) Radio capacity of direct sequence code division multiple access mobile radio systems. IEE Proceedings-I 140(5): 402–408.
108. Hanly S & Mathar R (2002) On the optimal base-station density for CDMA cellular networks. IEEE Transactions on Communications 50(8): 1274–1281.

109. Ho C-J, Copeland JA, Lea C-T & Stüber GL (2000) Impact of the cell size on the cell's Erlang capacity and call admission control in the DS/CDMA cellular networks. Proc. IEEE Vehicular Technology Conference (VTC-Spring), Tokyo, Japan, 1: 385–389.
110. Jalali A & Mermelstein P (1994) Effects of diversity, power control, and bandwidth on the capacity of microcellular CDMA systems. IEEE Journal on Selected Areas in Communications 12(5): 952–961.
111. The 3rd generation partnership project. [online]. 2006 [cited Oct 5, 2006]. Available from: <http://www.3gpp.org>.
112. Holma H & Toskala A (Eds.) (2004) WCDMA for UMTS – Radio Access for Third Generation Mobile Communications, Third Edition. Wiley.
113. Duel-Hallen A, Holtzman J & Zvonar Z (1995) Multiuser detection for CDMA systems. IEEE Personal Communications Magazine 2(2): 46–58.
114. Moshavi S (1996) Multi-user detection for DS-CDMA communications. IEEE Communications Magazine 34(10): 124–136.
115. Juntti M & Glisic S (1997) Advanced CDMA for wireless communications. In: Glisic SG & Leppänen PA (Eds.) Wireless Communications. Kluwer Academic Publishers, p 447–490.
116. Woodward G & Vucetic BS (1998) Adaptive detection for DS-CDMA. Proceedings of the IEEE 86(7): 1413–1434.
117. Ojanperä T (1997) Overview of multiuser detection/interference cancellation for DS-CDMA. Proc. IEEE International Conference on Personal Wireless Communications (ICPWC), Mumbai, India, 115–119.
118. Koulakiotis D & Aghvami AH (2000) Data detection techniques for DS/CDMA mobile systems: a review. IEEE Personal Communications Magazine 7(3): 24–34.
119. Honig M & Tsatsanis MK (2000) Adaptive techniques for multiuser CDMA receivers. IEEE Signal Processing Magazine 17(3): 49–61.
120. Andrews JG (2005) Interference cancellation for cellular systems: a contemporary overview. IEEE Wireless Communications 12(2):19–29.
121. Lupas R & Verdú S (1989) Linear multiuser detectors for synchronous code-division multiple-access channels. IEEE Transactions on Information Theory 35(1): 123–136.
122. Lupas R & Verdú S (1990) Near-far resistance of multiuser detectors in asynchronous channels. IEEE Transactions on Communications 38(4): 496–508.
123. Verdú S (1998) Multiuser Detection. Cambridge University Press.
124. Zvonar Z & Brady D (1996) Linear multipath-decorrelating receivers for CDMA frequency-selective fading channels. IEEE Transactions on Communications 44(6): 650–653.
125. Zvonar Z (1996) Combined multiuser detection and diversity reception for wireless CDMA systems. IEEE Transactions on Vehicular Technology 45(1): 205–211.
126. Park J-H & Tranter WH (1998) Pseudo-decorrelating multiuser receivers for asynchronous code division multiple access (CDMA) systems. IEICE Transactions on Communications E81-B(11): 2197–2204.
127. Ghauri I & Iltis RA (1997) Capacity of the linear decorrelating detector for QS-CDMA. IEEE Transactions on Communications 45(9): 1039–1042.
128. Lee S-K & Kim SR (2002) A one-shot LDD with pre-SDC/post-MRC for random CDMA over asynchronous Rayleigh channels. IEEE Journal on Selected Areas in Communications 20(2): 257–263.
129. Im S & Kim E (2000) An iterative decorrelator with multipath combiners for CDMA frequency-selective fading channels. Proc. IEEE Vehicular Technology Conference (VTC-Spring), Tokyo, Japan, 1: 537–541.

130. Baines SJ, Tozer TC & Burr AG (1996) Performance limits for multi-user decorrelating detectors in DS-CDMA cellular radio systems. Proc. IEEE International Symposium on Spread Spectrum Techniques and Applications (ISSSTA), Mainz, Germany, 2: 486–491.
131. Chen H-H & Sim H-K (1997) Quasi-decorrelating detector (QDD) and its spreading codes dependent performance analysis. IEICE Transactions on Communications E80-B(9): 1337–1344.
132. Chen H-H & Wu C-F (2004) A novel approach to enable decorrelating multiuser detection without matrix inversion operations. International Journal of Communication Systems 17(9): 851–871.
133. Mandayam NB & Verdú S (1998) Analysis of an approximate decorrelating detector. Wireless Personal Communications 6(1/2): 97–111.
134. Kawahara T & Matsumoto T (1995) Joint decorrelating multiuser detection and channel estimation in asynchronous CDMA mobile communications channels. IEEE Transactions on Vehicular Technology 44(3): 506–515.
135. Pirinen P (2002) Spreading code set dependent decorrelator performance in an AWGN channel at the fraction of chip user delay offsets. Proc. IEEE International Symposium on Spread Spectrum Techniques and Applications (ISSSTA), Prague, Czech Republic, 2: 580–584.
136. Blanz J, Klein A, Naßhan M & Steil A (1994) Capacity of a cellular mobile radio system applying joint detection. COST 231 TD94 002, 18 pages.
137. Blanz J, Klein A, Naßhan M & Steil A (1994) Performance of a cellular hybrid C/TDMA mobile radio system applying joint detection and coherent receiver antenna diversity. IEEE Journal on Selected Areas in Communications 12(4): 568–579.
138. Manji S & Mandayam NB (1998) Outage probability for a zero forcing multiuser detector with random signature sequences. Proc. IEEE Vehicular Technology Conference (VTC), Ottawa, Ont., Canada, 1: 174–178.
139. Poor HV & Verdú S (1997) Probability of error in MMSE multiuser detection. IEEE Transactions on Information Theory 43(3): 858–871.
140. Juntti MJ & Latva-aho M (1999) Bit-error probability analysis of linear receivers for CDMA systems in frequency-selective fading channels. IEEE Transactions on Communications 47(12): 1788–1791.
141. Latva-aho M (1998) Advanced receivers for wideband CDMA systems. Doctoral Thesis. Acta Universitatis Ouluensis C 125.
142. Mirbagheri A & Yoon YC (2004) Performance analysis of a linear MMSE receiver for bandlimited random-CDMA using quadriphase spreading over multipath channels. IEEE Transactions on Wireless Communications 3(4): 1053–1066.
143. Dekorsy A & Brueck S (2003) On system capacity and coverage improvements by linear multiuser detection for UMTS. Proc. IEEE Vehicular Technology Conference (VTC-Spring), Jeju, Korea, 4: 2162–2166.
144. Kajiwara A & Nakagawa M (1994) Microcellular CDMA system with a linear multiuser interference canceler. IEEE Journal on Selected Areas in Communications 12(4): 605–611.
145. Díaz P & Agustí R (1994) Analysis of a linear interference canceller in cellular DS/CDMA systems. Proc. IEEE Vehicular Technology Conference (VTC), Stockholm, Sweden, 2: 785–788.
146. Díaz P & Agustí R (1994) On the influence of the channel impulsional response estimation on the performance of a linear interference canceller for a DS/CDMA system. Proc. IEEE International Symposium on Personal, Indoor and Mobile Radio Communications (PIMRC), The Hague, Netherlands, 2: 529–532.

147. Díaz P & Agustí R (1995) Performance of a linear interference canceller for a DS/CDMA synchronous system based on the EKF delay estimator. Proc. IEEE Vehicular Technology Conference (VTC), Chicago, IL, USA, 1: 68–71.
148. Buehrer RM (2001) Equal BER performance in linear successive interference cancellation for CDMA systems. IEEE Transactions on Communications 49(7): 1250–1258.
149. Kim JB & Honig ML (1998) Outage probability of multi-code DS-SS with linear interference suppression. Proc. IEEE Military Communications Conference (MILCOM), Boston, MA, USA, 1: 248–252.
150. Nesper O & Ho P (1996) A reference symbol assisted interference cancelling hybrid receiver for an asynchronous DS/SS system. Proc. IEEE International Symposium on Personal, Indoor and Mobile Radio Communications (PIMRC), Taipei, Taiwan, 1: 108–112.
151. Nesper O & Ho P (1996) A pilot symbol assisted interference cancellation scheme for an asynchronous DS/SS system. Proc. IEEE Global Telecommunications Conference (GLOBECOM), London, UK, 3: 1447–1451.
152. Hui ALC & Letaief KB (1998) Successive interference cancellation for multiuser asynchronous DS/SS detectors in multipath fading links. IEEE Transactions on Communications 46(3): 384–391.
153. Hong D-K, You Y-H & Kang C-E (1999) Asymptotic performance limit of a DS/SS rake receiver with a multistage interference cancellation scheme. Proc. IEEE Wireless Communications and Networking Conference (WCNC), New Orleans, LA, USA, 1: 95–98.
154. Yoon YC, Kohno R & Imai H (1993) A spread-spectrum multi-access system with cochannel interference cancellation for multipath fading channels. IEEE Journal on Selected Areas in Communications 11(7): 1067–1075.
155. Jamal K & Dahlman E (1996) Multi-stage serial interference cancellation for DS-SS. Proc. IEEE Vehicular Technology Conference (VTC), Atlanta, GA, USA, 2: 671–675.
156. Soong ACK & Krzymien WA (1996) A novel SS multiuser interference cancellation receiver with reference symbol aided estimation of channel parameters. IEEE Journal on Selected Areas in Communications 14(8): 1536–1547.
157. Patel P & Holtzman J (1994) Analysis of a simple successive interference cancellation scheme in a DS/SS system. IEEE Journal on Selected Areas in Communications 12(5): 796–807.
158. Patel P & Holtzman J (1994) Performance comparison of a DS/SS system using a successive interference cancellation (IC) scheme and a parallel IC scheme under fading. Proc. IEEE International Conference on Communications (ICC), New Orleans, LA, USA, 1: 510–514.
159. Cheng F-C & Holtzman JM (1994) Effect of tracking error on DS/SS successive interference cancellation. Proc. IEEE Global Telecommunications Conference (GLOBECOM), San Francisco, CA, USA, 1: 166–170.
160. Yoshida S & Ushirokawa A (1995) Capacity evaluation of SS-AIC: SS cellular system with adaptive interference cancellation. Proc. IEEE International Conference on Universal Personal Communications (ICUPC), Tokyo, Japan, 148–152.
161. Wei L & Jana R (1999) Performance bounds for optimum multiuser DS-SS systems. IEEE Transactions on Communications 47(2): 185–190.
162. Cruickshank DGM (1996) Suppression of multiple access interference in a DS-SS system using Wiener filtering and parallel cancellation. IEE Proceedings Communications 143(4): 226–230.

163. Buehrer RM, Kaul A, Striglis S & Woerner BD (1996) Analysis of DS-CDMA parallel interference cancellation with phase and timing errors. *IEEE Journal on Selected Areas in Communications* 14(8): 1522–1535.
164. Guo Y & Aazhang B (1999) Capacity of multi-class traffic CDMA system with multiuser receiver. *Proc. IEEE Wireless Communications and Networking Conference (WCNC)*, New Orleans, LA, USA, 1: 500–504.
165. Toskala A, Holma H & Hämäläinen S (1998) Link and system level performance of multiuser detection CDMA uplink. *Wireless Personal Communications* 8(3): 301–320.
166. Hämäläinen S, Holma H & Toskala A (1996) Capacity evaluation of a cellular CDMA uplink with multiuser detection. *Proc. IEEE International Symposium on Spread Spectrum Techniques and Applications (ISSSTA)*, Mainz, Germany, 1: 339–343.
167. Holma H, Toskala A & Ojanperä T (1997) Cellular coverage analysis of wideband MUD-CDMA system. *Proc. IEEE International Symposium on Personal, Indoor and Mobile Radio Communications (PIMRC)*, Helsinki, Finland, 2: 549–553.
168. Hämäläinen S, Holma H, Toskala A & Laukkanen M (1997) Analysis of CDMA downlink capacity enhancements. *Proc. IEEE International Symposium on Personal, Indoor and Mobile Radio Communications (PIMRC)*, Helsinki, Finland, 1: 241–245.
169. Hassell Sweatman CZW, Mulgrew B, Thompson JS & Grant PM (2000) Multiuser detection for CDMA antenna array receivers using spatial equivalence classes. *IEE Proceedings Communications* 147(2): 105–113.
170. Mohamed NA & Dunham JG (2002) A combined antenna array and multi-user detection DS-CDMA receiver in single-path and multi-path fading channels. *Wireless Personal Communications* 20(3): 251–265.
171. Juntti MJ (2000) Performance analysis of linear multisensor multiuser receivers for CDMA in fading channels. *IEEE Journal on Selected Areas in Communications* 18(7): 1221–1229.
172. Papadias CB & Huang H (2001) Linear space-time multiuser detection for multipath CDMA channels. *IEEE Journal on Selected Areas in Communications* 19(2): 254–265.
173. Buehrer RM, Correal-Mendoza NS & Woerner BD (2000) A simulation comparison of multiuser receivers for cellular CDMA. *IEEE Transactions on Vehicular Technology* 49(4): 1065–1085.
174. Ertuğ Ö, Ünal BS & Baykal B (2002) Spectral efficiency and error-exponents of randomly-spread CDMA with linear multiuser receivers over multipath Rayleigh fading channels. *Proc. IEEE International Zurich Seminar on Broadband Communications*, Zurich, Switzerland, 26-1–26-7.
175. Verdú S & Shamai S (1999) Spectral efficiency of CDMA with random spreading. *IEEE Transactions on Information Theory* 45(2): 622–640.
176. Tse DNC & Hanly SV (1999) Linear multiuser receivers: effective interference, effective bandwidth and user capacity. *IEEE Transactions on Information Theory* 45(2): 641–657.
177. Evans J & Tse DNC (2000) Large system performance of linear multiuser receivers in multipath fading channels. *IEEE Transactions on Information Theory* 46(6): 2059–2078.
178. Zheng F-C & Barton SK (1995) On the performance of near-far resistant CDMA detectors in the presence of synchronization errors. *IEEE Transactions on Communications* 43(12): 3037–3045.
179. Moon TK, Xie Z, Rushforth CK & Short RT (1994) Parameter estimation in a multi-user communication system. *IEEE Transactions on Communications* 42(8): 2553–2559.
180. Xie Z, Rushforth CK, Short RT & Moon TK (1993) Joint signal detection and parameter estimation in multiuser communications. *IEEE Transactions on Communications* 41(7): 1208–1216.
181. Lim TJ & Rasmussen LK (1997) Adaptive symbol and parameter estimation in asynchronous multiuser CDMA detectors. *IEEE Transactions on Communications* 45(2): 213–220.

182. Gray SD, Kocic M & Brady D (1995) Multiuser detection in mismatched multiple-access channels. *IEEE Transactions on Communications* 43(12): 3080–3089.
183. Parkvall S, Ottersten B & Ström EG (1995) Sensitivity analysis of linear DS-CDMA detectors to propagation delay estimation errors. *Proc. IEEE Global Telecommunications Conference (GLOBECOM)*, Singapore, 3: 1872–1876.
184. Parkvall S, Ström E & Ottersten B (1996) The impact of timing errors on the performance of linear DS-CDMA receivers. *IEEE Journal on Selected Areas in Communications* 14(8): 1660–1668.
185. Ström EG, Parkvall S, Miller SL & Ottersten BE (1996) Propagation delay estimation in asynchronous direct-sequence code-division multiple access systems. *IEEE Transactions on Communications* 44(1): 84–93.
186. Ström EG, Parkvall S, Miller SL & Ottersten BE (1994) Sensitivity analysis of near-far resistant DS-CDMA receivers to propagation delay estimation errors. *Proc. IEEE Vehicular Technology Conference (VTC)*, Stockholm, Sweden, 2: 757–761.
187. Iltis RA & Maillaender L (1994) An adaptive multiuser detector with joint amplitude and delay estimation. *IEEE Journal on Selected Areas in Communications* 12(5): 774–785.
188. Iltis RA & Maillaender L (1996) Multiuser detection of quasisynchronous CDMA signals using linear decorrelators. *IEEE Transactions on Communications* 44(11): 1561–1571.
189. Turin GL (1980) Introduction to spread-spectrum antimultipath techniques and their application to urban digital radio. *Proceedings of the IEEE* 68(3): 328–353.
190. Mämmelä A (1995) Diversity receivers in a fast fading multipath channel. Doctoral Thesis. VTT Publications 253.
191. Proakis JG (1995) *Digital Communications*, 3rd ed. McGraw-Hill, New York.
192. Abu-Dayya AA & Beaulieu NC (1999) Diversity MPSK receivers in cochannel interference. *IEEE Transactions on Vehicular Technology* 48(6): 1959–1965.
193. Annamalai A, Jing S & Tellambura C (2000) Exact analysis of equal-gain diversity systems over fading channels. *Proc. IEEE Vehicular Technology Conference (VTC'00 Spring)*, Tokyo, Japan, 1: 612–616.
194. Kotsopoulos SA & Karagiannidis (2000) Error performance for equal-gain combiners over Rayleigh fading channels. *Electronics Letters* 36(10): 892–894.
195. Zhang QT (1997) Probability of error for equal-gain combiners over Rayleigh channels: some closed-form solutions. *IEEE Transactions on Communications* 45(3): 270–273.
196. Zhang QT (1999) A simple approach to probability of error for equal gain combiners over Rayleigh channels. *IEEE Transactions on Vehicular Technology* 48(4): 1151–1154.
197. Ziemer RE & Welch TB (2000) Equal-gain combining of multichannel DPSK in Doppler-spread Ricean fading. *IEEE Transactions on Vehicular Technology* 49(5): 1846–1855.
198. Sunay MO & McLane PJ (1996) Diversity combining for DS CDMA systems with synchronization errors. *Proc. IEEE International Conference on Communications (ICC)*, Dallas, TX, USA, 1: 83–89.
199. Sunay MO & McLane PJ (1998) Probability of error for diversity combining in DS CDMA systems with synchronization errors. *European Transactions on Telecommunications* 9(5): 449–463.
200. Eng T, Kong N & Milstein LB (1996) Comparison of diversity combining techniques for Rayleigh-fading channels. *IEEE Transactions on Communications* 44(9): 1117–1129.
201. Eng T, Kong N & Milstein LB (1998) Correction to "Comparison of diversity combining techniques for Rayleigh-fading channels". *IEEE Transactions on Communications* 46(9): 1111.

202. Fang L, Bi G & Kot AC (2000) New method of performance analysis for diversity reception with correlated Rayleigh-fading signals. *IEEE Transactions on Vehicular Technology* 49(5): 1807–1812.
203. Ko Y-C, Alouini M-S & Simon MK (2000) Outage probability of diversity systems over generalized fading channels. *IEEE Transactions on Communications* 48(11): 1783–1787.
204. Oh SK (2001) Class of blind maximal ratio combining methods for digital communication systems. *IEE Proceedings Communications* 148(3): 139–143.
205. Win MZ & Winters JH (1999) Analysis of hybrid selection/maximal-ratio combining of diversity branches with unequal SNR in Rayleigh fading. *Proc. IEEE Vehicular Technology Conference (VTC)*, Houston, TX, USA, 1: 215–220.
206. Polydorou P & Ho P (2000) Error performance of MPSK with diversity combining in non-uniform Rayleigh fading and non-ideal channel estimation. *Proc. IEEE Vehicular Technology Conference (VTC'00 Spring)*, Tokyo, Japan, 1: 627–631.
207. Annamalai A & Tellambura C (2002) Analysis of hybrid selection/maximal-ratio diversity combiners with Gaussian errors. *IEEE Transactions on Wireless Communications* 1(3): 498–512.
208. Win MZ, Beaulieu NC, Shepp LA, Logan BF, Jr. & Winters JH (2003) On the SNR penalty with hybrid selection/maximal ratio combining over i.i.d. Rayleigh fading channels. *IEEE Transactions on Communications* 51(6): 1012–1023.
209. Shao JW, Alouini M-S & Goldsmith A (1999) Impact of fading correlation and unequal branch gains on the capacity of diversity systems. *Proc. IEEE Vehicular Technology Conference (VTC)*, Houston, TX, USA, 3: 2159–2163.
210. Varzakas P & Tombras GS (2002) Average channel capacity for rake receivers. *Electronics Letters* 38(10): 475–476.
211. Simon MK & Alouini M-S (1998) A unified approach to the performance analysis of digital communications over generalized fading channels. *Proceedings of the IEEE* 86(9): 1860–1877.
212. Tomiuk BR, Beaulieu NC & Abu-Dayya AA (1995) Maximal ratio combining with channel estimation errors. *Proc. IEEE Pacific Rim Conference on Communications, Computers and Signal Processing*, Victoria, BC, Canada, 1: 363–366.
213. Tomiuk BR, Beaulieu NC & Abu-Dayya AA (1999) General forms for maximal ratio diversity with weighting errors. *IEEE Transactions on Communications* 47(4): 488–492.
214. Tomiuk BR & Beaulieu NC (1999) Canonical error rate analysis for maximal ratio diversity in correlated fading. *Proc. IEEE Wireless Communications and Networking Conference (WCNC)*, New Orleans, LA, USA, 1: 6–9.
215. Annavajjala R & Milstein LB (2003) On the performance of diversity combining schemes on Rayleigh fading channels with noisy channel estimates. *Proc. IEEE Military Communications Conference (MILCOM)*, Boston, MA, USA, 1: 320–325.
216. Wong RSC, Annamalai A & Bhargava VK (1997) Evaluation of predetection diversity techniques for rake receivers. *Proc. IEEE Pacific Rim Conference on Communications, Computers and Signal Processing*, Victoria, BC, Canada, 1: 227–230.
217. Kim KJ, Kwon SY, Hong EK & Whang KC (2000) Effect of tap spacing on the performance of direct-sequence spread-spectrum rake receiver. *IEEE Transactions on Communications* 48(6): 1029–1036.
218. Alouini M-S & Simon MK (2000) An MGF-based performance analysis of generalized selection combining over Rayleigh fading channels. *IEEE Transactions on Communications* 48(3): 401–415.

219. Yang H-C & Alouini M-S (2004) Generalized switch-and-examine combining (GSEC): a low-complexity combining scheme for diversity-rich environments. *IEEE Transactions on Communications* 52(10): 1711–1721.
220. Mehta NB, Kostić ZA & Win MZ (2003) Interaction between fast scheduling diversity and rake receivers. *Proc. IEEE Vehicular Technology Conference (VTC'03 Spring)*, Jeju, Korea, 2: 1464–1468.
221. Paulraj AJ & Papadias CB (1997) Space-time processing for wireless communications. *IEEE Signal Processing Magazine* 14(11): 49–83.
222. Winters JH (1998) Smart antennas for wireless systems. *IEEE Personal Communications Magazine* 5(1): 23–27.
223. Emamian V, Kaveh M & Alouini M-S (2002) Outage probability with transmit and receive diversity in a shadowing environment. *Proc. IEEE Wireless Communications and Networking Conference (WCNC)*, Orlando, FL, USA, 1: 54–57.
224. Choi J (1999) A receiver of simple structure for antenna array CDMA systems. *IEEE Transactions on Vehicular Technology* 48(5): 1332–1340.
225. Jones HM, Saha A & Abhayapala TD (2003) The effect of finite antenna separation on the performance of spatial diversity receivers. *Proc. IEEE International Symposium on Signal Processing and Its Applications (ISSPA)*, Paris, France, 2: 515–518.
226. Salz J & Winters JH (1994) Effect of fading correlation on adaptive arrays in digital mobile radio. *IEEE Transactions on Vehicular Technology* 43(4): 1049–1057.
227. Kang M & Alouini M-S (2003) Hotelling's generalized distribution and performance of 2D-RAKE receivers. *IEEE Transactions on Information Theory* 49(1): 317–323.
228. Lin T-T (2002) Interference-blocking rake receiver for CDMA systems. *Electronics Letters* 38(13): 655–657.
229. Multispectral Solutions, Inc. – History of UWB technology. [online]. 2006 [cited Oct 5, 2006]. Available from: www.multispectral.com/history.html.
230. Aiello GR & Rogerson (2003) Ultra-wideband wireless systems. *IEEE Microwave Magazine* 4(2): 36–47.
231. Win MZ & Scholtz RA (1998) Impulse radio: how it works. *IEEE Communications Letters* 2(2): 36–38.
232. Porcino D & Hirt W (2003) Ultra-wideband radio technology: potential and challenges ahead. *IEEE Communications Magazine* 41(7): 66–74.
233. Di Benedetto M-G & Vojcic BR (2003) Ultra wide band wireless communications: a tutorial. *Journal of Communications and Networks* 5(4): 290–302.
234. De Nardis L & Di Benedetto M-G (2003) Medium access control design for UWB communication systems: review and trends. *Journal of Communications and Networks* 5(4): 386–393.
235. Hämäläinen M (2006) Singleband UWB systems. Analysis and measurements of coexistence with selected existing radio systems. Doctoral Thesis. *Acta Universitatis Ouluensis C* 240.
236. Zhang J, Kennedy RA & Abhayapala TD (2003) New results on the capacity of M-ary PPM ultra-wideband systems. *Proc. IEEE International Conference on Communications (ICC)*, Anchorage, Alaska, USA, 4: 2867–2871.
237. Cassioli D, Win MZ & Molisch AF (2002) The ultra-wideband indoor channel: from statistical model to simulations. *IEEE Journal on Selected Areas in Communications* 20(6): 1247–1257.
238. Cramer RJ-M, Scholtz RA & Win MZ (2002) Evaluation of an ultra-wide-band propagation channel. *IEEE Transactions on Antennas and Propagation* 50(5): 561–570.
239. Saleh AAM & Valenzuela RA (1987) A statistical model for indoor multipath propagation. *IEEE Journal on Selected Areas in Communications* 5(2): 128–137.

240. Foerster J (Ed.) (2003) Channel modeling sub-committee report final. IEEE P802.15-02/490r1-SG3a, 52 p.
241. Win MZ & Scholtz RA (2002) Characterization of ultra-wide bandwidth wireless indoor channels: a communication-theoretic view. *IEEE Journal on Selected Areas in Communications* 20(9): 1613–1627.
242. Choi JD & Stark WE (2002) Performance of ultra-wideband communications with suboptimal receivers in multipath channels. *IEEE Journal on Selected Areas in Communications* 20(9): 1754–1766.
243. Rajeswaran A, Somayazulu VS & Foerster JR (2003) Rake performance for a pulse based UWB system in a realistic UWB indoor channel. *Proc. IEEE International Conference on Communications (ICC), Anchorage, Alaska, USA, 4: 2879–2883.*
244. Win MZ & Scholtz RA (1998) On the energy capture of ultrawide bandwidth signals in dense multipath environments. *IEEE Communications Letters* 2(9): 245–247.
245. Tesi R, Hämäläinen M & Iinatti J (2003) Impact of the number of fingers of a selective rake receiver for UWB systems in modified Saleh-Valenzuela channel. *Proc. the fourth Finnish Wireless Communications Workshop (FWCW), Oulu, Finland, 140–143.*
246. Rahman MA, Sasaki S, Zhou J, Muramatsu S & Kikuchi H (2004) Evaluation of selective rake receiver in direct sequence ultra wideband communications in the presence of interference. *Proc. IEEE Joint Conference on Ultra Wideband Systems and Technologies and International Workshop on Ultra Wideband Systems (UWBST & IWUWBS), Kyoto, Japan, 221–225.*
247. Durisi G & Benedetto S (2003) Performance evaluation of TH-PPM UWB systems in the presence of multiuser interference. *IEEE Communications Letters* 7(5): 224–226.
248. Ramírez-Mireles F (2002) Signal design for ultra-wide-band communications in dense multipath. *IEEE Transactions on Vehicular Technology* 51(6): 1517–1521.
249. Zhang J, Abhayapala TD & Kennedy RA (2003) Performance of ultra-wideband correlator receiver using Gaussian monocycles. *Proc. IEEE International Conference on Communications (ICC), Anchorage, Alaska, USA, 3: 2192–2196.*
250. Hu B & Beaulieu NC (2003) Exact bit error rate analysis of TH-PPM UWB systems in the presence of multiple-access interference. *IEEE Communications Letters* 7(12): 572–574.
251. Hélot F, Ghavami M & Nakhai MR (2006) Design and performance analysis of a space-time block coding scheme for single band UWB. *IEE Proceedings Communications* 153(1): 127–135.
252. Wilson RD & Scholtz RA (2003) Comparison of CDMA and modulation schemes for UWB radio in a multipath environment. *Proc. IEEE Global Telecommunications Conference (GLOBECOM), San Francisco, CA, USA, 2: 754–758.*
253. Cuomo F, Martello C, Baiocchi A & Capriotti F (2002) Radio resource sharing for ad hoc networking with UWB. *IEEE Journal on Selected Areas in Communications* 20(9): 1722–1732.
254. Forouzan AR & Nasiri-Kenari M & Salehi JA (2002) Performance analysis of time-hopping spread-spectrum multiple-access systems: uncoded and coded schemes. *IEEE Transactions on Wireless Communications* 1: 671–681.
255. Pasand R, Khaleshosseini S, Nielsen J & Sesay A (2006) Exact evaluation of M-ary TH-PPM UWB systems on AWGN channels for indoor multiple-access communications. *IEE Proceedings Communications* 153(1): 83–92.
256. Ramírez-Mireles F (2001) Performance of ultrawideband SSMA using time hopping and M-ary PPM. *IEEE Journal on Selected Areas in Communications* 19(6): 1186–1196.
257. Scholtz RA (1993) Multiple access with time-hopping impulse modulation. *Proc. IEEE Military Communications Conference (MILCOM), Boston, MA, USA, 2: 447–450.*
258. Win MZ & Scholtz RA (2000) Ultra-wide bandwidth time-hopping spread-spectrum impulse radio for wireless multiple-access communications. *IEEE Transactions on Communications* 48(4): 679–691.
259. Di Renzo M, Graziosi F & Santucci F (2005) A framework for performance analysis of TH-UWB communications. *Proc. IEEE International Conference on Ultra-Wideband (ICU), Zurich, Switzerland, 559–564.*

260. Giuliano R & Mazzenga F (2004) Semi analytic calculation of ultra wide band system outage probability. Proc. IEEE Vehicular Technology Conference (VTC-Spring), Milan, Italy, 4: 2215–2218.
261. Giuliano R & Mazzenga F (2004) Capacity analysis for a power controlled UWB indoor system. Proc. IEEE International Symposium on Personal, Indoor and Mobile Radio Communications (PIMRC), Barcelona, Spain, 1: 724–728.
262. Giuliano R & Mazzenga F (2005) Capacity analysis of UWB systems with transmitter power constraints. Proc. IEEE Vehicular Technology Conference (VTC-Spring), Stockholm, Sweden, 5: 3009–3013.
263. Cassioli D, Giuliano R & Mazzenga F (2005) Performance evaluation of high data rate UWB systems based on IEEE 802.15.3. Proc. IEEE International Conference on Ultra-Wideband (ICU), Zurich, Switzerland, 678–683.
264. Sadler BM & Swami A (2004) On the performance of episodic UWB and direct-sequence communication systems. IEEE Transactions on Wireless Communications 3(6): 2246–2255.
265. Boubaker N & Letaief KB (2004) Performance analysis of DS-UWB multiple access under imperfect power control. IEEE Transactions on Communications 52(9): 1459–1463.
266. Chang T-H, Chang Y-J, Peng C-H, Lin Y-H & Chi C-Y (2005) Space time MSINR-SRAKE receiver with finger assignment strategies in UWB multipath channels. Proc. IEEE International Conference on Ultra-Wideband (ICU), Zurich, Switzerland, 242–247.
267. Wong TC, Mark JW & Chua KC (2005) Performance analysis of variable bit rate multiclass services in multi-time-hopping pulse position modulation UWB system. Proc. IEEE Wireless Communications and Networking Conference (WCNC), New Orleans, LA, USA, 1: 651–656.
268. Wong TC, Mark JW & Chua KC (2005) Capacity region of a multi-code DS-UWB system supporting variable bit rate multiclass services. Proc. IEEE International Conference on Communications (ICC), Seoul, Korea, 4: 2857–2861.
269. Foerster JR (2002) The performance of a direct-sequence spread ultrawideband system in the presence of multipath, narrowband interference, and multiuser interference. Proc. IEEE Conference on Ultra Wideband Systems and Technologies, Baltimore (UWBST), MD, USA, 87–91.
270. Welborn M, Miller T, Lynch J & McCorkle J (2002) Multi-user perspectives in UWB communications networks. Proc. IEEE Conference on Ultra Wideband Systems and Technologies, Baltimore, MD, USA, 271–275.
271. Clabaugh DJ, Temple MA, Raines RA & Canadeo CM (2003) UWB multiple access performance using time hopped pulse position modulation with biorthogonal signaling. Proc. IEEE Conference on Ultra Wideband Systems and Technologies (UWBST), Reston, VA, USA, 330–333.
272. Canadeo CM, Temple MA, Baldwin RO & Raines RA (2003) Code selection for enhancing UWB communication performance using TH-PPM and DS-BPSK modulations. Proc. IEEE Wireless Communications Networking Conference (WCNC), New Orleans, LA, USA, 1: 678–682.
273. Canadeo CM, Temple MA, Baldwin RO & Raines RA (2003) UWB multiple access performance in synchronous and asynchronous networks. Electronics Letters 39(11): 880–882.
274. Iacobucci MS & Di Benedetto M-G (2002) Multiple access design for impulse radio communication systems. Proc. IEEE International Conference on Communications (ICC), New York, NY, USA, 2: 817–820.
275. Hoctor RT (2003) Multiple access capacity in multipath channels of delay-hopped transmitted-reference UWB. Proc. IEEE Conference on Ultra Wideband Systems and Technologies (UWBST), Reston, VA, USA, 315–319.
276. Zhang Z, Zeng F & Ge L (2003) Multiple-access interference in relation to time-hopping correlation properties in multiple-access UWB system. Proc. IEEE Conference on Ultra Wideband Systems and Technologies (UWBST), Reston, VA, USA, 453–457.
277. Ziemer R, Wickert M & Williams T (2003) A comparison between UWB and DSSS for use in a multiple access secure wireless sensor network. Proc. IEEE Conference on Ultra Wideband Systems and Technologies (UWBST), Reston, VA, USA, 428–432.

278. Gezici S, Tian Z, Giannakis GB, Kobayashi H, Molisch AF, Poor HV & Sahinoglu Z (2005) Localization via ultra-wideband radios. *IEEE Signal Processing Magazine* 22(4): 70–84.
279. Li Q & Rusch LA (2002) Multiuser detection for DS-CDMA UWB in the home environment. *IEEE Journal on Selected Areas in Communications* 20(9): 1701–1711.
280. Trichard LGF & Kohno R (2003) Iterative multiuser partial parallel interference cancellation for UWB-MA systems. *Proc. 2003 International Workshop on Ultra Wideband Systems (IWUWBS)*, Oulu, Finland, 5 p [CD-ROM].
281. Yoon YC & Kohno R (2002) Optimum multi-user detection in ultra-wideband (UWB) multiple-access communication systems. *Proc. IEEE International Conference on Communications (ICC)*, New York, NY, USA, 2: 812–816.
282. Yang L-L & Hanzo L (2002) Residue number system assisted fast frequency-hopped synchronous ultra-wideband spread-spectrum multiple-access: a design alternative to impulse radio. *IEEE Journal on Selected Areas in Communications* 20(9): 1652–1663.
283. Tonello AM & Rinaldo R (2005) A time-frequency domain approach to synchronization, channel estimation, and detection for DS-CDMA impulse-radio systems. *IEEE Transactions on Wireless Communications* 4(6): 3005–3017.
284. Liu P, Xu Z & Tang J (2003) Minimum variance multiuser detection for impulse radio UWB systems. *Proc. IEEE Conference on Ultra Wideband Systems and Technologies (UWBST)*, Reston, VA, USA, 111–115.
285. Liu P, Xu Z & Tang J (2003) Subspace multiuser receivers for UWB communication systems. *Proc. IEEE Conference on Ultra Wideband Systems and Technologies (UWBST)*, Reston, VA, USA, 116–120.
286. Hämäläinen M, Hovinen V, Tesi R, Iinatti JHJ & Latva-aho M (2002) On the UWB system coexistence with GSM900, UMTS/WCDMA, and GPS. *IEEE Journal on Selected Areas in Communications* 20(9): 1712–1721.
287. Lottici V, D’Andrea A & Mengali U (2002) Channel estimation for ultra-wideband communications. *IEEE Journal on Selected Areas in Communications* 20(9): 1638–1645.
288. Lovelace WM & Townsend JK (2002) The effects of timing jitter and tracking on the performance of impulse radio. *IEEE Journal on Selected Areas in Communications* 20(9): 1646–1651.
289. Güvenç İ & Arslan H (2003) Performance evaluation of UWB systems in the presence of timing jitter. *Proc. IEEE Conference on Ultra Wideband Systems and Technologies (UWBST)*, Reston, VA, USA, 136–141.
290. Fenton LF (1960) The sum of log-normal probability distributions in scatter transmission systems. *IRE Transactions on Communications Systems* 8(1): 57–67.
291. Schwartz S & Yeh YS (1982) On the distribution function and moments of power sums with log-normal components. *Bell System Technical Journal* 61(7): 1441–1462.
292. Prasad R & Kegel A (1991) Improved assessment of interference limits in cellular radio performance. *IEEE Transactions on Vehicular Technology* 40(2): 412–419.
293. Ho C-L (1995) Calculating the mean and variance of power sums with two log-normal components. *IEEE Transactions on Vehicular Technology* 44(4): 756–762.
294. Abu-Dayya AA & Beaulieu NC (1994) Outage probabilities in the presence of correlated lognormal interferers. *IEEE Transactions on Vehicular Technology* 43(1): 164–173.
295. Safak A (1993) Statistical analysis of the power sum of multiple correlated log-normal components. *IEEE Transactions on Vehicular Technology* 42(1): 58–61.
296. Cardieri P & Rappaport TS (2000) Statistics of the sum of lognormal variables in wireless communications. *Proc. IEEE Vehicular Technology Conference (VTC-Spring)*, Tokyo, Japan, 3: 1823–1827.
297. Cardieri P & Rappaport TS (2001) Statistical analysis of co-channel interference in wireless communications systems. *Wireless Communications and Mobile Computing* 1(1): 111–121.

298. Pirinen P (2003) Statistical power sum analysis for nonidentically distributed correlated lognormal signals. Proc. The 2003 Finnish Signal Processing Symposium (FINSIG), Tampere, Finland, 254–258.
299. Santucci F, Pratesi M, Ruggieri M & Graziosi F (2000) A general analysis of signal strength handover algorithms with cochannel interference. IEEE Transactions on Communications 48(2): 231–241.
300. Pratesi M, Santucci F, Graziosi F & Ruggieri M (2000) Outage analysis in mobile radio systems with generically correlated log-normal interferers. IEEE Transactions on Communications 48(3): 381–385.
301. Beaulieu NC, Abu-Dayya AA & McLane PJ (1994) Comparison of methods of computing lognormal sum distributions and outages for digital wireless applications. Proc. IEEE International Conference on Communications (ICC), New Orleans, LA, USA, 3: 1270–1275.
302. Beaulieu NC, Abu-Dayya AA & McLane PJ (1995) Estimating the distribution of a sum of independent lognormal random variables. IEEE Transactions on Communications 43(12): 2869–2873.
303. Stüber GL (1996) Principles of Mobile Communication. Kluwer, Norwell, MA.
304. Schleher DC (1977) Generalized Gram-Charlier series with application to the sum of log-normal variates. IEEE Transactions on Information Technology 23(2): 275–280.
305. Punt JB & Sparreboom (1996) Summing received signal powers with arbitrary probability density functions on a logarithmic scale. Wireless Personal Communications 3(3): 215–224.
306. Caini C, Immovilli G & Merani ML (1992) Outage probability for cellular mobile radio systems: simplified analytical evaluation and simulation results. Electronics Letters 28(7): 669–671.
307. Caini C, Immovilli G & Merani ML (1994) Outage probability in FDMA/TDMA mobile communication networks. European Transactions on Telecommunications 5(1): 59–68.
308. Beaulieu NC & Rajwani F (2004) Highly accurate simple closed-form approximations to lognormal sum distributions and densities. IEEE Communications Letters 8(12): 709–711.
309. Beaulieu NC & Xie Q (2004) An optimal lognormal approximation to lognormal sum distributions. IEEE Transactions on Vehicular Technology 53(2): 479–489.
310. Beaulieu NC & Xie Q (2003) Minimax approximation to lognormal sum distributions. Proc. IEEE Vehicular Technology Conference (VTC-Spring), Jeju, Korea, 2: 1061–1065.
311. Santos Filho JCS, Cardieri P & Yacoub MD (2005) Simple accurate lognormal approximation to lognormal sums. Electronics Letters 41(18): 1016–1017.
312. Ligeti A (2000) Outage probability in the presence of correlated lognormal useful and interfering components. IEEE Communications Letters 4(1): 15–17.
313. Wu J, Mehta NB & Zhang J (2005) A flexible lognormal sum approximation method. Proc. IEEE Global Telecommunications Conference (GLOBECOM), St. Louis, MO, USA, 6: 3413–3417.
314. Lam CLJ & Le-Ngoc T (2005) Log shifted Gamma approximation to lognormal sum distributions. Proc. IEEE International Conference on Communications (ICC), Seoul, Korea, 1: 495–499.
315. Ben Slimane B (2001) Bounds on the distribution of a sum of independent lognormal random variables. IEEE Transactions on Communications 49(6): 975–978.
316. Coulson AJ, Williamson AG & Vaughan RG (1998) A statistical basis for lognormal shadowing effects in multipath fading channels. IEEE Transactions on Communications 46(4): 494–502.
317. Janos WA (1970) Tail of the distribution of sums of log-normal variates. IEEE Transactions on Information Theory IT-16(3): 299–302.
318. Romeo M, Da Costa V & Bardou F (2003) Broad distribution effects in sums of lognormal random variables. The European Physical Journal B 32: 513–525.
319. Glisic S and Vucetic B (1997) CDMA for Wireless Communications. Artech House, Boston, MA, USA, p 1–47.
320. Eng T & Milstein LB (1994) Comparison of hybrid FDMA/CDMA systems in frequency selective Rayleigh fading. IEEE Journal on Selected Areas in Communications 12(5): 938–951.

321. Algans A, Pedersen KI & Mogensen PE (2002) Experimental analysis of the joint statistical properties of azimuth spread, delay spread, and shadow fading. *IEEE Journal on Selected Areas in Communications* 20(3): 523–531.
322. Ziemer RE & Tranter WH (1995) *Principles of Communications, Systems, Modulation, and Noise*. Fourth Edition, John Wiley & Sons, Inc., New York, p 406.
323. Kay SM (1993) *Fundamentals of Statistical Signal Processing: Estimation Theory*. Prentice-Hall, Englewood Cliffs, NJ, USA.
324. Gini F, Luise M & Reggiannini R (1998) Cramér-Rao bounds in the parametric estimation of fading radiotransmission channels. *IEEE Transactions on Communications* 46(10): 1390–1398.
325. Steendam H & Moeneclaey M (2001) Low-SNR limit of the Cramer-Rao bound for estimating the carrier phase and frequency of a PAM, PSK, or QAM waveform. *IEEE Communications Letters* 5(5): 218–220.
326. Steendam H & Moeneclaey M (2001) Low-SNR limit of the Cramer-Rao bound for estimating the time delay of a PSK, QAM, or PAM waveform. *IEEE Communications Letters* 5(1): 31–33.
327. Ström EG & Malmsten F (2000) A maximum likelihood approach for estimating DS-CDMA multipath fading channels. *IEEE Journal on Selected Areas in Communications* 18(1): 132–140.
328. Haeb R & Meyr H (1989) A systematic approach to carrier recovery and detection of digitally phase modulated signals on fading channels. *IEEE Transactions on Communications* 37(7): 748–754.
329. Price R & Green PE Jr. (1958) A communication technique for multipath channels. *Proceedings of the IRE* 46: 555–570.
330. Fukasawa A, Sato T, Takizawa Y, Kato T, Kawabe N & Fisher RE (1996) Wideband CDMA system for personal radio communications. *IEEE Communications Magazine* 34(10): 116–123.
331. Adachi F & Sawahashi M (1998) Wideband wireless access based on DS-CDMA. *IEICE Transactions on Communications* E81-B(7): 1305–1316.
332. Meyr H & Ascheid G (1990) *Synchronization in Digital Communications-Vol. 1, Phase-, Frequency-Locked Loops, and Amplitude Control*. Wiley, New York, p 278.
333. Roy S, Foerster JR, Somayazulu VS & Leeper DG (2004) Ultrawideband radio design: the promise of high-speed, short-range wireless connectivity. *Proceedings of the IEEE*, 92(2): 295–311.
334. Integrated Project PULSERS (IST 506897). [online]. 2006 [cited Oct 5, 2006]. Available from: <http://www.pulsers.info>.
335. Molisch AF, Foerster JR & Pendergrass M (2003) Channel models for ultrawideband personal area networks. *IEEE Wireless Communications* 10(6): 14–21.
336. Zhang J, Kennedy RA & Abhayapala TD (2003) Performance of rake reception for ultra wideband signals in a lognormal-fading channel. *Proc. International Workshop on Ultra Wideband Systems (IWUWBS)*, Oulu, Finland, 5 p [CD-ROM].
337. Cano E & McGrath S (2004) TH-UWB and DS-UWB in lognormal fading channel and 802.11a interference. *Proc. IEEE International Symposium on Personal, Indoor and Mobile Radio Communications (PIMRC)*, Barcelona, Spain, 4: 2978–2982.
338. Giuliano R & Mazzenga F (2005) On the coexistence of power-controlled ultrawide-band systems with UMTS, GPS, DCS1800, and fixed wireless systems. *IEEE Transactions on Vehicular Technology* 54(1): 62–81.
339. Irahauten Z, Nikookar H & Janssen GJM (2004) An overview of ultra wide band indoor channel measurements and modeling. *IEEE Microwave and Wireless Components Letters* 14(8): 386–388.

340. Oh SW & Li KH (1998) Effects of simplified cellular configuration on performance of Rayleigh-faded forward-link CDMA system with power control. *Electronics Letters* 34(23): 2201–2202.
341. Oh SW & Li KH (1999) Effect of circular-cell approximation on the forward-link BER performance of a power-controlled CDMA system. *Proc. IEEE Global Telecommunications Conference (GLOBECOM)*, Rio de Janeiro, Brazil, 5: 2472–2476.
342. Bettstetter C, Hartenstein H & Pérez-Costa X (2004) Stochastic properties of the random waypoint mobility model. *ACM/Kluwer Wireless Networks: Special Issue on Modeling and Analysis of Mobile Networks* 10(5): 555–567.
343. Weisstein EW (2006) Square line picking. From *MathWorld*—A Wolfram Web Resource. [online]. 2006 [cited Oct 5, 2006]. Available from: <http://mathworld.wolfram.com/SquareLinePicking.html>.
344. Weisstein EW (2006) Disk line picking. From *MathWorld*—A Wolfram Web Resource. [online]. 2006 [cited Oct 5, 2006]. Available from: <http://mathworld.wolfram.com/DiskLinePicking.html>.
345. Sheng H, Orlik P, Haimovich AM, Cimini LJ Jr. & Zhang J (2003) On the spectral and power requirements for ultra-wideband transmission. *Proc. IEEE International Conference on Communications (ICC)*, Anchorage, Alaska, USA, 1: 738–742.
346. Ramírez-Mireles F & Scholtz RA (1998) Multiple-access with time hopping and block waveform PPM modulation. *Proc. IEEE International Conference on Communications (ICC)*, Atlanta, GA, USA, 2: 775–779.
347. IEEE 802.15 working group for wireless personal area networks (WPANs) (2006) [online]. 2006 [cited Oct 5, 2006]. Available from: <http://www.ieee802.org/15/>.
348. WILHO home page (2006) [online]. 2006 [cited Oct 5, 2006]. Available from: <http://www.wilho.net>.

Appendix Complex multiuser receiver structure

As a starting point we represent equations (53) and (54) as

$$\mathbf{y}_i = \mathbf{y}_{ii} + \mathbf{y}_{qi} = \mathfrak{R}^{ii} \mathbf{d}_i + \mathfrak{R}^{qi} \mathbf{d}_q + \mathbf{n}_i \quad (155)$$

$$\mathbf{y}_q = \mathbf{y}_{iq} + \mathbf{y}_{qq} = \mathfrak{R}^{iq} \mathbf{d}_i + \mathfrak{R}^{qq} \mathbf{d}_q + \mathbf{n}_q \quad (156)$$

where

$$\mathfrak{R} = \mathbf{RHA} \quad (157)$$

and use an additional step to produce

$$\left(\mathfrak{R}^{ii}\right)^{-1} \mathbf{y}_i = \mathbf{d}_i + \left(\mathfrak{R}^{ii}\right)^{-1} \mathfrak{R}^{qi} \mathbf{d}_q + \left(\mathfrak{R}^{ii}\right)^{-1} \mathbf{n}_i \quad (158)$$

$$\left(\mathfrak{R}^{iq}\right)^{-1} \mathbf{y}_q = \mathbf{d}_i + \left(\mathfrak{R}^{iq}\right)^{-1} \mathfrak{R}^{qq} \mathbf{d}_q + \left(\mathfrak{R}^{iq}\right)^{-1} \mathbf{n}_q \quad (159)$$

$$\left(\mathfrak{R}^{qi}\right)^{-1} \mathbf{y}_i = \left(\mathfrak{R}^{qi}\right)^{-1} \mathfrak{R}^{ii} \mathbf{d}_i + \mathbf{d}_q + \left(\mathfrak{R}^{qi}\right)^{-1} \mathbf{n}_i \quad (160)$$

$$\left(\mathfrak{R}^{qq}\right)^{-1} \mathbf{y}_q = \left(\mathfrak{R}^{qq}\right)^{-1} \mathfrak{R}^{iq} \mathbf{d}_i + \mathbf{d}_q + \left(\mathfrak{R}^{qq}\right)^{-1} \mathbf{n}_q . \quad (161)$$

From (158)–(161) one can show that the data estimates should be obtained as

$$\hat{\mathbf{d}} = \hat{\mathbf{d}}_i + \hat{\mathbf{d}}_q \quad (162)$$

$$\hat{\mathbf{d}}_q = \text{sgn}\left\{\mathbf{D}_{qi} \mathbf{y}_i + \mathbf{D}_{qq} \mathbf{y}_q\right\} \quad (163)$$

$$\mathbf{D}_{qi} = \left\{\left(\mathfrak{R}^{qi}\right)^{-1} \mathfrak{R}^{ii} - \left(\mathfrak{R}^{qq}\right)^{-1} \mathfrak{R}^{iq}\right\}^{-1} \left(\mathfrak{R}^{qi}\right)^{-1} \quad (164)$$

$$\mathbf{D}_{qq} = -\left\{\left(\mathfrak{R}^{qi}\right)^{-1} \mathfrak{R}^{ii} - \left(\mathfrak{R}^{qq}\right)^{-1} \mathfrak{R}^{iq}\right\}^{-1} \left(\mathfrak{R}^{qq}\right)^{-1} \quad (165)$$

and similarly

$$\hat{\mathbf{d}}_i = \text{sgn}\left\{\mathbf{D}_{ii} \mathbf{y}_i + \mathbf{D}_{iq} \mathbf{y}_q\right\} \quad (166)$$

$$\mathbf{D}_{ii} = \left\{ \left(\mathfrak{R}^{ii} \right)^{-1} \mathfrak{R}^{qi} - \left(\mathfrak{R}^{iq} \right)^{-1} \mathfrak{R}^{qq} \right\}^{-1} \left(\mathfrak{R}^{ii} \right)^{-1} \quad (167)$$

$$\mathbf{D}_{iq} = - \left\{ \left(\mathfrak{R}^{ii} \right)^{-1} \mathfrak{R}^{qi} - \left(\mathfrak{R}^{iq} \right)^{-1} \mathfrak{R}^{qq} \right\}^{-1} \left(\mathfrak{R}^{iq} \right)^{-1}. \quad (168)$$

Bearing in mind that all current wideband CDMA standards are based on using complex signal formats future research in the field of multiuser detectors should be focused on the structures defined by (155)–(168).

242. Lumijärvi, Jouko (2006) Optimization of critical flow velocity in cantilevered fluid-conveying pipes, with a subsequent non-linear analysis
243. Stoor, Tuomas (2006) Air in pulp and papermaking processes
244. György, Zsuzsanna (2006) Glycoside production by in vitro *Rhodiola rosea* cultures
245. Özer-Kemppainen, Özlem (2006) Alternative housing environments for the elderly in the information society. The Finnish experience
246. Laurinen, Perttu (2006) A top-down approach for creating and implementing data mining solutions
247. Jortama, Timo (2006) A self-assessment based method for post-completion audits in paper production line investment projects
248. Remes, Janne (2006) The development of laser chemical vapor deposition and focused ion beam methods for prototype integrated circuit modification
249. Kinnunen, Matti (2006) Comparison of optical coherence tomography, the pulsed photoacoustic technique, and the time-of-flight technique in glucose measurements *in vitro*
250. Iskanius, Päivi (2006) An agile supply chain for a project-oriented steel product network
251. Rantanen, Rami (2006) Modelling and control of cooking degree in conventional and modified continuous pulping processes
252. Koskiaho, Jari (2006) Retention performance and hydraulic design of constructed wetlands treating runoff waters from arable land
253. Koskinen, Miika (2006) Automatic assessment of functional suppression of the central nervous system due to propofol anesthetic infusion. From EEG phenomena to a quantitative index
254. Heino, Jyrki (2006) Harjavallan Suurteollisuuspuisto teollisen ekosysteemin esimerkkinä kehitettäessä hiiliteräksen ympäristömyönteisyyttä
255. Gebus, Sébastien (2006) Knowledge-based decision support systems for production optimization and quality improvement in the electronics industry
256. Alarousu, Erkki (2006) Low coherence interferometry and optical coherence tomography in paper measurements
257. Leppäkoski, Kimmo (2006) Utilisation of non-linear modelling methods in flue-gas oxygen-content control

Book orders:
OULU UNIVERSITY PRESS
P.O. Box 8200, FI-90014
University of Oulu, Finland

Distributed by
OULU UNIVERSITY LIBRARY
P.O. Box 7500, FI-90014
University of Oulu, Finland

S E R I E S E D I T O R S

A
SCIENTIAE RERUM NATURALIUM
Professor Mikko Siponen

B
HUMANIORA
Professor Harri Mantila

C
TECHNICA
Professor Juha Kostamovaara

D
MEDICA
Professor Olli Vuolteenaho

E
SCIENTIAE RERUM SOCIALIUM
Senior Assistant Timo Latomaa

E
SCRIPTA ACADEMICA
Communications Officer Elna Stjerna

G
OECONOMICA
Senior Lecturer Seppo Eriksson

EDITOR IN CHIEF
Professor Olli Vuolteenaho

EDITORIAL SECRETARY
Publications Editor Kirsti Nurkkala

ISBN 951-42-8269-8 (Paperback)

ISBN 951-42-8270-1 (PDF)

ISSN 0355-3213 (Print)

ISSN 1796-2226 (Online)

